American Journal of
Electronics & Communication

Contents

Diffraction Tomography Using Born Approximation

S.Banerjee [1]

Indian Institute of Technology, Delhi
Kolkata India
soumyadip.banerjee@gmail.com

Abstract— **This paper mainly describes a new method to solve forward and backward problem related to 2D diffraction tomography. The method is based upon Born approximation which holds for weakly scattering body. A new approach to mapping is presented from real space to K-space. The reconstructed images are obtained for different SNR values and also for different resolution in K space. Also suitable forward and inverse formulas are presented for the following method.**

Index Terms— **Diffraction tomography, K-space, Ewald's circle, Fourier transform, Born approximation**

I. INTRODUCTION

The last two decades has seen an immense growth in the development of new algorithms and techniques in diffraction tomography problems. Though non-diffracting tomography is more popular in medical applications, still when it comes to reconstruction of the shape and the electrical properties (complex refractive index profile) of the body under test, diffraction tomography has an advantage. Early techniques employed Fourier diffraction theorem [6] to obtain data in frequency domain and that data is processed using an inverse algorithm [2] to get back the reconstructed image. Unlike the direct methods which work on far field data, there are methods which work on near field

data and the reconstruction occurs through an iterative process and is based on moment method solution [10].

This paper is organised as follows. First the theoretical background is provided for both 2D diffraction tomography. Under 2D tomography the mathematical foundation for the two new scanning methods are explained and corresponding to the methods the forward and the inverse formulas are provided. A suitable forward and reconstruction formula is also provided. Secondly, there is the Simulation and Result section where the above methods are tested on different test bodies and the reconstructed images are shown for different cases. Finally, conclusion of the work is provided.

II. THEORY

Considering an inhomogeneous medium for which the Helmholtz equation is given by

$$[\nabla^2 + k^2]\mathbf{u}(\mathbf{r}) = 0 \qquad (1)$$

Where, k(r) =k_0n(**r**)
k_0=average wave no. of the medium.
n(**r**) is complex refractive index of the medium given by

$$n(\mathbf{r}) = \sqrt{\frac{\mu(\mathbf{r})\,\varepsilon(\mathbf{r})}{\mu 0 \,\varepsilon 0}}$$

u(**r**)=Complex amplitude of the total field at position given by **r**.

The above equation can be rewritten as

$$[\nabla^2 + k_0{}^2]\, \mathbf{u_s(r)} = -\mathbf{u(r)}F(\mathbf{r}) \qquad (2)$$

Where, F(**r**) = $k_0{}^2$[n^2(**r**)-1]

F(**r**) is the forcing function called the scattering potential and $\mathbf{u_s(r)}$ is the complex amplitude of the scattered field.

The solution to (2) obtained by green's function method is given as

$$\mathbf{u_s(r)} = \int F(\mathbf{r}', \boldsymbol{\omega})\, g\,(\mathbf{r} \mid \mathbf{r'})\, u(\mathbf{r})\; dv \qquad (3)$$

Where, g(r|r') is the green's function used in the solution.

The above solution (3) is a Fredholm equation of second kind. Though there are standard theoretical and numerical methods [5] to solve the equation. But if the test body has weak inhomogeneity then the above equation can be simplified using first order Born approximation [6]. In this approximation the total field in (3) is replaced by the incident field u_0(**r**) and hence the simplified equation is given by

$$\mathbf{u_s(r)} = \int F(\mathbf{r}', \boldsymbol{\omega})\, g\,(\mathbf{r} \mid \mathbf{r'})\, u_0(\mathbf{r})\; dv \qquad (4)$$

where, in 2D case the Green's function is given by

$$g\,(\mathbf{r} \mid \mathbf{r'}) = -\frac{j}{4}\, H_0^2(k_0|\mathbf{r} - \mathbf{r'}|)$$

A. *Forward Problem*

In 2D diffraction tomography the test object or objects are considered to be having refractive index variation along the cross-section and having no or gradual variation with height. Under far field approximation [6] the scattered field at the observation point is given by

$$\mathbf{u_s(r)} = A_0 \sqrt{\frac{2j}{\pi k_0 r}}\, e^{-j k_0 r}\, f(\mathbf{s_0}, \mathbf{s}) \qquad (5)$$

Where, A_0= amplitude of the incident field

$\mathbf{s_0}$=unit vector along the direction of propagation of the incident field.

s = unit vector directed towards the position of the receiver Rx

f($\mathbf{s_0}$, **s**) is called the Scattering amplitude and is given as

$$f(\mathbf{s_0}, \mathbf{s}) = F'[\mathbf{K}] = \iint F(\mathbf{r}', \boldsymbol{\omega})\, e^{-j\mathbf{K}.\mathbf{r'}}\; ds \qquad (6)$$

Here, **K** = k_0(**s**-$\mathbf{s_0}$) is called the spatial frequency vector[6]. The significance of (6) is that the complex amplitude of the scattered field measured in the far field region depends entirely on only one Fourier component of the scattering potential F(**r**) corresponding to a given K vector. The approach in this type of problem is to obtain Fourier component data for all K vectors within the K space. For that the scattered field is to be measured at all possible direction **s** and also for all possible direction of the incident wave $\mathbf{s_0}$. This is best diagrammatically described by Ewald's circle of reflection. For a fixed $\mathbf{k_0}$ and different orientation of **k** the K vector traces out this Ewald's circle of reflection. In 3D case the circle transforms into a sphere. The **K** space is bounded by the outer circle of radius given by K=2k_0
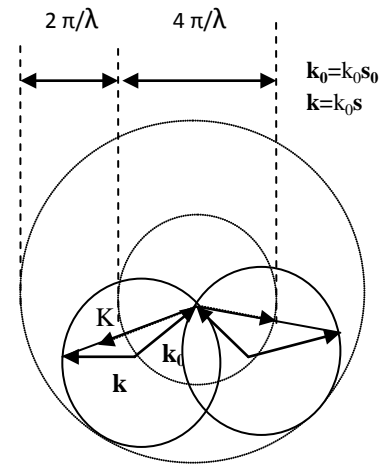
Fig. 1. The figure showing the construction of a **K** vector from **k** and $\mathbf{k_0}$ vector and the Ewald's circle it traces out for two possible orientation of $\mathbf{k_0}$ vector.

Two methods are suggested to solve the forward problem. It is seen from (6) that the 2D Fourier transform value f depends mainly on **K.** Generally, Fourier diffraction theorem is applied to obtain f data for different position of receiver and also for different angle of incidence. But this leads to a non-linear mapping from real space to **K** space. This makes the reconstruction procedure difficult. To circumvent the situation the sampled values of the scattered field is extracted at non-uniform intervals in real space so that the f data are obtained for uniform sampled values of K. This makes the reconstruction problem easier to handle.

In the first method (Method I) the K space is pictured with the help of a Cartesian co-ordinate system, where it is divided into uniform cells of size ΔK as shown in the figure below
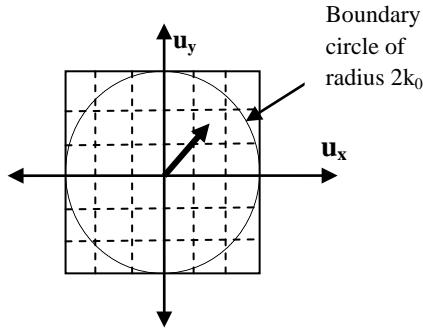
Fig. 2. Representation of K space in Cartesian co-ordinate system. The dark arrow representing to a K vector pointing to one of the cell.

In order to obtain f data corresponding to each cell the transmitting and the receiving antenna should be properly oriented with respect to the test body in the far field region. An effective way of doing this is to make the transmitter fixed and change the angular position of the receiver accompanied by a proper rotation of the body to a particular angle.

Let $\mathbf{K}=K_x\,\mathbf{u_x} + K_y\,\mathbf{u_y} = m\Delta K\,\mathbf{u_x} + n\Delta K\,\mathbf{u_y}$
and $\Delta K = 2k_0/M$,
where m and n are rational no.s and $(2M)^2$ is the total no. of cells the K space is divided into.

The Tx antenna position on a unit radius circle is fixed and is given by
$X_{Tx}= 1$ $\qquad$ $Y_{Tx}= 0$

The Rx antenna position on a unit radius circle is given by
$X_{Rx}= -\cos(\alpha - \alpha_0)$ $\qquad$ $Y_{Rx}= \sin(\alpha - \alpha_0)$

Where, $\alpha_0 = \tan^{-1}\dfrac{n}{m} + \cos^{-1}\dfrac{\sqrt{(m^2+n^2)}}{M}$ $\qquad$ (7)

and, $\alpha=\tan^{-1}[\dfrac{sin\,\alpha 0 - 2\frac{n}{M}}{cos\,\alpha 0 - 2\frac{m}{M}}]$ $\qquad$ (8)

In order to obtain proper incident field direction the test body is rotated by an angle $\pi-\alpha_0$ in anti-clockwise direction.
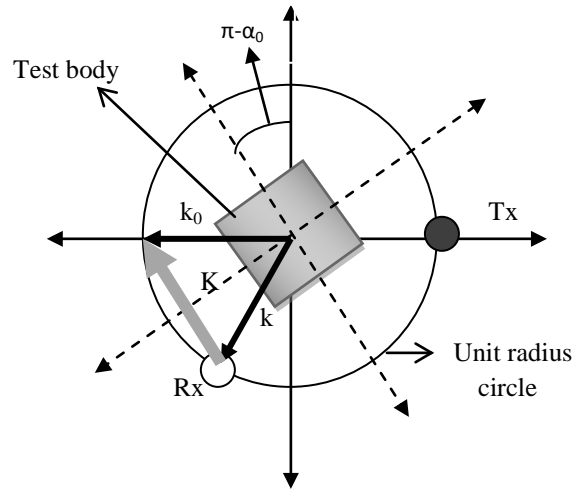
Fig. 3. Diagram showing the arrangement of Tx ,Rx and the body for the Method I type scanning.

The forward formula for obtaining the scattering amplitude value is obtained by dividing the entire body or the scattering region into N no. of square cells of side length h. For a given K vector f is given by

$$f(\mathbf{K})=h^2\,sinc(\frac{K_x h}{2})sinc(\frac{K_y h}{2})\sum_{i=1}^{N} F(r_i^{'})e^{-j\,\mathbf{K}\cdot\mathbf{r_i}'}$$
$\qquad$ (9)

Where, $\mathbf{r_i}'=x_i'\mathbf{u_x} + y_i'\mathbf{u_y}$ is the position vector of the ith cell of the scattering region and h^2 is the cell area.

2.3 Backward Problem

As the K-space is divided into uniform cells, so the low pass filtered approximation of the scattering potential [6] can be written as

$$F_{LP}(\mathbf{r}) =(\frac{\Delta K}{2\pi})^2\,sinc\frac{\Delta K\,x}{2})\,sinc\,(\frac{\Delta K\,y}{2})\sum_{i=1}^{(2M)^2} f(K_i)\,e^{j\,K_i.r}$$
$\qquad$ (10)

ΔK^2 = area of each cell in K-space.

Here, $\mathbf{K}_i$ specifies the position vector of the ith cell in K-space. The above discrete sum is to be evaluated within the boundary circle.

III. Numerical Model

The numerical model of two different test bodies is presented in this section. The first body considered is a 2D body with mainly three types of scatterers placed at different locations and having different refractive index

profile. While the second body considered is a high contrast body compared to the first comprising of bones and muscles. The shape of the bones are approximated to square in nature instead of being irregular. The body image of both the bodies are divided into $2500(50^2)$ cells.

A. Body Model A

4-a

4-b
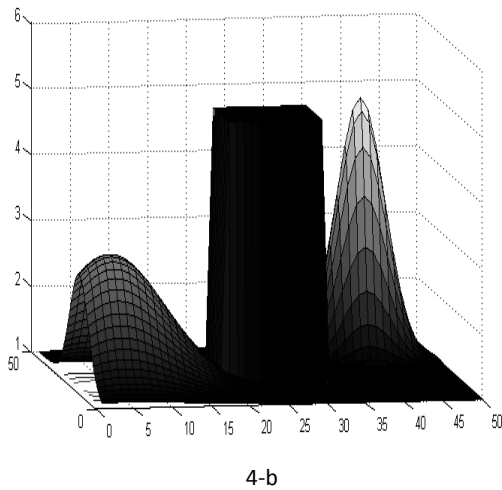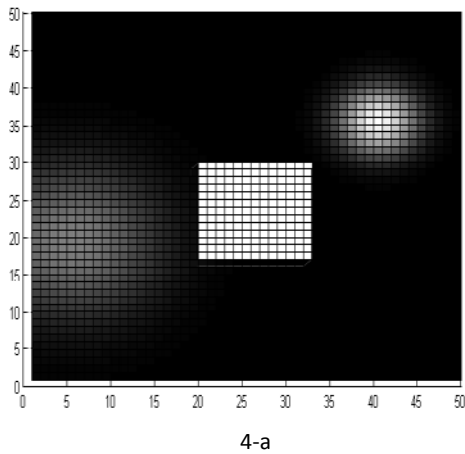
Fig-4(*a*) figure showing the position and the shape of the scatterers in the region R' (extent of R' is 10cmX10cm) of Body A (b) figure depicting the real part of the refractive (n_r) index of the object(at 10GHz)

5-a

5-b
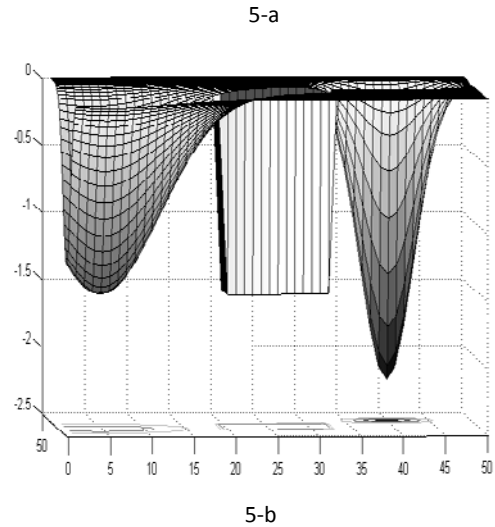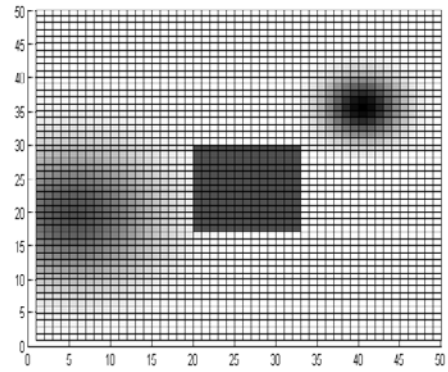
Fig-5(*a*) figure showing the position and the shape of the scatterers in the region R' (extent of R' is 10cmX10cm) (b) figure depicting the imaginary part of the refractive (n_i) index of the object (at 10GHz)

B. Body Model B

6-a
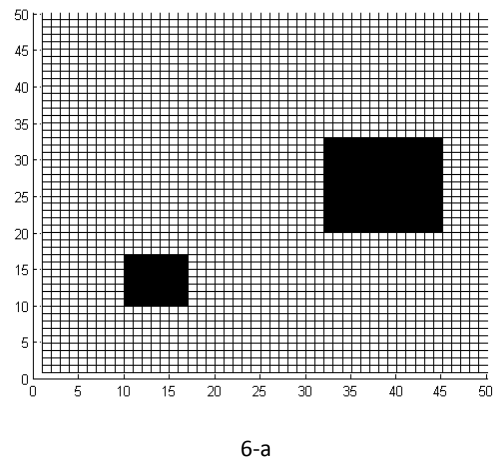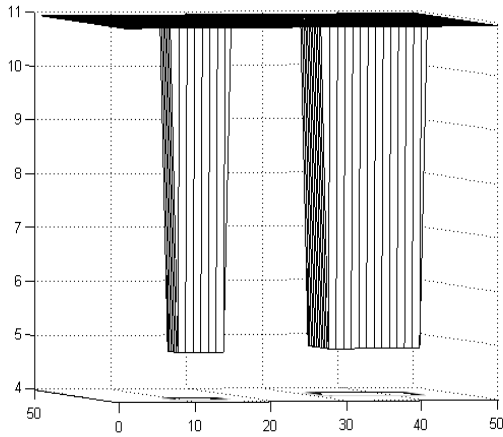
6-b

Fig-6(*a*) figure showing the position and the shape of the scatterers in the region R' (extent of R' is 10cmX10cm) of Body B(b) figure depicting the real part of the refractive (n_r) index of the object(at 10GHz)

IV. Results and Discussion

The reconstructed images of the bodies are presented for two separate cases i.e. for method I and II. For each method the reconstructed images are obtained for high and low resolution in K-space. The inverse methods are tested with signals corrupted with different amount of noise. The type of noise considered over here is an Additive White Gaussian Noise (AWGN). The frequency of operation is 10GHz and the incident field amplitude is 1V/m for each case.

The results of the body model A is shown in fig 8,9 and 10 under different noise condition and considering high resolution in K space.. The no. of cells in K space is considered to be $2500(50)^2$. The no. of cells of the reconstructed image is $400(20^2)$.

7-a

7-b

Fig-7(*a*) figure showing the position and the shape of the scatterers in the region R' (extent of R' is 10cmX10cm) of Body B(b) figure depicting the imaginary part of the refractive (n_i) index of the object(at 10GHz)

8-a

8-b

8-c

8-d
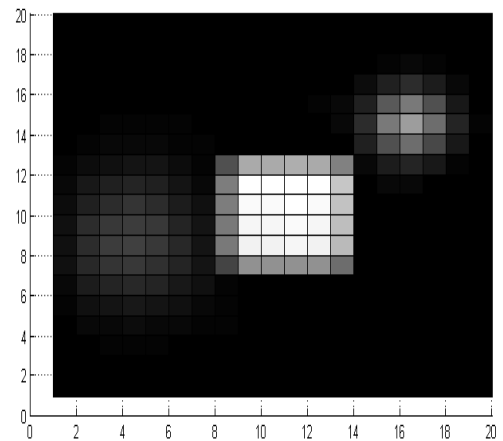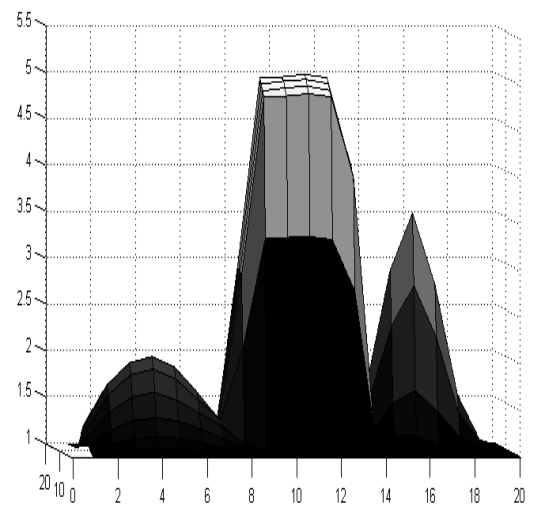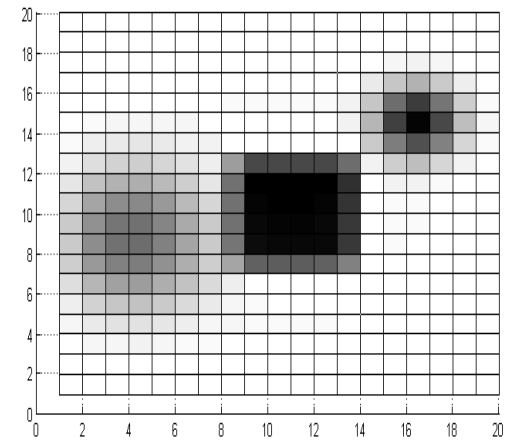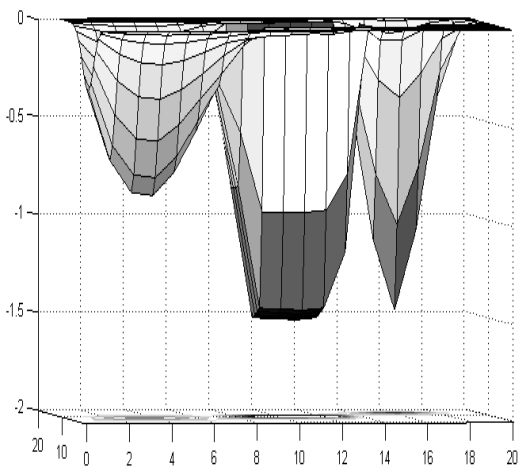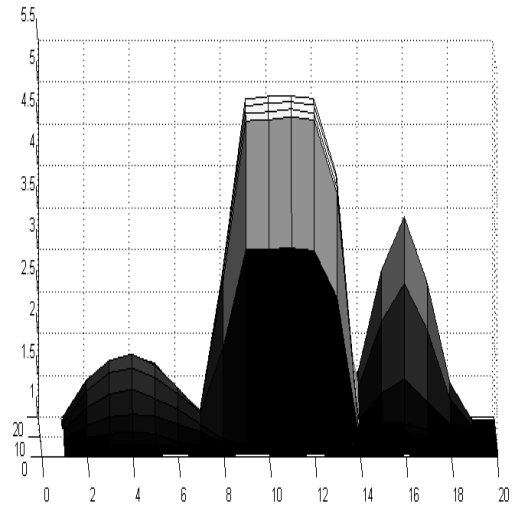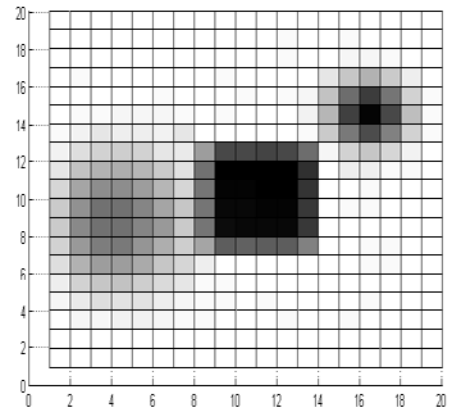
Fig-8 Reconstructed images of body A for high resolution in K-space. The profile of the real part of the refractive index obtained is shown in a and b while the imaginary part shown in c and d. The images are obtained under noise free condition.

9-a

9-b

9-c
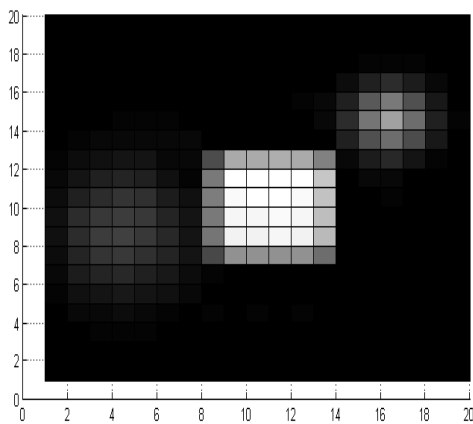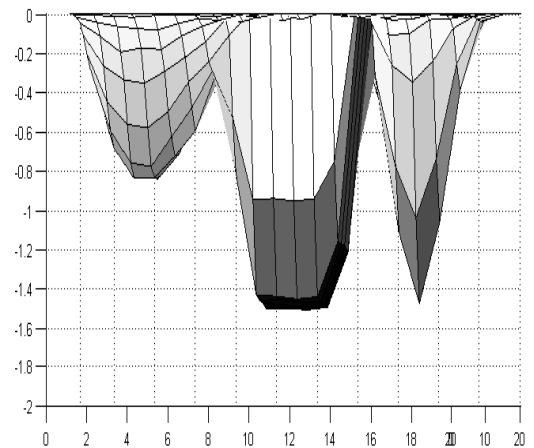
9-d

Fig-9 Reconstructed images of body A for high resolution in K-space. The profile of the real part of the refractive index obtained is shown in a and b while the imaginary part shown in c and d. The images are obtained under SNR=30dB

10-a

10-b

10-c

10-d
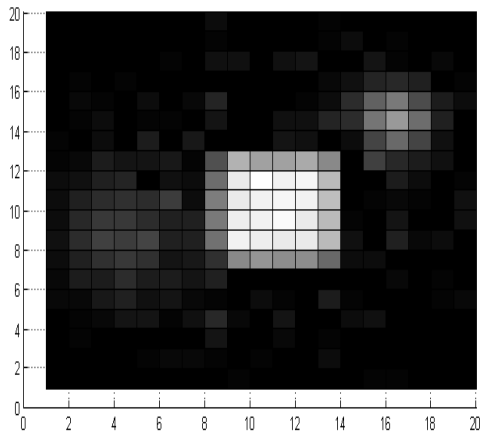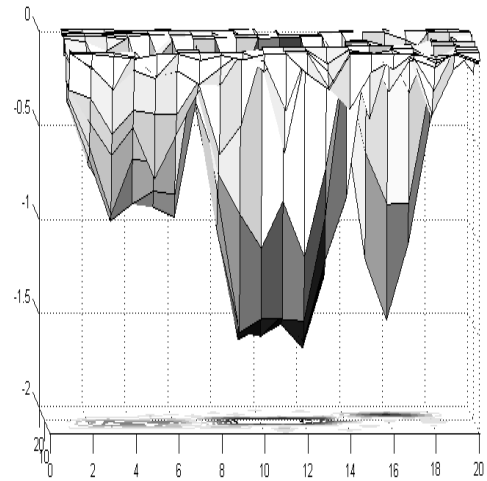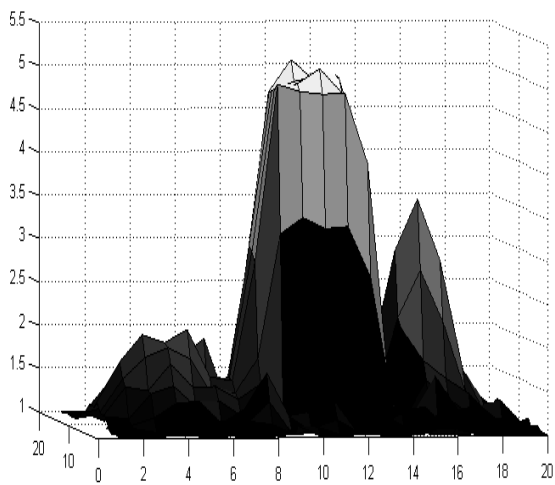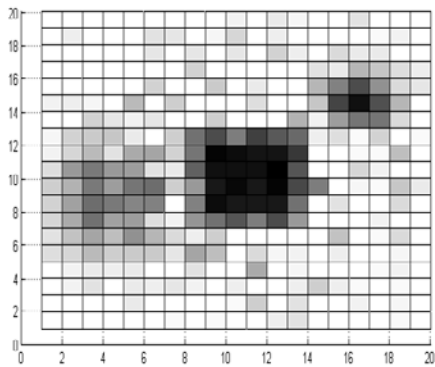
Fig-10 Reconstructed images of body A for high resolution in K-space. The profile of the real part of the refractive index obtained is shown in a and b while the imaginary part shown in c and d. The images are obtained under SNR=10dB

The results of the body model A is shown in fig 11-13 under different noise condition and considering low resolution in K space.. The no. of cells in K space is considered to be $900(30)^2$. The no. of cells of the reconstructed image is $400(20^2)$.

11-a

11-b

12-a

11-c

12-b

11-d
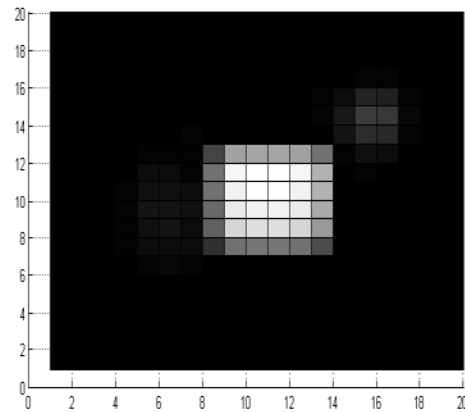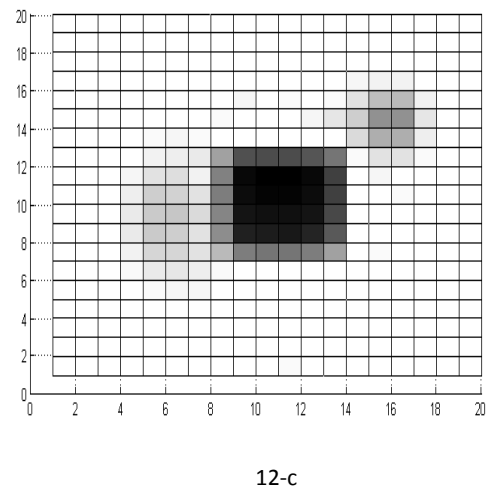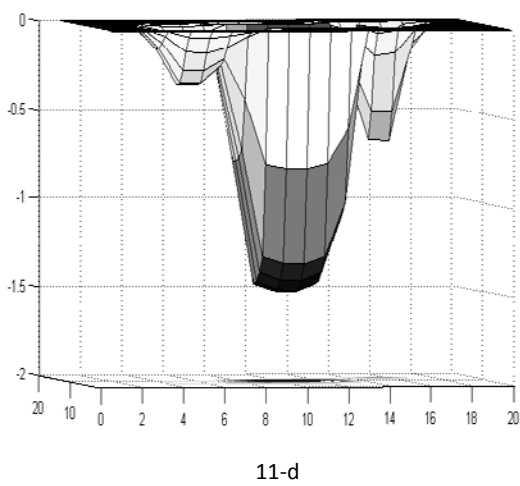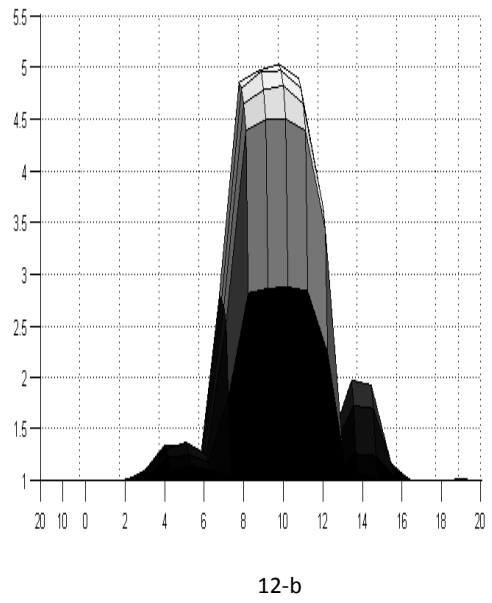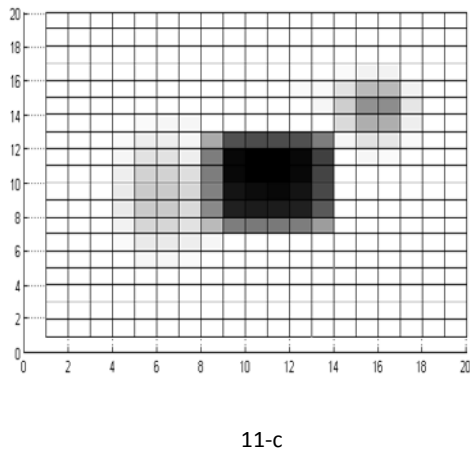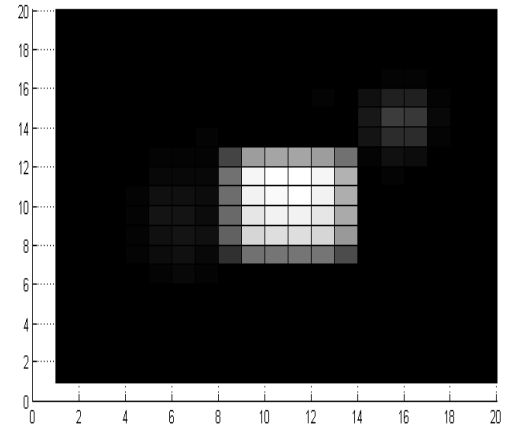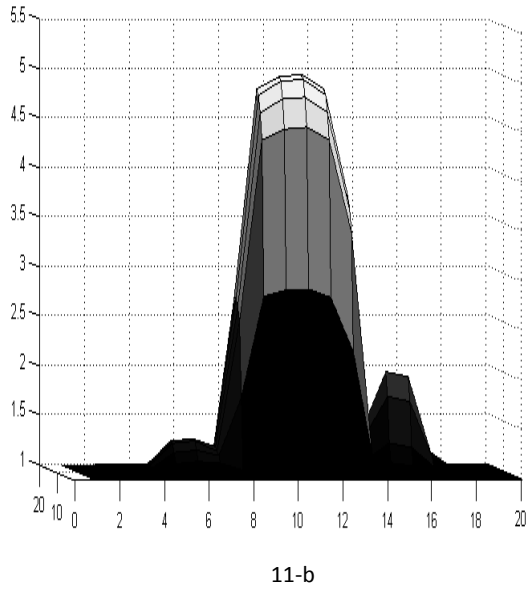
Fig-11 Reconstructed images of body A for low resolution in K-space. The profile of the real part of the refractive index obtained is shown in a and b while the imaginary part shown in c and d. The images are obtained under noise free condition.

12-c

12-d
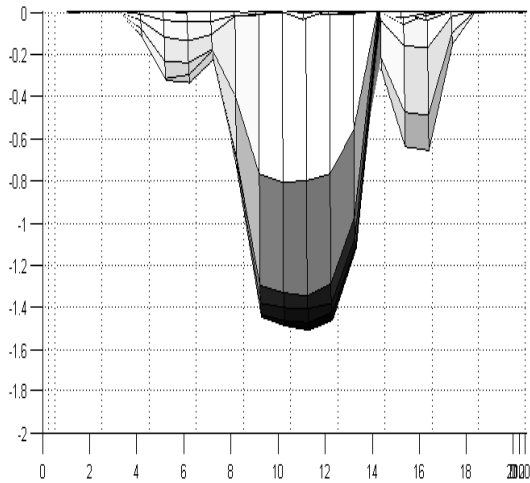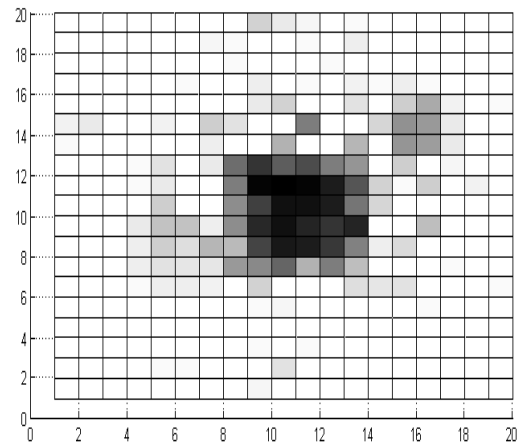
Fig-12 Reconstructed images of body A for low resolution in K-space. The profile of the real part of the refractive index obtained is shown in a and b while the imaginary part shown in c and d. The images are obtained under SNR-30 dB.

13-c
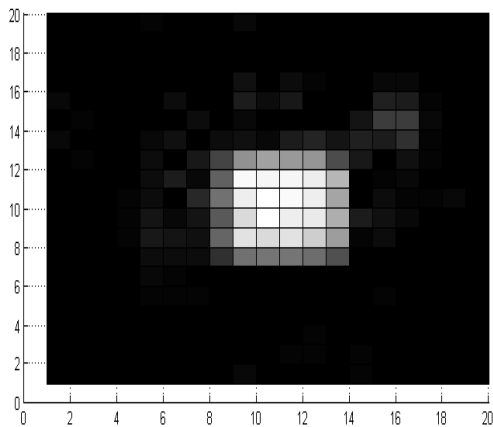
13-a
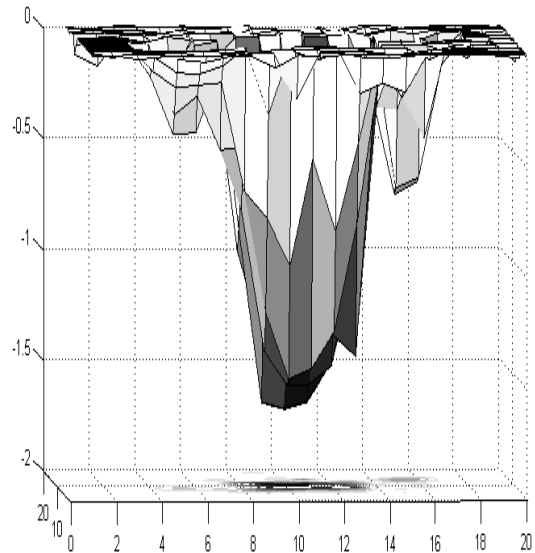
13-d

Fig-13 Reconstructed images of body A for low resolution in K-space. The profile of the real part of the refractive index obtained is shown in a and b while the imaginary part shown in c and d. The images are obtained under SNR-10 dB.
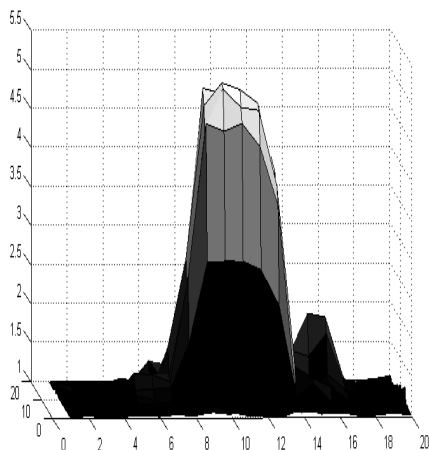
13-b

The results of the body model B is shown in fig 14,15 and 16 under different noise condition and considering high resolution in K space.. The no. of cells in K space is considered to be $2500(50)^2$. The no. of cells of the reconstructed image is $400(20^2)$.
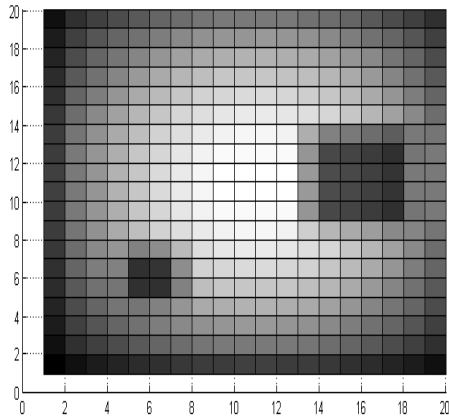
14-a
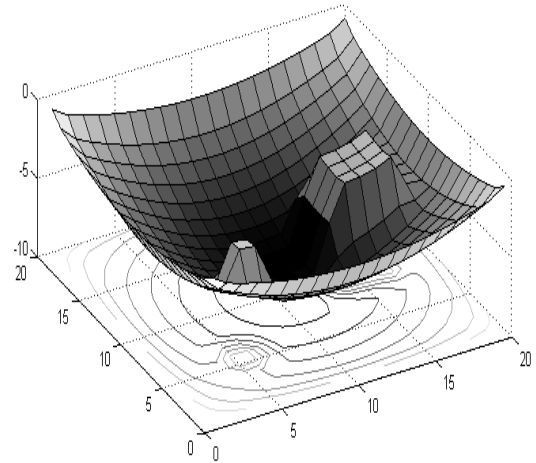
14-d

Fig-14 Reconstructed images of body A for high resolution in K-space. The profile of the real part of the refractive index obtained is shown in a and b while the imaginary part shown in c and d. The images are obtained under noise free condition.
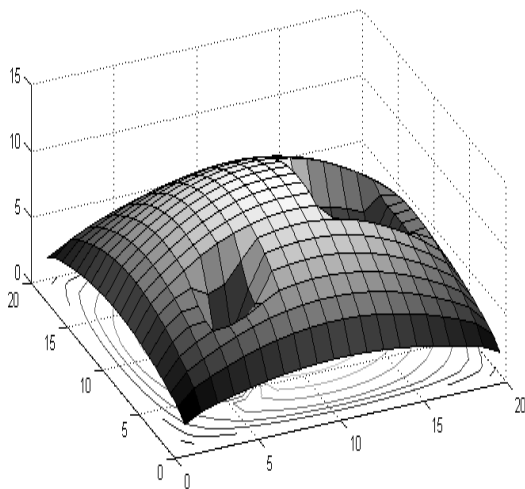
14-b

14-c

15-a

15-b

15-c

16-b

15-d
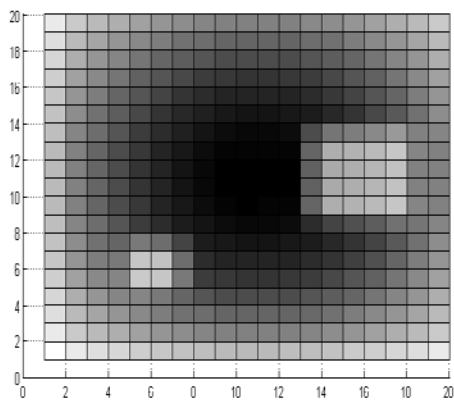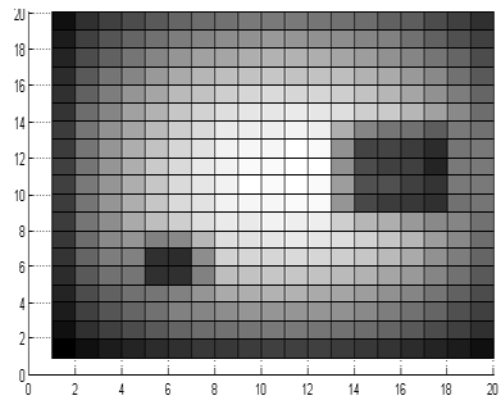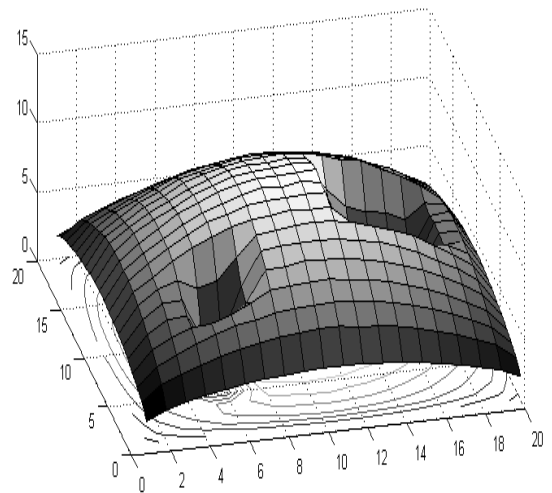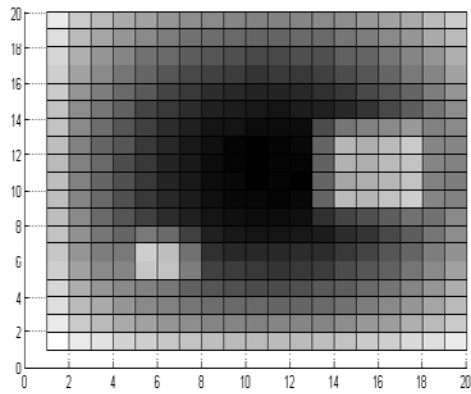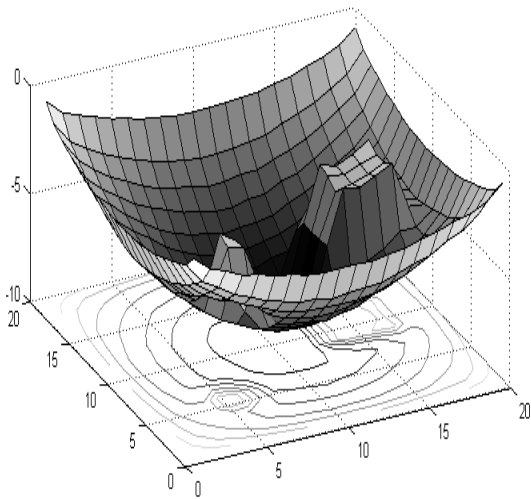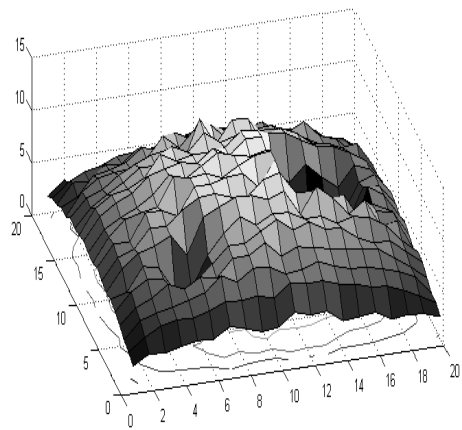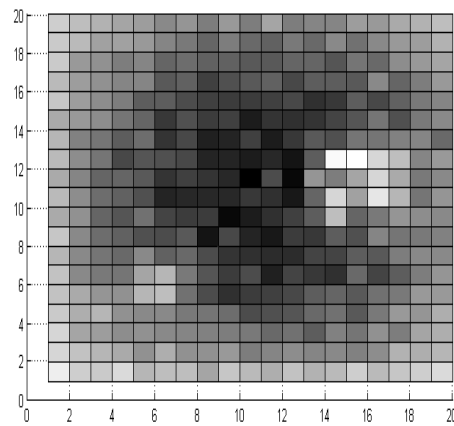
16-c

Fig-15 Reconstructed images of body A for high resolution in K-space. The profile of the real part of the refractive index obtained is shown in a and b while the imaginary part shown in c and d. The images are obtained under SNR-30 dB.
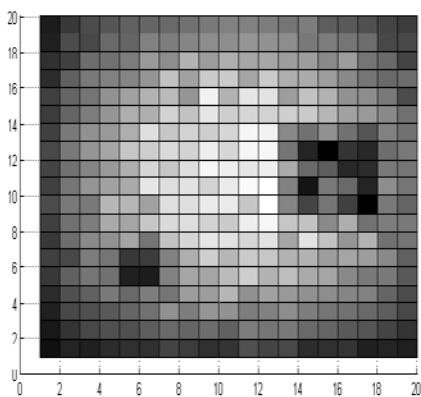
16-a
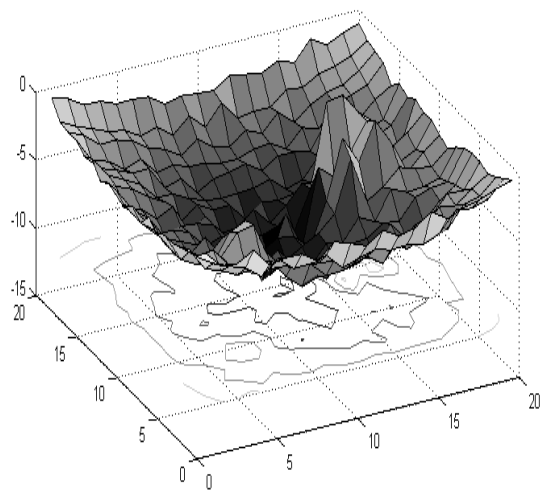
16-d

Fig-16 Reconstructed images of body A for high resolution in K-space. The profile of the real part of the refractive index obtained is shown in a and b while the imaginary part shown in c and d. The images are obtained under SNR-10 dB.

The results of the body model B is shown in fig 17-19 under different noise condition and considering high resolution in K space.. The no. of cells in K space is considered to be $900(30)^2$. The no. of cells of the reconstructed image is $400(20^2)$.

17-c

17-a

17-d
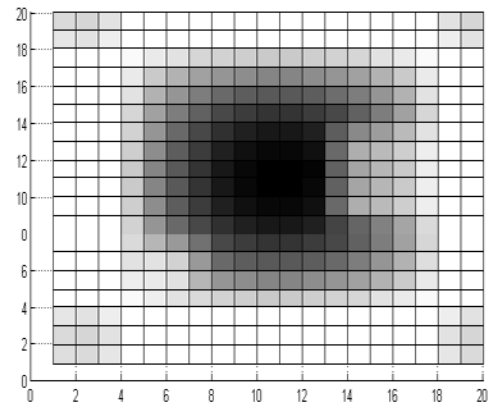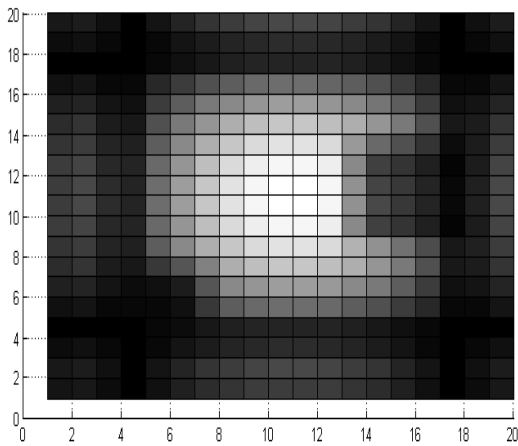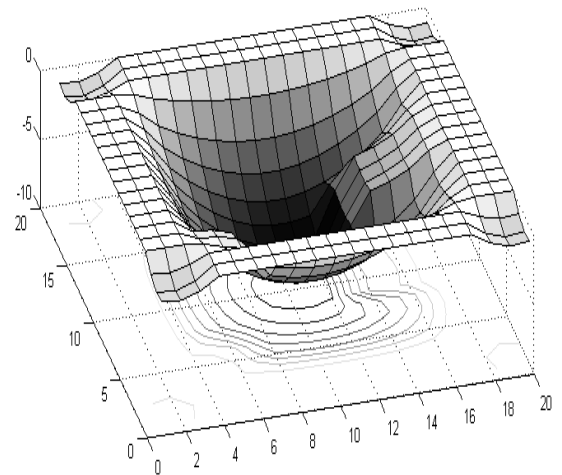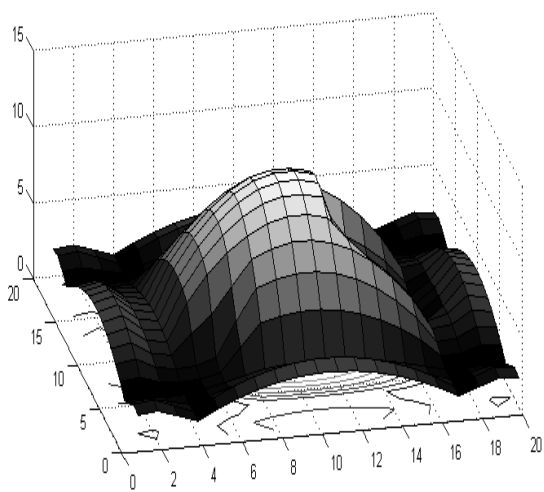
Fig-17 Reconstructed images of body A for low resolution in K-space. The profile of the real part of the refractive index obtained is shown in a and b while the imaginary part shown in c and d. The images are obtained under noise free condition.

17-b
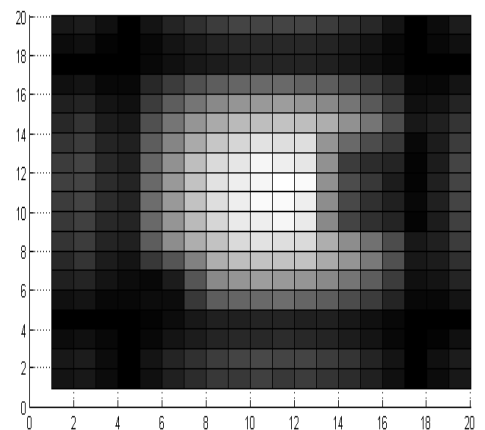
18-a
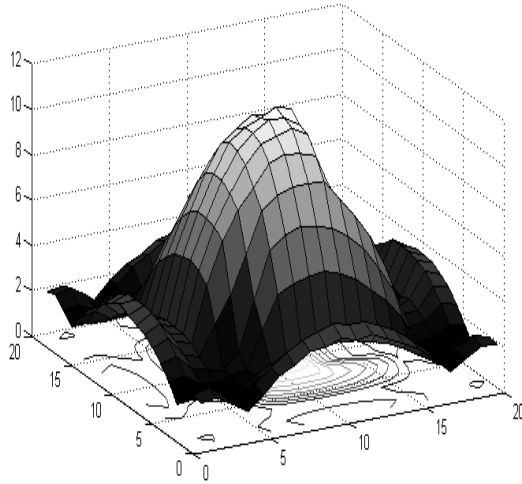
18-b
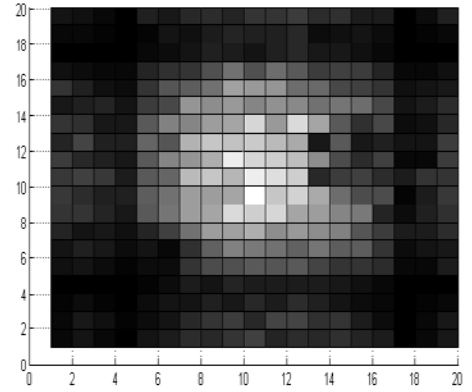
19-a
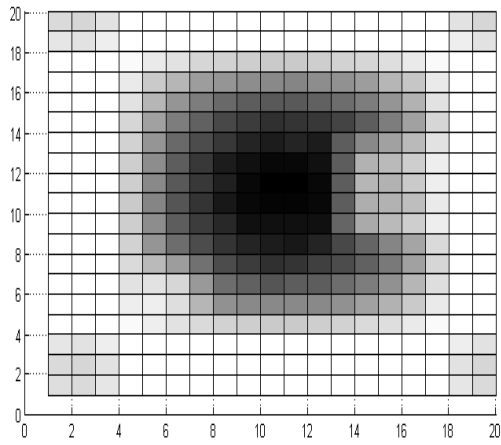
18-c
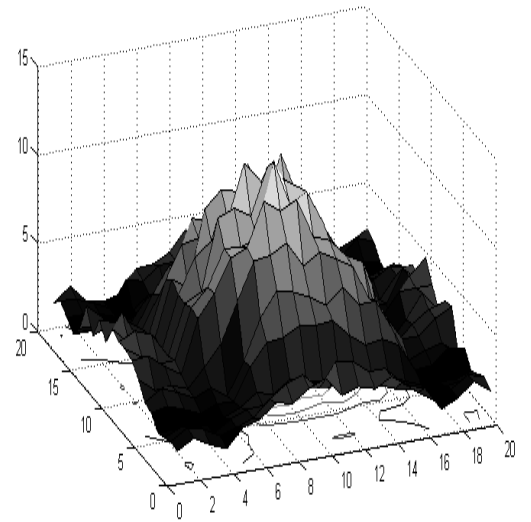
19-b
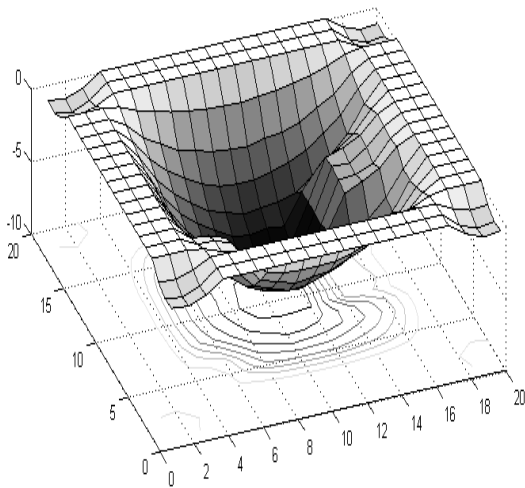
18-d
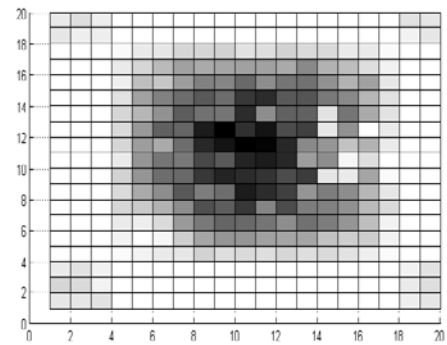
19-c

Fig-18 Reconstructed images of body A for low resolution in K-space. The profile of the real part of the refractive index obtained is shown in a and b while the imaginary part shown in c and d. The images are obtained under SNR-30 dB.
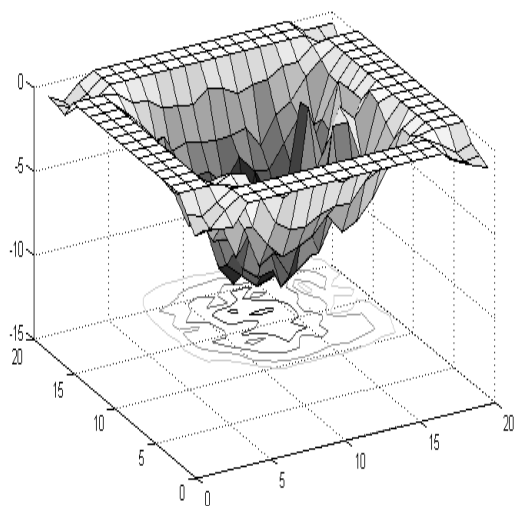
19-d

Fig-19 Reconstructed images of body A for low resolution in K-space. The profile of the real part of the refractive index obtained is shown in a and b while the imaginary part shown in c and d. The images are obtained under SNR-10 dB.

When the reconstructed images are compared under the same noise condition then it is observed that the quality of the image is better when high resolution in K space is considered. This is more visible for images associated with low SNR values where it is hard to recover the profile of the body. The reconstructed images obtained in case of body model 2 is more erroneous than in case of body model 1. This is due to the fact that the methods described are based on Born Approximation which treats the body to be weakly scattering whereas body 2 is a high contrast body and is highly scattering. The main practical challenge in these direct methods is to extract the phase information from the received signal. This requires sophisticated technologies like the use of vector analysers. Other challenge is the proper positioning of Tx and Rx in the far field region.

The future work will be to modify the above method so that reconstruction of high contrast bodies can be done with more precision.

REFERENCES

1. A.C. Kak and M. Slaney , "Principles of Computerised Tomographic Imaging" IEEE press, Ch-1,pg-1-4, *1999*

2. A.C. Kak and M. Slaney , "Principles of Computerised Tomographic Imaging" IEEE press, Ch-3,pg-60, *1999*

3. A.C. Kak and M. Slaney , "Principles of Computerised Tomographic Imaging" IEEE press, Ch-4,pg-134,137,158, *1999*

4. Max Born and Emil Wolf , "Principles of optics-Electromagnetic theory of propagation ,interference and diffraction of light", Cambridge University press,Ch-8,pg-695-703,*2005*

5. J.H.Richmond,"Scattering by a Dielectric Cylinder of Arbitary Cross-section Shape",IEEE transactions on Antenna and Propagation, vol. 13, No. 3, 334-341, *1965*

6. A.C. Kak and M. Slaney , "Principles of Computerised Tomographic Imaging" IEEE press, Ch-6,pg-208-214,218,137,158,234-247 *1999*

7. G.Gbur and E.Wolf," Relation between Computed and Diffraction tomography", J. Opt. Soc. Am. A/Vol. 18, No. 9/September 2001

8. C.F. Gerald and P.O. Wheatly,"Applied Numerical Analysis",Ch-5,pg-301,seventh edition ,Pearson.

9. Rudra Pratap,"Getting Started with Matlab 7",Oxford University Press

10. A.k. Kundu ,B.Bandyopadyay, "An Image Reconstruction and Enhancement Technique for Microwave Tomography",Abstract, ACTA TECHNICA CORVINIENSIS -Bulletin of Engineering

Modal noise improvement in 10-Gb/s offset launch in multimode fiber link with multimode fiber taper

Mike Nix
Department of Electrical and
Computer Engineering
Queen's University
Kingston, ON, Canada

Chen Qian
Department of Electrical and
Computer Engineering
Queen's University
Kingston, ON, Canada

Scott S.-H. Yam
Department of Electrical and
Computer Engineering
Queen's University
Kingston, ON, Canada
scott.yam@queensu.ca

Lisa Huff
Advanced Design and
Applications Data
Communications Competence
Center
Nexans Inc
New Holland, PA, USA

Abstract— **Implementing the newest IEEE 802.3 Ethernet standards and updating older systems to meet those standards requires the use of laser diodes to maintain a high bandwidth-distance product through the multimode fiber link. However, due to the high coherence of such sources, link performance can be severely impaired by modal noise. In this paper the use of a multimode fiber taper to reduce modal noise in a 220 or 300 m, 10 Gb/s IEEE 802.3aq-compliant link is investigated. It was found that by inserting the taper at the input of the multimode fiber link, modal noise improvement was seen at different single-mode transverse launch offsets with a maximum signal-to-modal-noise ratio improvement of 8 dB being observed.**

Keywords— multimode fiber, fiber taper, 10 GbE, modal noise

I. INTRODUCTION

With many emerging applications requiring increased data transmission rates, there is interest in updating older and installing new premise and local area networks to speeds beyond 1 Gb/s. The newest IEEE 802.3 Ethernet standards (802.3ae/aq) require 10 Gb/s transmission over 220 m of 62.5/125 μm legacy multimode fiber (MMF) or up to 300 m over newer 50/125 μm laser optimized fiber [1]. There is also work being done to vastly improve the bandwidth distance product of multimode fiber beyond the current 2,000 MHz.km towards 40 Gb/s and 100 Gb/s Ethernet [2.]

Traditionally, multimode networks used low cost LEDs as a signal source due to their low cost, but for the new Ethernet standards the modulation bandwidth of an LED is far too low.

As a result, laser diodes (LD) are being used in the newer MMF systems [1, 3-5]. However, because of the high coherence length of LDs compared to LEDs, a significant problem can arise: modal noise [6, 7]. Modal noise is due to a dynamic interference pattern between different transverse fiber modes caused by low frequency fiber fluctuations with a source of mode-selective loss (MSL) located somewhere in the fiber link. This mode-selective loss is usually due to connector offsets and it essentially filters out specific fiber modes. If the interference pattern is changing, different modes are being filtered by the MSL, and this results in power fluctuations that are ultimately seen at the receiver as noise on the signal [6, 7].

Previous work has demonstrated the ability for a fiber taper to improve MMF link performance by spatially filtering higher order modes [8]. However, it is not clear how this type of MSL will affect modal noise. In this paper, we investigate the effect of fiber taper on modal noise in systems employing coherent laser and laser optimized MMF links. By selectively removing higher order modes with significantly different group delays than lower order modes at the input of the MMF links, signal-to-noise ratio due to modal noise sees dramatic improvement from 2 to 8 dB at different offset launch positions. Thus, a simple and low-cost device could potentially relax the design specification for electronic dispersion compensation (EDC) integrated circuits for short reach MMF applications.

II. EFABRICATION OF MMF TAPER

A multimode fiber taper can be fabricated by slowly stretching a length of multimode fiber while simultaneously applying a strong heat source at a single point. For the taper to be ideal, it should be stretched sufficiently slowly so that it has a consistent shape along its length and low optical power loss. Assuming an exponential taper model9, the taper waist, d, is found to be d = D_0 exp{L/L_0} where D_0 is the original fiber diameter, L_0 is the length of the taper waist region and L is the length of the region of exponential decrease. Using a flame as a heat source, the length of the taper waist region, L_0, is solely determined by the width of the flame.
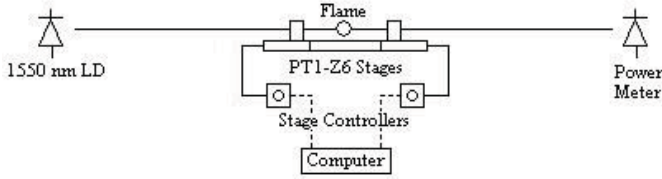
Fig. 1: Taper Fabrication Setup

To fabricate the taper, a propane burner and micro torch kit with a flow controller was used where the flame temperature reaches approximately 1800 ºC and the flame width was set to be 4 mm. Two computer-controlled Thorlabs PT1-Z6 motorized stages with fiber clamps were used to stretch the fiber at a translational speed of 0.3 mm/s. During the fabrication process, a 1550 nm laser diode and power meter was used to continuously monitor the insertion loss through the taper. Fig. 1 shows the taper fabrication setup.

After many trial fabrications a taper waist of five microns was decided on. This waist provided the taper with a low optical loss (< 1 dB) while allowing for easy fabrication with a high degree of repeatability.

III. GENERATING MODAL NOISE

For modal noise to be present in a multimode fiber link, the modal interference (or speckle) pattern present at the receiver has to be dynamically changing. This can be due to either low frequency vibrations present along the link or due to laser instability at the transmitter. A dynamic interference pattern itself does not cause modal noise because if enough modes are excited the received power will remain relatively constant. However, if there is a source of mode selective loss (such as offset connectors) that selectively filters out certain modes in the link, then the dynamic interference pattern will also result in dynamic power fluctuations.

To generate the modal noise in the multimode fiber link under test, the procedure described in TIA FOTP-142 [10] was followed. The mode selective loss generator was constructed from a 10 m long piece of multimode fiber. Located along the fiber, at 2, 6, and 10 m three mode selective loss locations were placed. Each one of these connections consisted of an offset splice such that there was 1 dB loss across the splice and the total loss through the mode selective loss generator

approximately 3 dB. To create the dynamic modal interference pattern, a 10 m length of fiber was coiled into a figure-eight configuration and then placed on an electric shaker such that as the shaker vibrated the fiber was flexed back and forth. The mode selective loss element combined with the fiber shaker allowed for the generation of modal noise in the multimode fiber link under test.

IV. EXPERIMENTAL SETUP

To measure the modal noise penalty of our multimode fiber link, the procedure and test setup as described in TIA FOTP-142 [10] was used to generate the MSL element and modal noise. All components used and measurements taken conform to this test procedure. Fig. 2 shows the final experimental setup. A 1550 nm laser diode with a 100 kHz line-width was used, although other wavelengths can be used as well. The Mach-Zehnder modulator (MZM) intensity modulated the output of the LD and the EDFA was used to compensate link loss and allow for meaningful measurements. The modal noise mechanism (MNM) in Fig. 2 consists of four elements arranged in five different configurations: A) 10 m fiber shaker, 10 m reference fiber; B) 10 m fiber shaker, 3 dB MSL; C) 10 m fiber shaker, 3 dB MSL, MMF Taper; D) 10 m fiber shaker, MMF Taper, 3 dB MSL; E) MMF Taper, 10 m fiber shaker, 3 dB MSL; where the MSL and fiber shaker are constructed as detailed above. The offset launch was done using a single mode fiber (SMF) aligned with a MMF using a six-axis nano-positioning stage with 37.5 nm resolution and 30 nm x-/y-/z-axis repeatability. To maintain offset accuracy, the stage was reset and homed after each measurement set. The transverse offset range was 0 – 24 µm from the MMF center axis in 2 µm steps. The taper was a 50/125 µm graded-index MMF tapered down to a diameter of 5 µm, with a measured insertion loss of only 1 dB as detailed above. The fiber under test (FUT) consisted of either a 220 or 300 m MMF made from the same preform. The optical receiver is MMF pigtailed with a bandwidth of 9 GHZ and the oscilloscope (OSC) used had standard compliant bandwidth of 12 GHz [10].
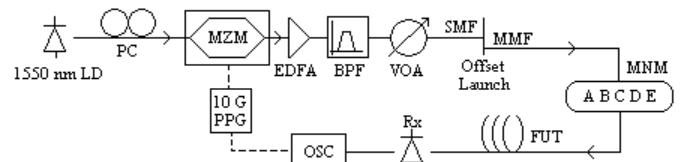
Fig. 2: Experimental Setup.

V. MEASURING MODAL NOISE

Using one of these ten configurations (A/B/C/D/E and 220/300 m FUT), the 10 m fiber shaker was set to oscillate at 8 Hz to create the modal noise in the link. To measure the amount of modal noise present in the link, FOTP-142 [10] was again followed. The modulator was set up to generate a simple periodic bit sequence of alternating ones and zeros. The optical signal was then received and the electrical signal

viewed on the oscilloscope. For ease of comparison, the output was then measured and the attenuator (VOA) was changed for each sample and transverse offset so that the peak-peak output voltage measured by the oscilloscope was 20 +/- 1 mV. The oscilloscope was then set up so that a voltage histogram measured a "1" or "0" value at the midpoint of the bit period where the modal noise distribution was assumed to be Gaussian with bin sizes of approximately 0.16 mV. The mean and standard deviation of the histogram were then measured, and the signal-to-modal-noise ratio (SMNR) was calculated using SMNR = 20 log (μ/σ), where μ is the mean value of the "1" and σ the standard deviation. This method was also used to collect data from the received "0". To ensure just modal noise was being measured, the output of the EDFA was filtered and the noise contribution of the pre-link configuration was found as above (which was insignificant) and then subtracted from the actual measurements. These measurements were taken for each of the ten possible configurations at lateral offsets ranging from 0 – 24 µm.

VI. Results and Discussions

Fig. 3 shows the SMNR of the received signal for a MMF length of 220 and 300 m for the first three configurations (A-C), and fig. 3 shows the SMNR for the last two configurations (D, E) compared to the reference fiber (A). Figs. 3 and 4 show just the "1" data; the data for the "0" points showed similar behaviour but were omitted for the sake of brevity. To compare the results between configurations, configuration A is considered to be the best case because there is no significant source of MSL (and thus very little modal noise), while configuration B is the worst case because it consists of just the MSL. Since the MSL is the center for modal noise generation[6], it was thought that placing the fiber taper after the MSL would have an effect on the modal noise. From Fig. 3, it can be seen that for 220 m the fiber taper (configuration C) generally improves the SMNR of the signal by at least 4 dB up until an offset of 14 µm. For the longer 300 m fiber there is only significant noise generated by the MSL for the middle offset range (10 – 14 µm) and there is improvement of almost 8 dB over that range. Comparing Fig. 4a to those shown in Fig. 3a, there is about 2 – 4 dB of SMNR improvement over the case with just the MSL (B) for the lower offset range (0 – 14 µm) with the 220 m fiber. For the 300 m MMF fiber, there is again only improvement seen for the middle offset range when compared to configuration B. That there is improvement for configurations D and E is an interesting result because they both have the taper placed before the MSL, which is the center for the creation of the modal noise. This in turn suggests that the use of a fiber taper at the beginning of an actual MMF link could be used to improve the total modal noise performance.
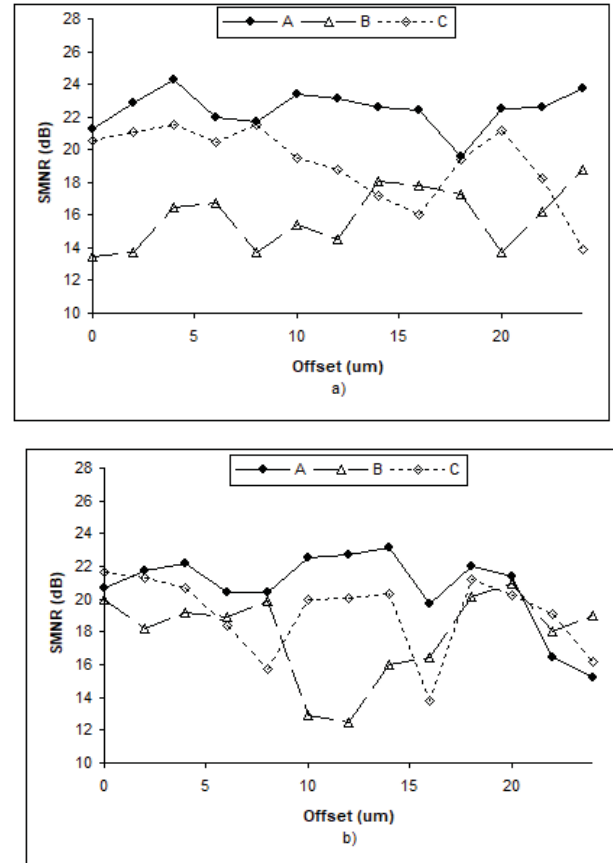
Fig. 3: SMNR results for configurations A, B, C with a) 220 m and b) 300 m MMF length.

To determine the repeatability of the measurements, data was collected at different transverse offsets for a continuous wave input and it was found that 90% of the 408 measurements taken fell within ±10% of the mean value for each offset. This level of repeatability is assumed to hold for the pulsed input case as well. During the experiment it was also found that the taper insertion loss changed with transverse offset. For the 200 m link the loss was 1 dB up until a 16 µm offset where it increased to almost 2 dB. For the 300 m link the loss was almost 7 dB for low offsets, reducing to 1 dB again for the middle offset range (10 – 14 µm).
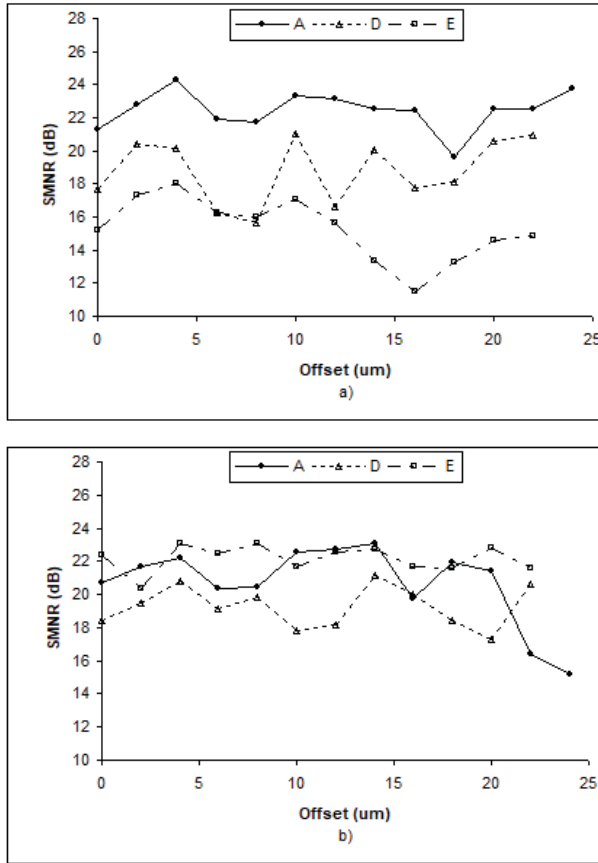
Fig. 4: SMNR results for configuration A, D, E with a) 220 m and b) 300 m MMF length.

The presence of insertion loss through the fiber taper as well as previous work [8] indicates that the taper acts as a modal filter, and because of this it can be considered a source of mode-selective loss which would degrade the modal noise performance. However, since it was found that the use of a fiber taper improves performance over a range of transverse offsets, this implies that there are unknown mechanisms inherent in high-speed MMF applications. Future work studying the effects of inline fiber tapers could potentially further our understanding of modal noise with directly modulated lasers and laser optimized MMF. Even if the modal noise performance is enhanced by only a small amount, since the 802.3aq power budget only allowed for 0.2 dB of modal noise [11], a fiber taper could be used to improve performance in particularly problematic systems.

VII. Conclusions

The use of a fiber taper is a novel method for reducing modal noise and in this study we have seen the effect a multimode fiber taper has on improving performance in a 220 or 300 m MMF link. For the 220 m link it was found that placing a fiber taper before or after the source of mode-selective loss (and thus the source of modal noise) resulted in an improvement in signal-to-noise ratio of 2 – 7 dB for a

transverse launch offset up to 14 µm when compared to a purely MSL configuration. A link length of 300 m showed significant noise generation for a launch offset of 10 – 14 µm and a maximum SMNR improvement of 8 dB was observed. Because placing a fiber taper at the input of a MMF link improves performance, a fiber taper could be used as an effective, easy to deploy and very inexpensive enabling component in high bit-rate MMF Ethernet applications.

References

[1] P. Ronco, J. Abbot. "10 Gb/s Solutions for Multimode Fiber Premises Networks." Corning Optical Fiber Guidelines. Vol. 13E, 2006.

[2] Yam, S. S-H., Achten F. "Toward 100 Gbits/s Ethernet with Broad Wavelength Window Multimode Fiber." J. Optical Networking. 6(5), 527-533 (2007).

[3] Papen, G. C., Murphy, G. M. "Modal Noise in Multimode Fiber under Restricted Launch Conditions." J. Light. Tech., 17(5), 817-822 (1999).

[4] Webster, M. et al. "A Statistical Analysis of Conditioned Launch for Gigabit Ethernet Links Using Multimode Fiber." J. Light. Tech., 17(9), 1532-1541 (1999).

[5] Wegmuller, M. et al. "Evolution of the Beam Diameter in a Multimode Fiber Link Through Offset Connectors." IEEE Phot. Tech. Letters, 13(6), 574-576 (2001).

[6] Epworth, R. E. "Modal Noise – Causes and Cures." Laser Focus with Fiber Optic Technology. 109-115 (1981).

[7] Pepeljugoski, P. et al. "Modal Noise BER Calculations in 10-Gb/s Multimode Fiber LAN Links." IEEE Phot. Tech. Letters, 17(12), 2586-2588 (2005).

[8] Moon, S. and Kim, D. Y. "Effective Single-Mode Transmission at Wavelengths Shorter Than the Cutoff Wavelength of an Optical Fiber." IEEE Phot. Tech. Letters, 17(12), 2604-2606 (2005).

[9] Kenny, R. P., Birks, T. A., Oakley, K. P. "Control of Optical Fiber Taper Shape." Electronics Letters, 27(18),   1654-1656 (1991).

[10] "Measurement of modal noise power penalty for laser sources." FOTP-142, TIA/EIA SC FO-5.6, 6/14/99.

[11] Cunningham, D. et al. "Modal Noise and Implications for the CSRS Test." Presented at the IEEE P802.3aq 10GBASE-LRM Task Force meeting,   March   2006.   [Online].   Available: http://www.ieee802.org/3/aq/public/mar06/cunningham_1_0306.pdf

[12] Couch, P. R., Epworth, R. E. "Reproducible Modal-Noise Measurements in System Design and Analysis." J. Light. Tech. 1(4), 591-596 (1983).

[13] Epworth, R. E. "The Phenomenon of Modal Noise in Fiber Systems." in Proc. Topical Meeting Opt. Fiber Commun. (1979).

Design and Analysis of Magnetic Tunnel Junction Based Random Access Memory Cell

Ankit Singh Kushwah

Department of ECE
Institute of Technology and Management
Gwalior, India
akushwah13@gmail.com

Shyam Akashe

Department of ECE
ITM University
Gwalior, India
shyam.akashe@itmuniversity.ac.in

Abstract— **In this report, we presented an NV Random Access Memory cell using a novel easy and proficient model of Spin Transfer Torque Magnetic Tunnel Junction (STT-MTJ). Magnetic tunnel junction (MTJ) devices are CMOS well suited with high steadiness, high dependability and non-volatility. The combination of magnetic tunnel junction with CMOS circuits in magnetic RAM (MRAM) or Magnetic FPGA can get the digital circuits to major advantages related with non-volatile facility like immediate on/off, Zero standby power use of goods and services. MTJ (Magnetic Tunnel Junction) devices have various advantages over other magneto-resistive devices for use in MRAM cells, like MRAM produces a big signal for the read operation and a varying resistance that can make the circuit. Due to these attributes, MTJ-MRAM can operate at high velocity. A completed simulation model for the 5T and 2MTJ SRAM design is shown in this report, which is grounded on the recently confirmed STT (Spin-Transfer Torque) writing technique which promises to take down the switching current losing to ~150μA and the STT RAM cache reduces total power consumption from 44.6μW -13.2μW. This model has been confirmed in Verilog A language and the whole work carried out and ran out on cadence virtuoso platform at 45nm.**

Keywords— Non-volatile; STT-MTJ; MRAM; High speed; Magnetic logic.

I. INTRODUCTION

Withering of the complementary metal-oxide semiconductor (CMOS) fabricated node below 90nm, the high supply power due to rising leakage currents becomes a more and more significant subject. This upgrade power use of static random access memory (SRAM) based low rank cache memory shows the harshest problem in superior processor particularly used for battery used computing devices. To master these problems a quantity of non-volatile storage technologies such as Magnetic RAM (MRAM), Ferroelectric RAM (FRAM), Phase-Change RAM (PCRAM) and Resistive RAM etc. are under examination. These devices are expected to over the above problem in the CMOS logic circuit and take the non-volatility into the CMOS logic circuit and permit them to completely power OFF. All the data are confined and can be retrieved immediately on Active state. This technique could overcome the standby power issue and allow the

Circuits and technology to be further shrunk down. MTJ (Magnetic Tunnel Junction) is considered as one of the most hopeful rising technologies to overcome the high leakage power issue of CMOS circuits and MTJ circuit also provide non volatility unbounded endurance and fast random access. In Magnetic Tunnel Junction it is one of the most gifted storage technologies, that features non volatility, high read/write speed, large withholding up to 10 years and it permits also more than 10^{12} reprogramming cycles.

A. MOTIVATION FOR STT-RAM

Presently, three cases of memory exist, Static RAM (SRAM), Dynamic RAM (DRAM), and Flash memory. SRAM has superb read and write speeds, but holds a very large cell size (requiring 6 or more transistors per cell). The speed of SRAM makes it rather suited for embedded applications, particularly cache memory, where execution is key than memory density. SRAM is volatile, but takes

very little active power for data retention. DRAM is able to offer much better storage density through its function of a single transistor with a storage capacitance. Even so, the capacitor leak off the charge and refresh the cycle after every few milliseconds. DRAM is typically used as the primary memory system in a computer, where memory density and public presentation are more significant in comparison to power using up. Flash memory technologies for fluid applications in which high volatility and very high densities are required. While Flash does have reasonably quick read access times, but very slow write speeds and endurance rates are really low (< 100,000 cycles). To sustain the power, performance and control the effectiveness of cost we use a typical organization that incorporates all the advantages of SRAM, DRAM and Flash memory called Magneto resistive RAM. Such a memory would reduces the need of multiple applications definite memories, and getting better system performance and reliability, while also reducing costs and power use of goods and services. MRAM based on the idea of way of magnetization to store binary information and exploit magneto resistive properties to retrieve the data [8].

TABLE I.   COMPARISION OF MEMORY TECHNOLOGIES

	SRAM	DRAM	FLASH (NOR)	FLASH (NAND)	STT-MRAM
Non-Volatile	NO	NO	YES	YES	YES
Read Time (ns)	1-100	30-100	10	50	2-20
Write Time (ns)	1-100	15	1µs/1ms	1ms/0.1ms	2-20
Cell Size	50-120	6-10	10	5	6-20

II.   MTJ TECHNOLOGY

MTJ circuits can be switch generally in three modes: field induced magnetization switching (FIMS), thermally assisted switching (TAS) and spin torque transfer (STT). FIMS is used in the first generation of MRAM, which was successfully commercialized. However, the high switching power expenses, large switching area, and bad cell selection performance of the conventional MRAM writing approach Field-Induced Magnetic Switching (FIMS) is not good with future respect. And in other side another switching approach, Thermally Assisted Switching (TAS) -MRAM promises to lower the reconfiguration latency and enhance the writing selectivity, but it is also not good for future because decrease the chip area and programming power due to the comparatively high switching current and the heating current. To overwhelm all these drawbacks of FIMS and TAS technologies we developed a novel technology called STT RAM [4].

TABLE II.   COMPARISION OF STT-MTJ TECHNOLOGIES

MTJ Device	SPEED	AREA	POWER
FIMS-MTJ	High	Large	Very High
TAS-MTJ	Medium	Medium	Medium
STT-MTJ	High	Small	Low

A. Spin Transfer Torque MTJ

In MTJ (magnetic tunnel junction) it have two ferromagnetic layers and one oxide barrier layer, e.g., MgO. The resistance of MTJ can be judge by the magnetization information of ferromagnetic layer with spin direction: when the direction of magnetization of spin is parallel (anti-parallel), MTJ is in low (high) resistance state. In STT-RAM design, the magnetization order of one ferromagnetic layer (reference layer) is developed by matching to a pinned magnetization layer while the magnetization order of the other ferromagnetic layer (free layer) can be altered by going across a switching current polarized by the magnetization of the reference layer [10].
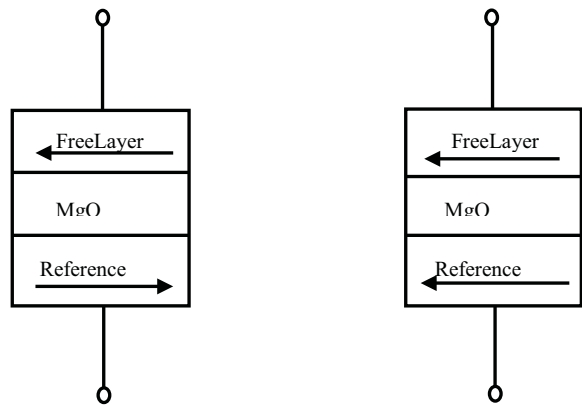
Fig. 1. MTJ Structure (a) Anti-Parallel (high resistance state). (b) Parallel (low resistance state).

The value taken as '1' if the directions of layers are parallel and MTJ shows low resistance and a '0' if the direction read as anti-parallel and MTJ shows high resistance or vice versa for negative sense. The MTJ shows low resistance when the two layers (free layer and reference layer) are magnetized in the same and it offers high impedance when the direction of magnetization of both the layers is opposite, named the "ant parallel state". Figure shows the states of an MTJ in high resistance mode or low resistance mode. In MRAM cell an NMOS transistor is added to form a NMOS as a read transistor in series with the MTJ. Fig.2, bit-line linked to the bit cells as bit-line (BL), source-line (SL) and word-line (WL). The data is read as '1' if the MTJ shows low impedance and a '0' if the MTJ shows high impedance or vice versa for negative logic.
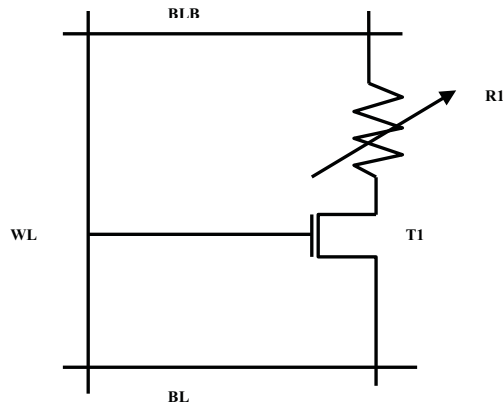
Fig. 2. 1T 1R STT-MRAM cell structure

The memory component in an STT-MRAM cell is a magnetic tunnel junction (MTJ), It is used as a variable resistance. A characteristic single-transistor-one-resistor (1T1R) STT-MRAM cell is presented in Figure 1. The access transistor is in serial publication with the MTJ. To scan the cell, the word line (WL) makes high and the impedance of the MTJ is determined. To write the cell, the word line makes high and the cell is forced by a write current. The centring of the write current determines the value of the bit written to the cubicle.
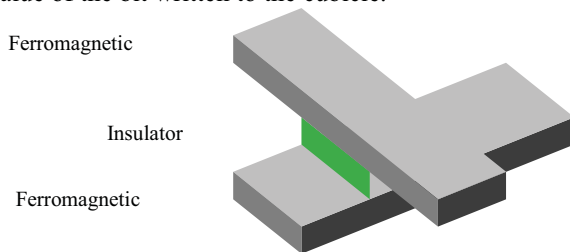
Fig. 3 Basic structure of an MTJ

III. 5T-2MTJ BASED NV-SRAM CELL

To overcome the difficulties of non-volatility in planar CMOS transistor based SRAM uses a new style of the 4T-2MTJ based SRAM cell, in which MTJ (Magnetic Tunnel Junction) is a variable resistance whose equivalent circuit shown above in figure (3). MTJ switches in two modes, (1) Parallel mode (low impedance state) and (2) anti-parallel fashion (high impedance state). The information is read as '1' if the MTJ offers low impedance and a '0' if the MTJ offers a high resistance or vice versa for negative logic. The Schematic of 5T-2MTJ based SRAM cell shown below.
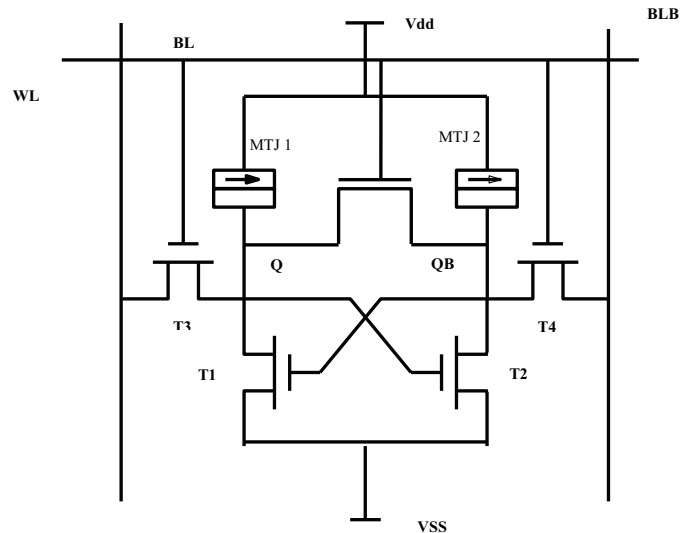
Fig. 4. 5T-2MTJ NV-SRAM

A. Non-volatile SRAM modes of operation

Non-Volatile SRAM cell shows the following basic ways of functioning:

Data retention or Standby mode: An SRAM cell is capable to hold the information indefinitely.

- Read mode: An SRAM cell is capable to exchange its stored information. This procedure does not impress the data, i.e., read operation is non-destructive as compared to DRAM's read operation.
- Write mode: The records of an SRAM cell can be arrange to any binary value, disregarding of its original stored value.
- Cell Operation: We can carry out both read or write operation on the mobile phone. For write operations two signals will be produced from the input data one is 'BL' and another is 'BLB'. Where BL = data and BLB = complement of information. Then word line (WL) goes high which makes on the operational transistors and the information will be penned in the cubicle. For a read operation both 'Bit Line' and 'Bit Line Bar' lines are pre-charged to voltage level "v" and then 'Word Line' goes high, since SRAM has been already either in state '0' or in '1', then, granting to the nation only one line discharges to Ground and a voltage difference developed between 'Bit Line' and 'Bit Line Bar' lines. This conflict will be sensed by sense amplifier and at last stored bit will be available at the output of sense amplifier.

IV. POWER CONSUMPTION

The total power of the circuit results the power dissipation across entire circuit. And it can state as:-

$$P_{total} = P_{dyn} + P_{static} \qquad (1)$$

P_{dyn} represents dynamic power dissipation through capacitance due to charging/discharging when a transition makes occur through the output signal of a logic gate. P_{static} is the static power consumption which occurs due to the leakage current whose major elements are the sub threshold leakage, gate direct tunnelling leakage, and junction band-to-band tunnelling leakage [8].

In general it express as

$$P = I * V \qquad (2)$$

Power using up in any digital integrated circuit, is afforded by the equation

$$P_{total} = I_o V + \alpha C V^2_{dd} f \qquad (3)$$

Where, I_o is the leakage current, which is regulated by the diode equation $I_s (e^{qv/kT} - 1)$, V_{dd} is the power supply voltage, α shows the characteristic of average switching activity factor, The total capacitance of the circuit represents by C, and f shows the frequency of operation. The first term of the equation shows the leakage power and the second term shows the dynamic switching power. With the reduction in features sizes, Vdd has also fallen and the threshold voltage V_t of the transistor trying to reduce. So the leakage current Io, which depends on V_t, given by diode equation increases [9]. A more detail expression for sub threshold leakage [11].

$$Isub = A * exp \left(\frac{q}{n'KT}(Vg - Vs - Vtho - \gamma Vs + \eta Vds)\right) * B \qquad (4)$$

Where, $A = \mu \, Cox \frac{Weff}{Leff} \left(\frac{KT}{q}\right)^2 e^{1.8} \qquad (5)$

$$B = 1 - exp \left(\frac{-qvds}{KT}\right) \qquad (6)$$
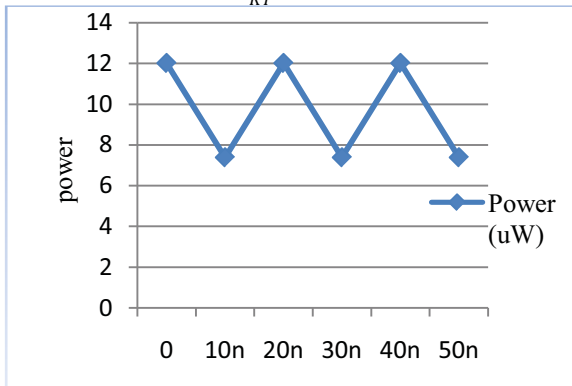
Fig. 5. Power consumption graph

V. CELL DELAY

The propagation delay times τPHL and τPLH can be evaluated by the input-to-output signal delay during the high-to-low and low-to-high transitions of the signal, respectively. In which, τPHL is the time delay between the $V_{50\%}$ transition of the rising input voltage and the $V_{50\%}$ transition of the falling output voltage. Similarly,

τPLH is defined as the time delay between the $V_{50\%}$ transition of the falling input voltage and the $V_{50\%}$ transition of the rising output voltage. To analysis and calculate the derivation of delay expressions, the input voltage waveform is generally understood to be an ideal step pulse with zero rise and fall times. Under this assumption, τPHL becomes the time required for the output voltage to fall from VOH to the $V_{50\%}$ level and τPLH becomes the time required for the output voltage to rise from VOL to $V_{50\%}$ level [13]. The voltage at point $V_{50\%}$ level defined as follows:-

$$V_{50\%} = VOL + \frac{1}{2}(VOH - VOL) = \frac{1}{2}(VOH + VOL) \qquad (7)$$

The average propagation delay τp of the inverter shows the average time taken for the input signal to distribute through the inverter.

$$Tp = \frac{\tau PHL + \tau PLH}{2} \qquad (8)$$

TABLE II. COMPARISION OF DELAY

Parameter	5T-2R SRAM	5T-2MTJ RAM
Delay	21.54 E-9	20.34 E-9

VI. STATIC NOISE MARGIN (SNM) MEASUREMENT

The static noise margin (SNM) of SRAM cell is put as the minimum DC noise voltage required to throw the cell state.e. SNM of an SRAM cell is a widely-used intends metric that evaluates the cell stability. The measured results when plotted are called "butterfly curve". The butterfly curve can obtain by the following technique with the test circuit: 1) Word line (WL) is biased at the ground and bit lines (BL, BLB) are biased at VDD. 2) The voltage of N1 is change from 0 V to VDD while measuring voltage of QB. 3) The voltage of N2 is changes from 0 V to VDD while measuring voltage of Q in the same path. 4) Now calculated voltages are plotting to obtain a butterfly curve [12].
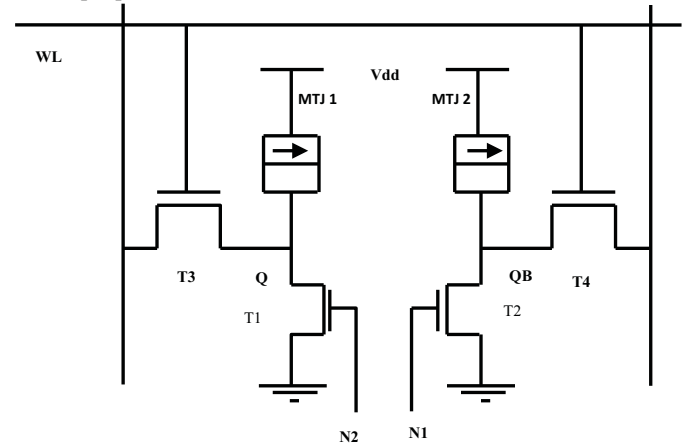
Fig. 6. Test setup for measuring SNM

Above shown schematic shows a trial setup for measuring SNM. After simulating above schematic a butterfly curve is held. The side length of Maximum Square that can be accommodated inside the smaller wing of the butterfly curve represents the SNM of the cell.
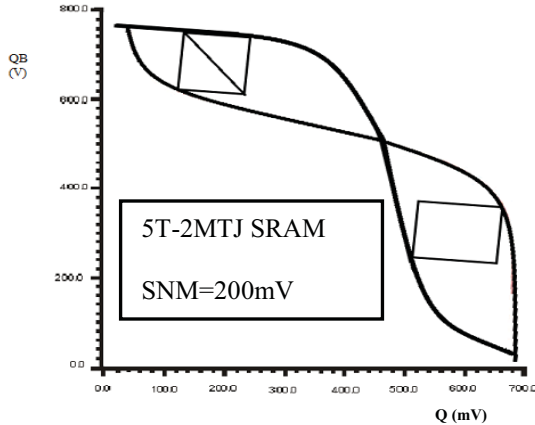
SNM influences both the read and write margin, is associated to the threshold voltage of the PMOS and NMOS devices in SRAM cells. Static noise margin (SNM) of the SRAM Cell affected by the cell ratio (CR), supply voltage, and pull up ratio (PR). The value of SNM should be high for stability of SRAM cell and that depends on cell ratio, pull up ratio and supply voltage. Cell ratio shows the ratio across the sizes of the driver transistor to the access transistor for the period of read operation. Pull up ratio makes fixed as the proportion between the sizes of the access transistor to the load transistor for the period of write operation. The SNM of the circuit is determined by the smallest diagonal of the two maximum squares that can he fit across the cross section of the VTC diagrams of the cross-coupled inverters. The SNM of SRAM is calculated and it is 0.184 V, shown in figure 7.

$$SNM = \sqrt{((NMH)^2 + (NML)^2)} \qquad (9)$$
$$N_{MH} = V_{OH} - V_{IH} \qquad (10)$$
$$N_{ML} = V_{IL} - V_{OL} \qquad (11)$$

VII. COMPARISION OF RESULTS

Parameter	5T–2R SRAM	STT-MRAM
Non-Volatile	No	Yes
Delay	21.54 E-9	20.34 E-9
Total Power	32 E-6	44.6 E-6
SNM	~150	~200mv

VIII. CONCLUSION

In this report, we introduced the characteristics results on the 5T-2MTJ based RAM cell under different facets. MTJ base circuit show one of the most gifted emerging technologies to defeat the high leakage power issue of CMOS circuits and MTJ circuit also provide non volatility, fast random access and infinite endurance. This work carried out on cadence tool, in device design and optimization such as different characteristic parameter profile in 0.7V supply voltage at 45nm technology and gets better result as compared to conventional 5T-2R SRAM. The calculated results indicate that the circuit based on 4T-2MTJ shows non-volatility, power reduction up to 44.6 E-6 and increases the stability in comparison of 5T-2R based SRAM up to ~200mV.

ACKNOWLEDGEMENT

REFERENCES

1. Mayank Chakraverty, Harish M. Kittur, P. Arun Kumar. First Principle Simulations of Various Magnetic Tunnel Junctions for Applications in Magneto resistive Random Access Memories. IEEE Transactions on Nanotechnology, vol. 12, no. 6: pp. 971-977, Nov. 2013

2. Chika Tanaka, Keiko Abe, Hiroki Noguchi, Kumiko Nomura, Kazutaka Ikegami, Shinobu Fujita. Normally-off type nonvolatile static random access memory with perpendicular spin torque transfer-magnetic random access memory cells and smallest number of transistors. Japanese Journal of Applied Physics, vol. 53, 04EM07, Mar 2014.

3. Zhenyu Sun, Xiuyuan Bi, Hai (Helen) Li, Weng-Fai Wong, Xiaochun Zhu. STT-RAM Cache Hierarchy With Multiretention MTJ Designs. IEEE Transactions on Very Large Scale Integration (VLSI) Systems, vol. 22, pp. 1281-1293, Jun 2014.

4. Yi Gang, Weisheng Zhao, Jacques-Olivier Klein, Claude Chappert, Pascale Mazoyer. A High-Reliability Low-Power Magnetic Full Adder. IEEE Transactions on Magnetics, vol. 47, no. 11, pp. 4611-4616, Nov. 2011.

5. Leem L, Harris james S. Magnetic coupled spin torque devices for non-volatile logic applications. Journal of applied physics, vol. 105, issue 7, pp. 07D102 - 07D102-3, Apr. 2009

6. Weisheng Zhao, Eric Belhaire, Claude Chappert. Spin Transfer Torque (STT)-MRAM–Based Runtime Reconfiguration FPGA Circuit. ACM Transactions on Embedded Computing Systems, vol. 9, no. 2, article 14, Oct. 2009.

7. Shyam Akashe, Sushil bhushan, Sanjay Sharma. High Density and Low Leakage Current Based 5T SRAM Cell Using 45 nm Technology. Romanian Journal of Information Science and Technology, vol.15, no.2 : 155-168, 2012.

8. Stuart A.Wolf, Jiwei Lu, Stan M.R, Chen E, Treger D. M. The Promise of Nonmagnetic and Spintronics for Future Logic and Universal Memory. Proceedings of the IEEE, vol. 98, no. 12, pp. 2155-2168, Dec. 2010,.

9. Hiwa Mahmoudi, Viktor Sverdlov, Siegfried Selberherr. MTJ-based Implication Logic Gates and Circuit Architecture for Large-Scale Spintronic Stateful Logic Systems. Proceedings of the IEEE conference on the European Solid-State Device research conference, pp. 254-257, Sept. 2012.

10. T. Kawahara, Takemura R, Miura K, Hayakawa J, Ikeda s, Lee Y, "2Mb Spin-Transfer Torque RAM (SPRAM) with Bit-

by-Bit Bidirectional Current Write and Parallelizing-Direction Current Read. Proceeding of the IEEE International Conference on Solid-State Circuits, pp. 480-617, Feb. 2007.

11. Mahadevan Gomathisankaran, Akhilesh Tyagi. WARM SRAM: A Novel Scheme to Reduce Static Leakage Energy in SRAM Arrays. Proceedings to IEEE Computer Society Annual Symposium on VLSI Emerging Trends in VLSI Systems Design (ISVLSI'04), pp. 105-112, Feb. 2004.

12. Aminul Islam, Mohd. Hassan. Variability Analysis of 6T and 7T SRAM Cell in Sub-45nm Technology. IIUM Engineering Journal, vol. 12, no. 1, 2011.

13. Shyam Akashe, Sanjay Sharma. Design of SRAM Cell Based Memory Array in Nano-Scaled Technology. Journal of Computational and Theoretical Nano-science, vol. 10, pp. 1–7, 2013.

14. Shyam Akashe, Sanjay Sharma. High density and low leakage current based SRAM cell using 45 nm technologies. International Journal of Electronics, pp. 1-17, Jun 2012.

15. M. El Baraji, V. Javerliac, W. Guo, G. Prenat, B. Dieny. Dynamic compact model of thermally assisted switching magnetic tunnel junctions. Journal of Applied Physics, vol. 106, pp. 123906(1-6), 2009.

16. J.-B. Kammerer, L. Hebrard, M. Hehn, F. Braun, P. Alnot, A. Schuhl. Compact modeling of a magnetic tunnel junction using VHDL-AMS: computer aided design of a two-axis magnetometer. Proceeding of IEEE Conference on Sensors, vol.3, pp. 1558-1561,

17. Weisheng Zhao, Lionel Torres, Yoann Guillemenet, Luis Vitorio Cargnini, Yahya Lakys, Jacques-Olivier Klein, Dafine Ravelosona, Gilles Sassatelli, Claude Chappert. Design of MRAM based Logic Circuits and its Applications, pp. 431-436, May 2011.

18. Rishubh Garg, Deepak Kumar, Navneet Jindal, Nandita Negi, Chetna Ahuja. Behavioural model of Spin Torque Transfer Magnetic Tunnel Junction, Using Verilog-A. International Journal of Advancements in Research & Technology, vol. 1, pp. 1-7,, Nov. 2012.

Smart Shopping Card

Khushi Arora, Parnika Gupta, Shefali Chopra,

khushi.arora87@yahoo.com, parnikakg2013@gmail.com, dracad@mru.ac.in
Department of Electronics and Communication
Manav Rachna University, Faridabad

Abstract—**This paper introduces SMART SHOPPING CARD, an easily accessible shopping card which makes shopping easier and simple. It has been designed using RFID, arduino, zigbee module, lcd display and keypad. The RFID technology is used as it helps in identifying as well as tagging and arduino is used as a microcontroller that is brain of the system. This card helps in reducing time of the customer during shopping. The system do not involve more of finance as well as labour work. Accessing the system for a customer is easy so no labour as such is required. Moreover, zigbee module used in the system helps in keeping account as well as stock information. The system can be further improved with addition of more features which makes shopping more simple and efficient.**

Keywords—*Arduino, RFID technology, LCD display, keypad and zigbee module.*

I. INTRODUCTION

Shopping is something on which a human spends most of his time every day. According to the researches done by researchers it is seen that people spend 23% of their lives on buying different products, that means we spend more than 150 hours per month and 2000 hours per year on shopping. In any condition, better or worse people will always need their necessities to live a comfortable life. They need food, groceries, clothes and other stuff for living. Since shopping is an important part of necessities of human, so it is necessary to optimize a better and comfortable way to do shopping. Today shopping can be simplified into two categories: 1) shopping in-person 2) shopping absentia. Shopping in absentia includes online shopping, tele-shopping etc where the shopper is not physically present in the shopping area. Shopping in-person involves shopping in shopping area where the person has to select the products according to the need. In shopping absentia, the person doesn't have to face a lot of issues as compared to that in shopping in-person. When a person enters a grocery store then he has to face lots of problems. He has to carry a cart

for keeping the material in it. So he has to roam all around the store to collect the stuff which requires a lot of time. Then after the collection of the material he has to stand in queue for the billing. He has to communicate with the shopkeeper which sometimes leads to fights. So a system is the need of the alarm to improve the way to do shopping. We need to organize a proper system in which people can buy their necessities in a proper comfort manner. A system in which their time during shopping is saved and they don't have to wait in queues. They should not feel shopping necessity as a headache. The proposed smart card system assist shopping in-person which will reduce the time spent in shopping and helps in store management too. The proposed system is based on very few technologies: 1) RFID for product identification 2) Zigbee for wireless communication with the shop server 3) Integrated system with display 4)Arduino . All these are being discussed in details in further sections. In this paper, we discuss design, working and conclusion of the smart card. In design, we discuss all the technologies used in building the card and in working section, we discuss the proper working of the smart card from how it reduces the shopping time till its contribution in store management. In conclusion, we discuss about the advances that can be done in the card to make it more commercial and helpful. The development opportunities are also focused so that it makes pleasurable shopping experience for the shopper and also makes the management of store easier.

II. SURVEY

While doing the survey we found that mostly people prefer leaving malls instead of waiting in line for checkout. People find it difficult to search for the required product too. After getting the product they have to stand in big queues for billing to be done .In recent years it has been seen that technologies has been used for overcoming these

public issues. Barcodes are found to be used today in every product. Barcodes are the universal technology used for retail products, stores that own barcode reader can process barcode and imprint it on the product. The most important fault with barcode scanning is that the product has to be at line of sight of the reader to get the barcode imprinted on the product scanned. The University of Arkansas Information Technology Research Institute, in 2009 came up with the business value of RFID item- level tagging for day to day operations at major luxury retailers. They demonstrated that overall inventory accuracy improved by more than 27 percent, under stocks decreased by 21 percent, and overstocks decreased by 6 percent. The study also compared how long it took to count items using RFID vs. a barcode reader. With RFID, scanning 10,000 items took two hours; scanning with a barcode reader took 53 hours. This translated into an average of 4,767 counted items per hour using RFID, and 209 items per hour using a barcode system—a 96 percent reduction in cycle-counting time. Public awareness of RFID was heightened in recent years when the U.S. Department of Defense (DoD) and retail giant Wal-Mart required their suppliers to use RFID technology. Bill McBeath in April 2013 said, to survive in 2013 and beyond, retailers need to make it easy for consumers to buy anywhere, receive anywhere, and return anywhere. The key to this cross-channel order promising is the ability, in real-time, to locate and allocate available inventory from any location, whether in the store, in DCs, in transit, or on order from the manufacturer. This requires having a very accurate, real-time, item-level picture of inventory at all these sources. RFID has proven to improve perpetual inventory accuracy in stores dramatically, by 20%-30%. JC Penney improved perpetual inventory accuracy from 75% to 99% in categories using RFID.

Khushi arora and parnika gupta, under the guidance of Mrs. Shefali chopra in their paper RFID and ARDUINO based shopping card described the implementation of a system to allow a simple and easy way of shopping. When arriving at the supermarket counter, the consumer issues a shopping card by getting it charged with some amount of money. The card is accessible to the RFID and ARDUINO designed system. The system consists of all the data of the items in the supermarket. The consumer only has to interact with the monitor designed with the transparent technologies. In the paper, we display the efficient and cost effective way of shopping for the consumer as well as the seller.

III. PROPOSED SYSTEM

We discuss the "SHOPPING CARD" designed to assist a person in everyday shopping in terms of reduced time spent while purchasing a product. Moreover this product helps the owner of the shopping area by reducing the cost involved in workers as the card requires less of man labor as compared to other way of shopping. The main objective of this project is to provide a technology oriented, low cost, scalable and rugged system for shopping in-person. The system consists of 4 key components 1) RFID technology 2) Arduino, 3) Integrated system with display and 4) Zigbee for wireless communication with shop server. Traditionally, RFID was used to track inventory along supply chains, retailers placed RFID tags onto pallets. The usage of barcode for product identification presents several limitations: only the product's class is identified; information is static; allows one single reading at a time; requires line-of sight; has low range and security. RFID technology is more resistant, safer, identifies products in a unique way, can provide other types of information, can make several simultaneous readings, doesn't need line-of-sight and it has a high range Now this automatic system hardware and software. Arduino acts as a brain of the system. Despite of other microcontrollers, arduino is not limited to windows only infact it runs on windows, macintosh OSX and linux operating systems. The zigbee module used helps in server and car communication. And even helps in creating a record of the product. The display helps in knowing the operation to be taken place and even acts as a medium of communication for the customer as proved later. overcomed the problem of line of sight of the reader. RFID gave 99.5% accurate result. Moreover the system is able to lower the labor cost giving significantly increase in inventory visibility. With RFID customers can enjoy speedier checkouts and greater convenience. Arduino used is an open source prototyping platform based on easy to use

IV. SYSTEM ARCHITECTURE
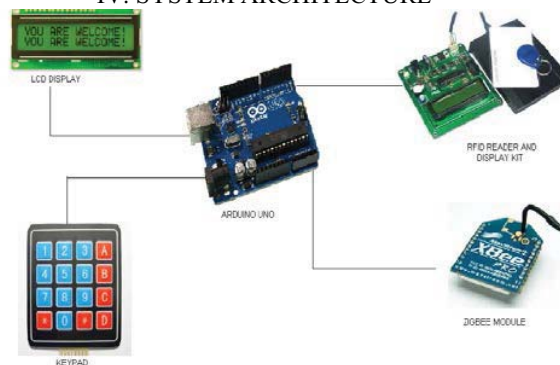
The modules components used in the architecture of the system are :
1) RFID technology
2) Arduino
3) Zigbee module
4) Lcd display
5) Keypad

1. RFID TECHNOLOGY

1) RFID stands for radio frequency identification. It is the wireless use of electromagnetic fields to transfer data, for the purpose of automatically identifying and tagging tags attached to the objects. The tags contain electronically stored information. And some tags are powered by electromagnetic induction for magnetic fields produced near the reader. Unlike the barcodes, tag does not necessarily need to be within the line of sight of the reader and may be embedded in the tracked object. RFID is one method of automatic identification and data capture. RFID provides a way for organization to identify and manage tools and equipments without manual data entry. RFID is being adopted for item level tagging in retail stores. This provides electronic article surveillance and self checkout process for consumer

2. ARDUINO

The UNO is a microcontroller board based on ATmega 328P. It has 14 digital input/output pins, 6 analog inputs, a 16 MHZ quartz crystal, a USB connection, a power jack, an ICSP header and a reset button. It contains everything needed to control a microcontroller, simply connect it to a USB cable or power it with a AC to DC adapter or battery to get started. UNO can be programmed with Arduino software. The UNO has number of facilities for communicating with a computer, Uno board and other microcontrollers. So, these functions of ARDUINO UNO acts resourceful for the shopping card.

3. ZIGBEE MODULE

The technology defined by the zigbee specification is intended to be simpler and less expensive than the personal area networks such as Bluetooth or wifi. Applications include wireless light switches, electrical meters for in-hopme displays, traffic management systems and other consumer and industrial equipment that requires short range low-rate wireless data transfer. Its low power consumption limits transmission distances from 10-100 meters line of sight depending upon power output and environmental characteristics. Zigbee device can transmit data over a long distance by passing it through a mesh network of intermediate devices to reach more distant ones. Zigbee is typically used in low data rate applications that require long battery life and secure networking.

4. LCD DISPLAY

A liquid crystal display is a flat panel display or other electronic visual display that uses light modulating properties of liquid crystals. Liquid crystals do not emit light directly. LCDs are available to display arbitrary images or fixed images with low information content, which can be displayed or hidden such as present words, digits and 7 segment displays such as in a digital clock. LCDs are used in wide applications of computer monitors, televisions, instrument panels, aircraft cockpit display and signage. The LCD screen is more effective and can be disposed of safely than CRT.

5. KEYPAD

A keypad is a set of buttons arranged in a block or pad which usually bear digits and symbols and a complete set of alphabetical letters. If it mostly contain numbers then it can also be called numeric keypad. Keypads are found on many

alphanumeric keyboards and on other devices like calculators, push button telephone, combination locks and digital door lock which require mainly numeric input.

V. WORKING

1.When the customer enter the mall , the customer need to get the shopping card recharged with required amount of money.

2.The space with the items have a number of RFID readers, the customer need to show the item tag on RFID for reading.

3.The customer will be asked for the number of such item required then using keypad he need to enter the needful information.

4.The reader will tell the total amount of the items and the customer with the help of card and keypad enter the amount so that the payment from the card get deducted .

5.This whole data of customer get stored in the main counter of mall to avoid mishappenings through zigbee module   used in the complete circuit

V.BENEFITS OF SHOPPING CARD

1.Reduces time by not letting the customer wait in queue for payments.

2.Reduces the requirement for workers in a shopping centre which is good for owners as they do not have to invest more in salaries.

3.Easy to check stock of the items since the purchased data get gathered in the web.

4.Easily accessed by anyone of any age.

5.Reduces the chances of cheating.

6.The card is renewable as it can be charged as much as required by the customer.

VI. CONCLUSION

Waiting in a queue for billing of the item intakes a lot of time. Not only this, the mall need to invest more in salaries of the workers working in the mall for making the bill and keeping the stock. With this proposed card all such problems get solved with low investment and time as it does not involve more of electronics which is costly. We are further working on this system by modifying the shopping card and trying in making it more resourceful with more additional features like use of credit cards. We are trying to add credit card feature with the RFID reader so that the payment option increases. We are working on this to make it more commercial.

REFERENCES

1.Swati Zope, Prof. .Maruti Limkar, "RFID based Bill Generation and Payment through Mobile",
International Journal of Computer Science and Network (IJCSN), Volume 1, Issue 3, June 2012

2. G. Roussos and B. College, "Enabling RFID in Retail", Computer, IEEE, vol. 39, no. 3, 2006, pp. 25-30.

3. Cisco Internet Business Solution Group survey document, My Shopping My   Survey   Findings, http://www.cisco.com/web/about/ac79/docs/retail/Mashop-surveymetricsUNITED

4.American Time Use Survey http://www.bls.gov/tus/charts/

5. D.V.S Chandra Babu, "wireless intelligent billing trolley for supermarket", International Journal of Advanced Research in Technology, vol.3, issue 1, Aug. 2012.

6. Panos E. Kourouthanassis and George M. Giaglis, "Shopping in the 21st Century: Embedding Technology in the Retail Arena", Consumer Driven Electronic Transformation, Springer Berlin Heidelberg, pp.227-239, 2005.

7. http://www.rfidjournal.com

8. http://en.wikipedia.org/wiki/zigbee

9. Ankit Anil Aggarwal, "RFID Based Automatic Shopping Cart", The International Institute for Science, Technology and Education journal on Control Theory and Informatics ,vol.1, no.1, 2011

Sub aperture polishing of Fused Silica asphere for deterministic control of form and texture

Neeraj Pandey, Anil Kumar, K. K. Pant, A. Ghosh
Instruments Research & Development Establishment,
Dehradun, India-248008
neerajpandey@irde.drdo.in, neerajspn@gmail.com

Abstract— **Aspheric lenses are the lenses, which have varying radius of curvature according to distance from the optical axis. Optical designer can do excellent aberration correction using an aspheric lens, which provides superior resolution, even with compact optics composed of a small number of elements. We report fabrication of an aspheric lens in Fused Silica using sub aperture polishing technique as traditional full aperture polishing is not suitable for aspheric lenses. The linear feed rate has been optimized to produce optical quality surface finish using less number of iterations. Stylus profilometer and optical profilometer has been used for aspheric surface characterization.**

Keywords— *Aspheric Optics, Sub aperture polishing, Optical fabrication.*

I. INTRODUCTION

A lens is an important part of any optical system. These lenses may have spherical, aspheric or diffractive surface. As per the shape of the lens, fabrication methods are different. A spherical surface is easy to fabricate using conventional grinding and polishing machines [1]. Also, the spherical surfaces are easy to measure using a Newton interferometer setup [2]. The fabrication methods and measurement systems for aspheric and diffractive optics are quite difficult and challenging.

Spherical surfaces are not usually the optimal shape for lens surfaces or for mirrors for most optical applications. Optical systems can benefit tremendously, if they can use aspherical surfaces – surfaces that are not spherical. The use of aspheres allows better quality images with the use of fewer elements. The application of aspheric surfaces is limited to a tiny fraction of optics because of the difficulty in fabricating and testing these surfaces. Optical designers always require less number of surfaces with more degree of freedom for removing the aberrations. Using aspheric surfaces, optical designer can design an optical system with less number of elements, small optical system and improved performance [3]. Spherical surface has only one radius of curvature. It is easy to fabricate using classical grinding & polishing techniques.

Aspheric surface has variation in radius of curvature along different zone.
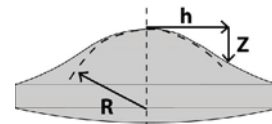
Figure1. Aspheric Surface

The sag equation of an aspheric surface is as following:

$$z = \frac{ch^2}{1 + \sqrt{1 - (1+k)c^2 h^2}} + Ah^4 + Bh^6 + Ch^8 + Dh^{10} + \ldots$$

…. (1)

Where, c is the curvature = (1/R), k denotes the conic constant & A, B, C, D are 4th, 6th, 8th and 10th order deformation coefficients respectively [4].

In this paper, we present the polishing of Fused Silica aspheric surface using sub aperture polishing technique. Aspheric optics in Fused Silica material having base radius of curvature 73.117 mm and diameter 12 mm was required for a Laser altitude sensor. Conventional all spherical design requires 3 lenses, while Aspheric design requires only single aspheric lens. Lenses were polished using sub aperture polishing method. Surface measurements were done using stylus profilometer and optical profilometer.

The component details are as following:

Material – Fused Silica
Final edge diameter = 12.000mm
Spherical radius R1 = 10.711mm Convex
Aspheric base radius R2 = 73.117mm Convex

Conic constant k =
0 Aspheric terms:
A = 0.103578e-03, B = -0.213284e-06
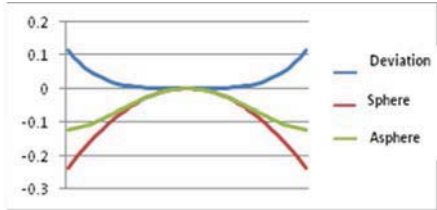
Figure 2.Sag Profile of Fused Silica asphere

Figure 2 shows the sag profile analysis. The red, green and blue curves show the sphere sag, asphere sag and the departure of asphere from base sphere respectively. The maximum departure at the edge is 50 m. The sag analysis shows that the surface is convex at the center while it is being concave at the edges. The curvature is changing form center to edge and there is inflection point. This behavior of asphere creates problem in polishing as well as in testing of surface.

II.   SUB APERTURE POLISHING TECHNIQUE

Full aperture technique is best suited for spherical optics, while an aspheric surface has zonal departures in various zones. A full aperture polishing tool cannot correct aspheric surface therefore using a smaller sub aperture tool, we will get finer corrections over the various zones [5]. The main difference between full aperture polishing and sub aperture polishing is that only a small section of the aperture is in contact with the polishing tool in sub aperture polishing.

Classical full aperture polishing method uses pitch or polyurethane pad for polisher. We cannot vary the polishing spot in full aperture polishing. The spot size of a membrane based sub aperture tool can be controlled by the application of pressure.

In sub aperture polishing, the tool and polishing medium selection is driven by the localized radius of asphere as well as the material properties. We used polyurethane (LP66) and Uninap cloth for various polishing cycles [6].
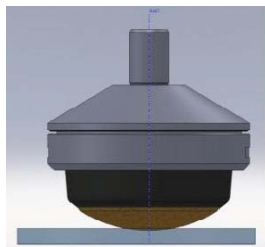
Figure 3. (a) Sub aperture tool   (b) Sub aperture tool geometry
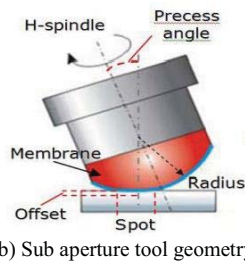
constant (c_p) describes molecular level effects during the

Figure 4. (a) Mounting tool   (b) Polishing tool

Sub aperture tool geometry is shown in figure 3(b). We have developed a mounting tool in stainless steel material for easy mounting of aspheric lens and to remove centering error problem due to mounting. A sub aperture polishing tool is shown in figure 4(b).

III. GRINDING OF ASPHERICS SURFACE

First, both the surfaces were grinded flat and edging of the part was done up to 14 mm diameter. Aspheric surface was generated using diamond cup tools having different grit sizes- D46, D17, D6. For aspheric surface, first a best fit radius was generated to reduce the excess material removal. In the figure 5 yellow, green and red curve show asphere sag, best fit sphere and the deviation of best fit sphere respectively
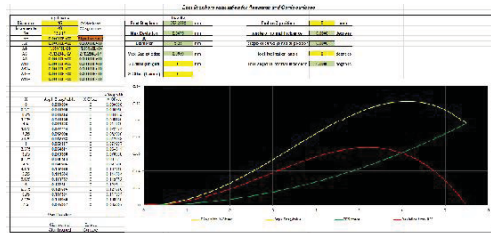
Figure 5. Best fit radius calculation

Figure 6. (a) Cup tool grinding   (b) Grinded surface profile –Peak to Valley (PV) 1.5 m
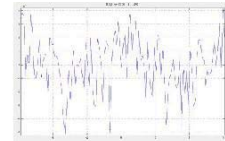
IV.   POLISHING, MEASUREMENT & SUCCESSIVE ITERATIONS

Material removal rate during the optical polishing can be defined by the Preston's equation [7] and it depends up on the tool pressure and relative velocity between tool and the lens surface.

$$\frac{dm}{dt} \, c \, P \, V \qquad \text{…………….. (2)}$$

where dm/dt is the average thickness removal rate, P_0 is the applied pressure, and V_r is the average relative velocity of the polishing particle relative to the substrate. The Preston's polishing process. The rate of removal increases linearly with

pressure and velocity. By changing the relative velocity between polishing tool and substrate, one can achieve desired material removal at the substrate. In our method of sub aperture polishing, we have described material removal in terms of variable linear feed rate over the part and dwell time approach has been applied for material removal [8].

We have used raster polishing mode for polishing of Fused Silica aspheric surface for local corrections. In raster polishing mode, job axis (C-Axis) is stationary while tool is moving either along X-axis or Y-axis. During raster polishing, feed rate is variable as per the error profile of the surface. Hence material removal rate is different in different regions of surface and we get desired material removal at surface along different regions.

First, we have done polishing trials on a Fused Silica flat surface having diameter 25 mm. The flat surface has been polished using different feed rates in seven polishing iterations. The roughness of the flat surface has been measured after each polishing cycle. It was observed that a lower value of feed rate gives better polishing quality.
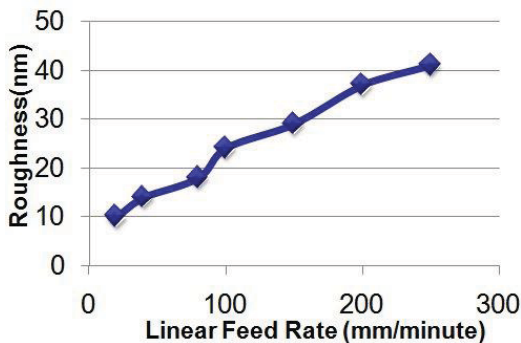
Figure 7. Polishing quality and linear feed rate

The polishing time at different feed rates is also monitored. The lower feed rate polishing cycle takes much time. So there is a trade of between polishing quality and polishing time. As per the required surface accuracy, the linear feed rate and polishing time has been optimized for the polishing for fused silica asphere.
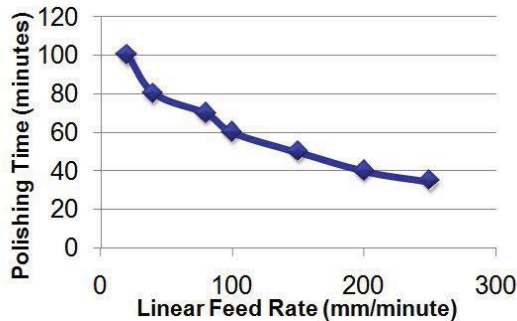
Figure 8. Polishing time and linear feed rate

Polyurethane pad is used for pre-polishing due to fast cutting action. The polishing tool is dressed after two polishing runs and Uninap cloth has been used in final polishing runs for surface roughness improvements. The polishing medium depends upon the material to be polished. For optical glasses, Cerium Oxide is the choice of material as polishing medium [9]. Cerium Oxide having particle size 1 micron with de-ionized water is used in polishing slurry. The slurry density was maintained 1.3 gm/cm3 and room temperature was maintained at 24 ^{0}C.

Raster mode has been chosen over the sync-spiral polishing mode because grinded surface is very good and surface peak to valley (PV) is of the order of 1.5 m. Surface profile measurements were done using Form Talysurf contact profilometer. Linear feed rate has been optimized as per the surface profile measurements and required corrections. Feed rate values between 20 mm/minute to 80 mm/minute provide good surface finish. Feed rate values more than 80 mm/minute degrade the surface while feed rate values less than 20 mm/minute takes longer polishing time. The feed rate is moderated as per the required material removal at a particular place.

Figures 9 to 13 show the feed rate profiles and surface profiles in various polishing cycles. After first polishing cycle, the measured surface profile is shown in figure 10(a). In this surface profile, more material has been removed at the central part as compared to material removed at the outer zonal part. In next polishing cycle, feed rate (figure 10b) is moderated such that high feed rate is at central part while lower feed rate at the outer zonal part. Hence material removal rate is small at the central part while it is more at the outer zonal part. Using this approach to moderate linear feed rate, the surface peak to valley (PV) was reduced in successive polishing iterations.
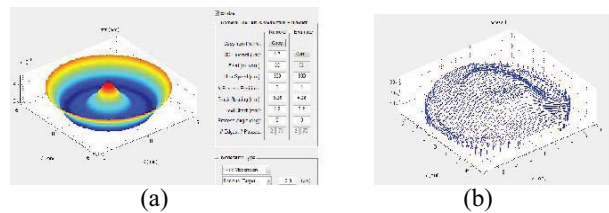
(a)   (b)
Figure 9. (a) Initial Surface profile (PV-1.5 m) after grinding (b) Feed rate in Ist polishing cycle
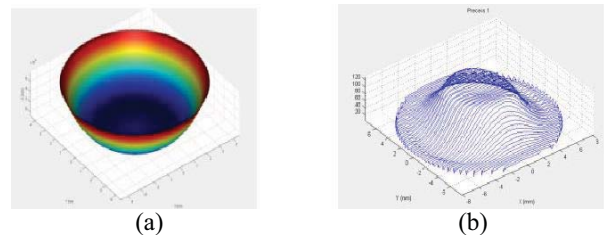
(a)   (b)
Figure 10. (a) Surface profile (PV-1.3 m) after Ist polishing cycle (b) Feed rate in IInd polishing cycle
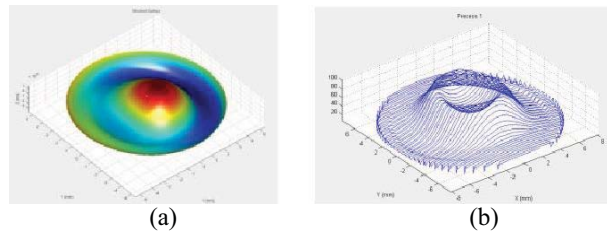
Figure 11. (a) Surface profile (PV-1 m) after IInd polishing cycle
(b) Feed rate in IIIrd polishing cycle
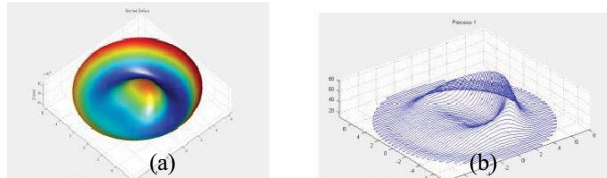
Figure 12. (a) Surface profile (PV-0.8 m) after IIIrd polishing cycle
(b) Feed rate in IVth polishing cycle
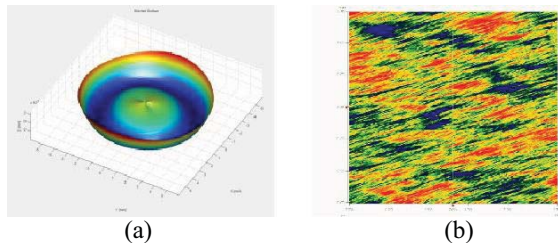
Figure 13. (a) Surface profile (PV-0.4 m) after IVth polishing cycle
(b) Surface roughness 10 nm after IVth polishing cycle

Among four polishing runs, first two runs are raster with polyurethane LP 66 pad having tool radius 14 mm, while other two raster runs with Uninap cloth having tool radius 7 mm. In four consecutive polishing iterations, we achieve successive improvements on surface and finally we achieved surface peak to valley (PV) 0.4 m and roughness (Ra): 10 nm.
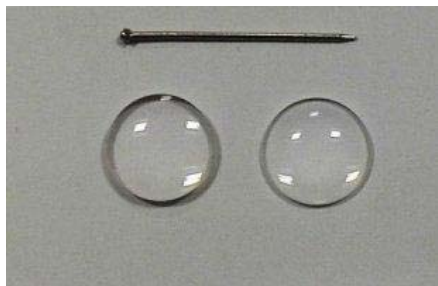
Figure 14. Polished Aspheric Lenses

V. CONCLUSION

Convex aspheric surface in fused silica material has been polished successfully using sub aperture polishing technique. The linear feed rate has been optimized for better results and surface accuracy. We have done four polishing runs having total polishing time 147 minutes. The finished surface has peak to valley (PV): 0.4 m, RMS: 40 nm and roughness (Ra): 10 nm.

Sub aperture polishing is a powerful tool that can be used to finish aspheres without the need for artisan techniques or skilled operators. Sub aperture polishing technique has enabled aspheres to be produced in a cost effective and deterministic manner with significantly reduced set up times, when compared with the traditional polishing techniques.

ACKNOWLEDGEMENT

REFERENCES

[1] Geoffrey Boothroyd, [Handbook of Lapping and Polishing], CRC Press, Taylor & Francis Group, New York 2007.

[2] M. V. Mantravadi, Newton, Fizeau, and Haidinger Interferometers, [Optical Shop Testing], Third Edition, John Wiley & Sons, Inc., New Jearsy 2007.

[3] B. Braunecker, R. Hentschel, and H.J. Tiziani, [Advanced Optics Using Aspherical Elements], SPIE ebook, 2008.

[4] J. Kumler, "Designing and Specifying Aspheres for Manufacturability", Jenoptik Optical Systems, Inc.

[5] Neeraj Pandey, "Pitch polishing of semiconductor optical materials using continuous iterative interferrogram analysis" [Physics of Semiconductor Devices], Proc. IWPSD-2013, 10-13, Dec 2013, India, Springer International Publishing, 2014, pp 811-812.

[6] Marc Tricard, "Subaperture approaches for asphere polishing and metrology", Proc. SPIE 5638, Optical Design and Testing II, 284 (April 06, 2005).

[7] F. W. Preston, "The Theory and Design of Plate Glass Polishing Machines" J. Soc. Glass Tech. 11, 214, 1927.

[8] R G Bingham, "A Novel Automated Process for Aspheric Surfaces", Proc. SPIE 45th Annual Meeting, 2000, Vol. 4093 'Current Developments in Lens Optical Design and Engineering'; pp445-448.

[9] L. M. Cook, "Chemical processes in glass polishing" Journal of Non-Crystalline Solids Volume 120, Issues 1–3, 1 April 1990, Pages 152–171.

DESIGN AND SIMULATION OF NOVEL TWO-STAGE OPERATIONAL TRANSCONDUCTANCE AMPLIFIER A USING FINFET

Prateek Tiwari
Research Scholar
ECE Department
ITM University, Gwalior (MP)
Prateekt6849@gmail.com

Ranjeet Singh Tomar
Professor
Department of Electronics and
Communication, ITM University,
Gwalior (M.P.)

Shyam Akashe
Professor
Department
Electronics and Communication
ITM University, Gwalior (M.P.)
shayam.akashe@itmuniversity.ac.in

Abstract—**In this paper novel two- stage operational transconductance amplifier (OTA) is designed using FinFET techniques & the responses are simulated. Basically design of OTA is totally based on MOS transistors that are essentially non linear which leads to deterioration The proposed circuit of two-stage OTA is used for low power consumption, increasing transconductance and efficiency of the circuit. Due to the operation of all the transistors in saturation region the output voltage is increased. By using proposed circuit the performance of two stages OTA is enhanced. Performance parameters for the designed circuit are as power consumption 38.13μW, gain margin 57.9dB, phase margin 104.31º, slew rate 30.76Vμ/sec etc. By introducing FinFET techniques the required power supply for the circuit decreases to 0.7V. Model parameters are calculated by using cadence virtuoso 6.1 in 45nm technology.**

Keywords: FinFET, CMOS Operational transconductance Amplifier (OTA), low power

I. INTRODUCTION

The Operational Tranconductance Amplifier (OTA) operates in differential input voltage and generates output current. OTA is an unbuffered op-amp and it produces high output resistance. Application for OTA includes voltage controlled low-pass or high-pass filters, waveform generators, amplifiers, modulators, comparators, and Schmitt triggers. OTA was designed in low power and frequency for the reduction in Transconductance in the circuit. Better noise optimization with good settling time is acquired using three-stage OTA design [1]. With different applications of OTA various techniques are being applied like single ended and rail to rail topology and performance

parameter of the circuit is observed according to it [2]. Using feedback in the OTA design circuit better performance can be attained in the field of efficiency, Transconductance and output resistance of the circuit [3]. Higher gain-bandwidth product with lower supply voltage can be acquired using folded cascade topology and by removing the transmission gate from the circuit [4]. Slew Rate and leakage controlling can be obtained using Adaptive biasing technique in OTA [5]. Controlling of Leakage reduction and better performance in current analysis can be obtained by using FinFET design [6]. High frequency and low power approach in OTA is used for higher tuning property and low current consumption in the circuit [7]. Higher gain and better transconductance can be obtained by designing OTA in 45 nm technology [8].

Better dimensionality and improved input offset voltage can be obtained using the Bulk degeneration technique [9]. OTA designed using two diode connected transistor in class AB amplifier led to achieve wide linear input range with high output performance at low supply voltage [10]. Designing of OTA at low power, low voltage and wide linear range in bulk-driven technique is shown as another method for designing of the circuit [11]. OTA circuit is simulated for high gain, high CMRR and low power consumption at low supply voltage and the performance of the circuit is observed [12]. Different values of Transconductance can be obtained with the variations in aspect ratio of transistor [13].

In this work, the advantages of the c Two stage OTA are considered to be carried out for a FinFET based two stage OTA circuit. The design is implemented with 45nm two stages OTA FinFET Technology and tested in Cadence virtuoso 6.1. The paper is summarized as follows, first is the introduction and working of operational transconductance

amplifier, then is the proposed circuit with performance parameter and comparison of proposed Two stage FinFET based OTA circuit with Two stage OTA circuit and simulation and result is compared by showing graph below.

II. OPERATIONAL TRANSCONDUCTANCE AMPLIFIER (OTA)

OTA is an electronic equipment is also process during which distinction of the two voltages because the input and current because the output. OTA may be a voltage controlled-current supply (VCCS). Since, voltage controlled-current supply is alleged that the output current (Io) is controlled by the input voltage (V1), the output current depends on the input voltage. The extra bias current (IB) is additional to controlled Transconductance. The operational transconductance amplifiers find wide application in the analog integrated circuit design. Because of high input impedance of the MOS devices the order for low-output impedance is not actual for the amplifiers which are inside integrated circuit. In this case only capacitive load presents at the output and accordingly high-impedance output stage with high voltage gain is suitable to use. The ideal model of OTA and equivalent circuit design is shown in fig. 1 and fig. 2 respectively.
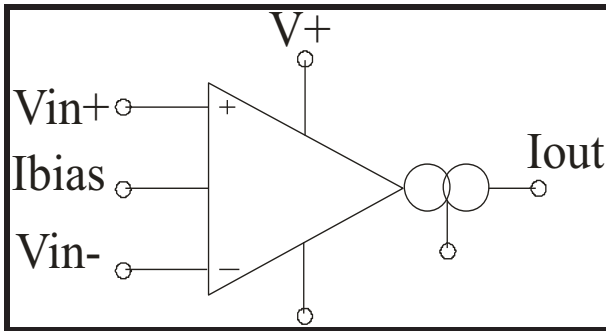
Fig 1: Symbol of OTA
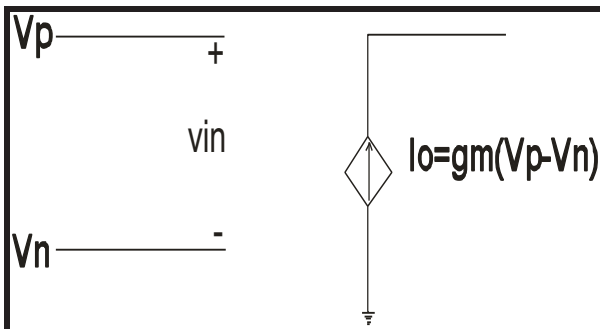
Fig 2: Equivalent circuit of OTA

 Since the output of an OTA is current, the output impedance of the OTA is very high (ideally infinity). Since gm of the OTA is dependent on the *Ibis* current, the output

of the OTA is controlled externally by the bias current (*Ibis*).

III.   DESIGN PRINCIPLES

A.   CONVENTIONAL 2-STAGE OTA
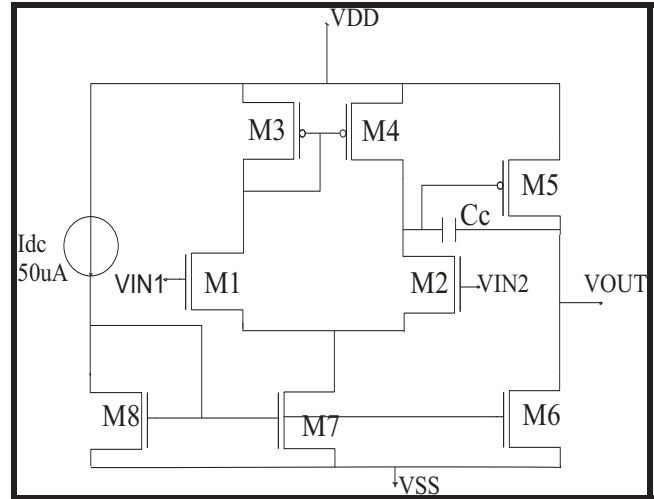
Fig.3. Conventional diagram of 2-Stage OTA

In VLSI technology the dimensions of CMOS decreases and power supply also reduces and speed of device is increase. So the OTA may be a basic building block in most of analog circuit with linear input-output characteristics also OTA is widely employed in analog circuit include such as Instrumentation amplifier with ADC and Filter circuit. The OTA is same as operational Amplifier in which having differential inputs.
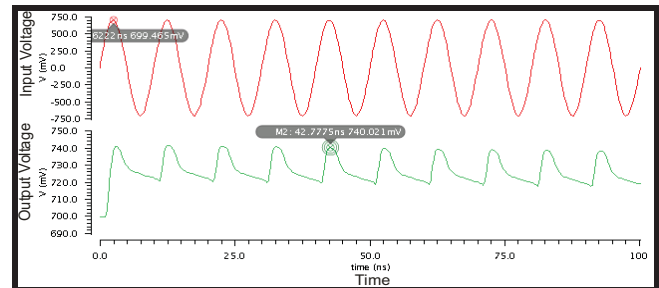
Fig.4. Output of Conventional 2-Stage OTA

R = r6 /r7   (1)

Where,

R=output resistance

r6 and r7= internal resistance

The ideal transfer characteristics are as follow:-

Mathematically expression,

$$Iout = gm\,(Vin+\; -\; Vin-) \qquad (2)$$
$$Iout = gm * Vin \qquad (3)$$

Where,

Gm = Transconductance,

IC = control current,

Vin+ = Non inverting

Vin- = Inverting

Vin is input voltages.

B. PROPOSED CIRCUIT OF 2-STAGE OTA
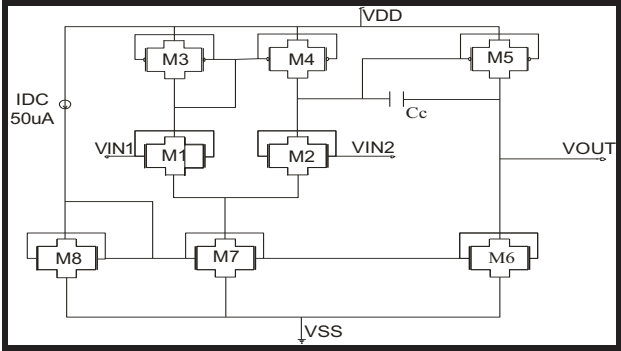
Fig.5.Proposed diagram of Two-stage OTA by FinFET Technique

FinFET is stand for 'fin-Shaped Field Effect Transistor' which describes a non planar, double transister built on an SOI substrate, based on single gate transistor design. The important characteristics of FinFET is that conducting channel is wrapped by a thin si 'fin', which forms of the body of a device. The thickness of the fin determines the effective channel length of the devices. In terms of its structure, it typically has a vertical fin on a substrate which runs between a larger drain and source area. This protrudes vertically above the substrate as a fin. The gate orientation is at right angles to the vertical fin. And to traverse from one side of the fin to the other it wraps over the fin, enabling it to interface with three side of the fin or channel. This form of gate structure provides improved electrical control over the channel conduction and it helps reduce leakage current levels and overcomes some other short-channel effects.The term FinFET is used somewhat generically. Sometimes it is used to describe any fin-based, multigate transistor architecture regardless of number of gates. Since, a design of a proposed OTA with 45nm FinFET technology is proposed and shown in fig. 5 above.

WORKING:

The two stage OTA architecture consists of two stages. Its configuration is similar to the considered operational voltage amplifier Op Amp. The first stage is a differential amplifier (M1, M2, M7) with current mirror load (M3, M4). It ensures high value of the CMRR. The second stage is a common source amplifier with active load (M5, M6). Transistor M8 is for the biasing of M8-M7 and M8-M6 current mirrors. Iref is a constant current reference. As we

know from previous modules, transistors M1 and M2, and M3 and M4 are identical. Also the Miller capacitance Cc is introduced, in order to guarantee the stability of the circuit.
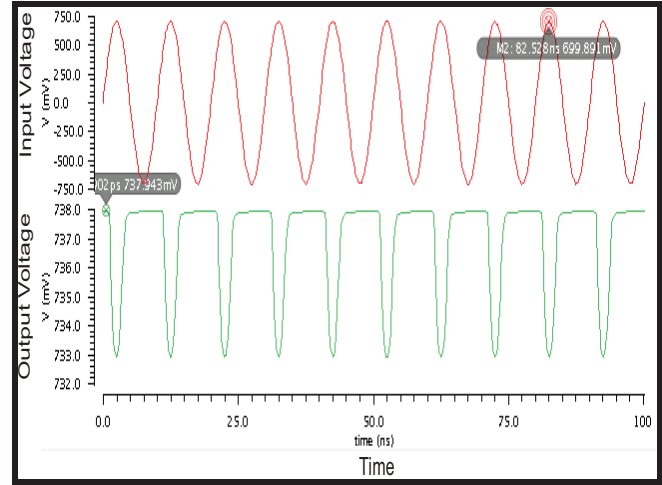
Fig.6. Output of Proposed 2-Stage OTA

IV.   OTA PRACTICAL CONSIDERATION

(A).Noise

Noise may be define that random fluctuation in all electrical and electronic circuits Or in alternative, word noise is unwanted signal that arises by environment like natural and man-made artificial sources like vehicle and a few electronic equipment.

$$Sv(f) = 4kTR, \qquad f \geq 0 \qquad (1)$$

Where,

k= Boltzmann constant

R= noiseless resistor

T= temperature

(B).Voltage Gain

Voltage may be defined, in which circuit of the gain is improving in the power factor of output to input. Quantitative relation of voltage measured at the output to voltage measured at the input. Calculation of the voltage gain is observed in logarithmic scale in decibel.

$$A_u = \frac{v_{out}}{v_{id}} = \frac{i_o r_{out}}{v_{id}} = \frac{i_o}{v_{id}} r_{out} = G_m r_{out} = \frac{g_{m5} \cdot g_{m2}}{(g_{o5}+g_{o6})(g_{o2}+g_{o4})} \cdot \qquad (2)$$

35

$$Voltage\ Gain = 10\log\left(\frac{Vout}{Vin}\right) dB \qquad (3)$$

$Vout$= Output Voltage.

Vin = Input Voltage.

(C).Phase Margin

Phase margin is nothing but, in electronic equipment the difference between the phases is calculated in degree and 180º also and amplified output signal is a function of frequency. One's the loop gain is 1.0 the phase margin is the difference between response of phase or -180º.Phase margin is also said that the negative phase perturbation by which system is marginally stable.

$$P.M. = 180º + \measuredangle\ G(jWgc) \qquad (4)$$

Where,
gc = gain crossover frequency

(D).Slew Rate

The rate of change of the closed-loop amplifier output voltage for a signal input. The pulse is faster at slew rate is low. Since, pulse can change its state for higher output performance the slew rate is mostly determined by the utmost current obtainable to charge or discharge capacitance. It unit is v/μs.
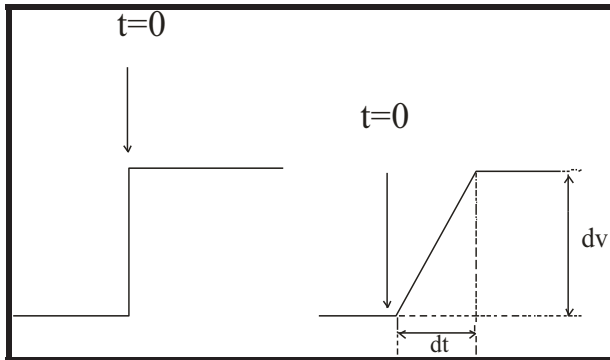
$$Slew\ Rate = \frac{\Delta Vout}{\Delta t} \qquad (5)$$

Where
$\Delta Vout$ = Voltage at Output
Δt = time

(E).Power Consumption

To achieving power consumption dimension is vital in all CMOS based circuits In CMOS based circuit short channel effect is arise, to overcome this effect we used FinFET techniques. In some other, word what proportion power is consumed by the circuit by which we have tendency to get desired output. Power consumption is measured in kilowatt hours (kWh).

$$Power\ (P) = (Vdd) * (Iavg) \qquad (6)$$
Where,
Vdd = supply voltage
Iavg = average current.

(F). Gain Margin

The reciprocal of the open-loop voltage amplification at the lowest frequency at which the open-loop phase shift is such that the output is in phase with the inverting input the gain margin is nothing however within which the problem by that the gain |G(jw)| has got to be magnified for operational transconductance amplifier. The expression of gain margin is in dB. The gain margin defines as follow:

$$GM = |G(j\omega 180°)| - 1 \qquad (7)$$

$$GM = -1/G(jWpc) \qquad (8)$$
Where,
ω180∘ is such that G(jω180∘) = 180∘.
pc = phase crossover frequency

(G). Efficiency

Efficiency of a circuit is that the ability of providing the higher output power once any input is provided within the circuit. It's the foremost vital parameter within the analog circuit. It is defined as the ratio of the output power obtained from the circuit to the input power provided to the circuit. It's calculated in proportion (%).

$$\eta = \frac{Pout}{Pin} \qquad (9)$$

Where,

Pout = Output power is measured.

Pin= Input power is measured.

(H).Transconductance

The circuit performance is ascertained by measuring Transconductance. The circuit is good as much as transconductance is more. It is defined as the ratio of the change in output current to the change in input voltage terminal. It is denoted by gm.

$$gm = \left(\frac{\Delta Iout}{\Delta Vin}\right) \qquad (10)$$

Where,

ΔIout = Current at output terminal

ΔVin = Voltage at input terminal

(I). *Gain-Bandwidth product*

The frequency, at which the gain starts decreasing is called the bandwidth **BW** or the **−3dB** frequency. The product of the low-frequency gain and the bandwidth is called the Gain-Bandwidth product **GBW**. Its value is much closed to unity gain frequency **fu** - the frequency, at which the gain is equal to 1 (0dB).

$$GBW = \frac{g_{m1}}{2\pi C_c}; \quad SR = \frac{I}{C_c}, \text{ where } I = \min(I_{D5}, I_{D7}). \quad \textbf{(11)}$$

V. SIMULATION AND RESULTS

A. SIMULATION

1. During this FinFET technique that we tend to employed in this paper we've got seen a reduce in noise and therefore the noise curve as shown in fig. 6.
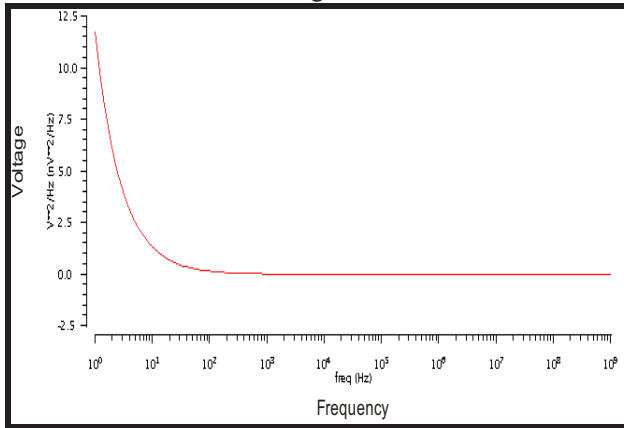
Fig.7. Noise

2. During this paper we seen a reduction in power consumption by using FinFET technique, it is best for circuits as shown in fig. 7
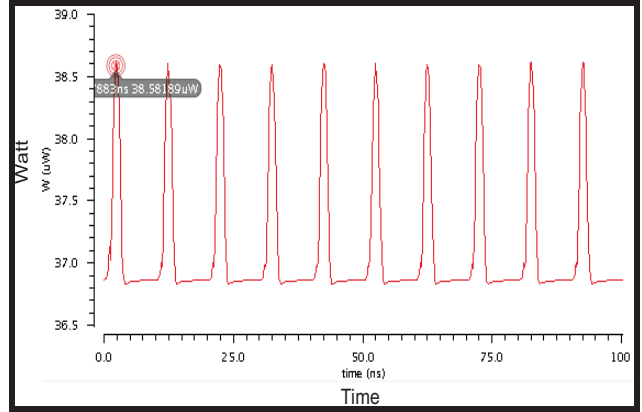
Fig.8. Power Consumption

3. Phase Margin and Gain Margin of 2-stage OTA
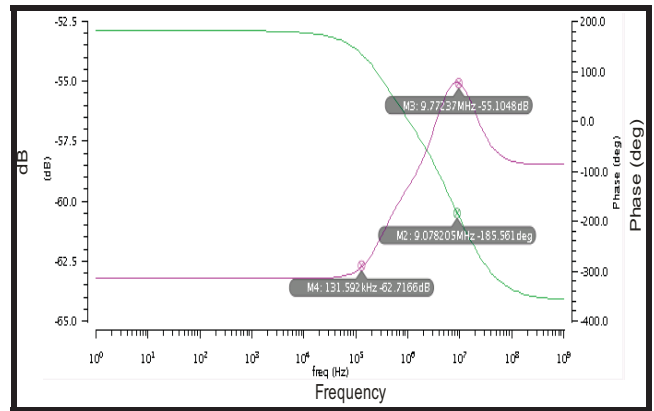
Fig.9. Phase Margin and Gain Margin

B. RESULTS

Table 1: Comparison table for Two-Stage OTA and FinFET based Two-Stage OTA

Sl. No	Parameters	Two-Stage OTA	FinFET based Two-Stage OTA
1	Noise(V2/Hz)	3.56954E-14	2.45732E-17
2	Power Consumption (μW)	41.99	38.13
3	Supply voltage(V)	0.7	0.7
4	Slew Rate	32.47	30.76
5	Leakage Power	45.45E-9	39.22E-12
6	Phase margin	100.21º	104.31º
7	Gain	57.4	59.47

	margin(dB)		
8	Open loop gain(dB)	61.41	63.21
9	Transconductance	1.5779E-6	2.221E-4
10	Voltage Gain	30.7dB	31dB

Tabular representation of the compared data is given above table.1. From the above mentioned data the graphical comparison is done. As we can see that all the parameters calculated have decreased and performance of the device is enhanced by using the proposed novel FinFET technique in place of CMOS.

Phase Margin

Slew Rate

Gain Margin

Open Loop Gain

Transconductance

	Transconductance
2-Stage OTA	1.5779
FinFET based 2-stage OTA	222.1
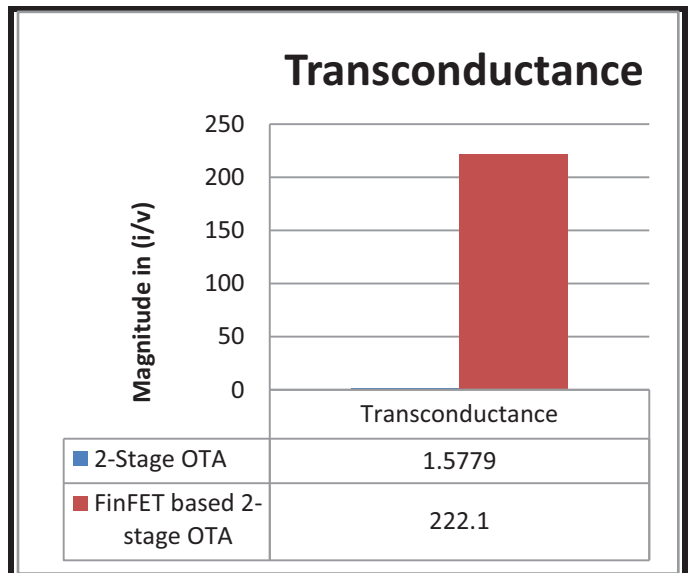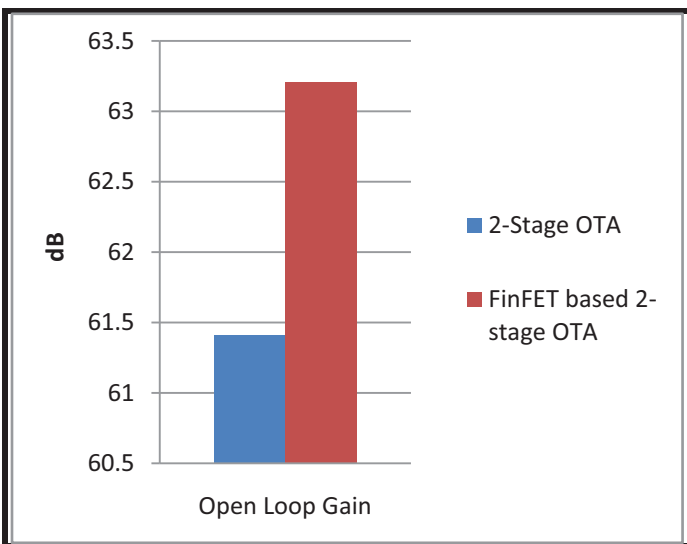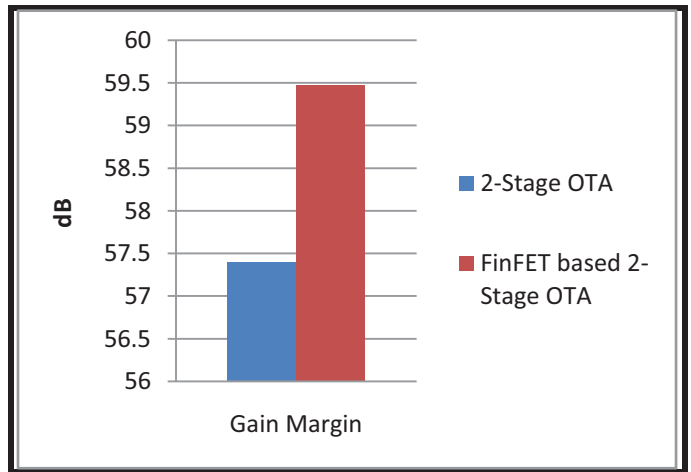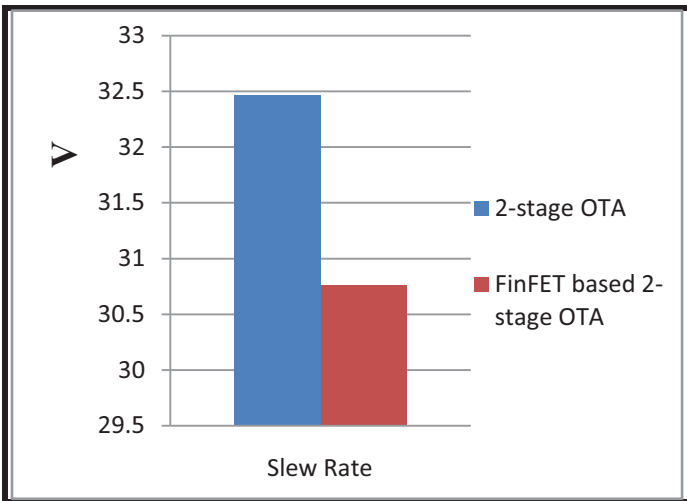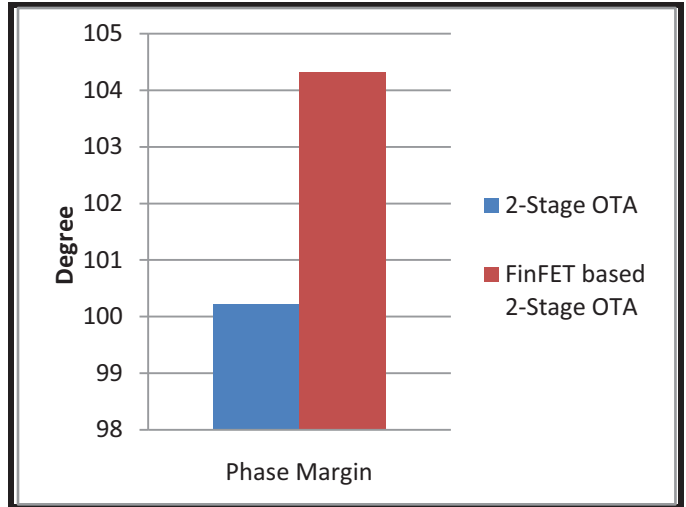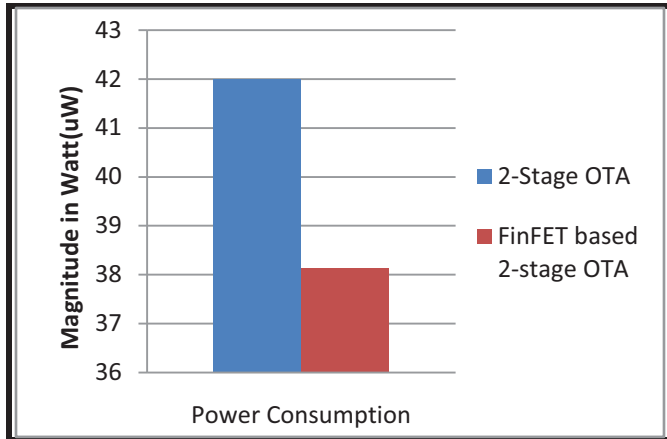
VI. CONCULSION

In this, paper Two stage OTA is optimized and result is simulated in 45nm technology. By exploitation, FinFET in place of two-stage OTA there is reduction in the gain margin59.47dB, phase margin104.31º, power consumption38.13mW and slew rate 38.13 V/µs etc. By exploitation FinFET technique power consumption is obtained is 41.99 mW from 38.13 mW. In my simulation result power dissipation, phase margin, gain margin, voltage gain employed good result.

ACKNOWLEDGEMENT

REFERENCES

[1] Siddharth Seth and Boris Murmann ., "Settling Time and Noise Optimization of a Three-Stage Operational Transconductance Amplifier" IEEE transactions on circuits and systems, vol. 60, no. 5, May 2013

[2] M. F. Li, Uday Dasgupta, X. W. Zhang, and Yong Ching Lim," A Low-Voltage CMOS OTA with Rail-to-Rail Differential Input Range", IEEE Transactions on circuits and systems, Vol. 47, pp. 1, January 2000

[3] Shanshan Dai, Xiaofei Cao, Ting Yi, Allyn E. Hubbard, and Zhiliang Hong," 1-V Low-Power Programmable Rail-to-Rail Operational Amplifier With Improved Transconductance Feedback Technique",IEEE Transactions on very large scale integration (vlsi) systems, Vol. 21,pp. 1928-1935, September 2013

[4]. Fabian Henrici, Joachim Becker, Maurits Ortmanns, Yiannos Manoli," A Switchable Folded-Cascode OTA without Transmission Gates in the Signal Path", IEEE Conference, pp.180-183, November 2008.

[5]. Fabian Henrici, Joachim Becker, Maurits Ortmanns, Yiannos Manoli," A Switchable Folded-Cascode OTA without Transmission Gates in the Signal Path", IEEE Conference, pp.180-183, November 2008.

[6]. Zehan Kesilmiş, Mutlu Avc, Murat Aksoy3," An operational Transconductance amplifier with 45nm finfet technology ", 2011

[7]. Dmitry V. Morozov and Alexander S. Korotkov, "Transconductance Amplifier With Low-Power Consumption", IEEE Transactions on circuits and systems, Vol.52, pp. 11, November 2005

[8]. Navneet Dubey and Shyam Akashe"Low Power Two-Stage Operational Amplifier design using 45 nm Technology", International Journal of Modern Engineering & Management Research(IJMEMR) , Vol.2, pp. 15-20, December 2014

[9]. Joel Gak, Matías R. Miguez, and Alfredo Arnaud, "Nanopower OTAs with Improved Linearity and Low Input Offset Using Bulk Degeneration" IEEE Transactions on circuits and systems, Vol. 61, pp. 03, March 2014

[10] A. Yodtean, "A CMOS OTA and Implementation," IEEE International Symposium on Intelligent Signal Processing Communication Systems (ISPACS) , pp. 1-4, 2014

[12] S. Goswami, "Analysis and Design of Two-Stage Operational Transconductance Amplifier," vol. 2, no. 4, pp. 9–14, 2014

[13] Abhay Pratap Singh, Sunil Kr. Pandey, Manish Kumar," Operational Transconductance Amplifier for Low Frequency Application" International Journal of Computer Technology and Applications (IJCTA), Vol. 3, pp. 1064 -1066, May-June 2012

Polarization Selective Photonic Crystal Based Integrated Plasmonic Sensor

Rik Chattopadhyay, Tushar Biswas, Shyamal K. Bhadra

CSIR-Central Glass and Ceramic Research Institute

196, Raja S.C. Mullick Road, Kolkata-700032

Abstract— **We report a two dimensional photonic crystal based integrated plasmonic sensor which selects only transverse magnetic polarization from an unpolarized light input. The device is polarization sensitive over a large band of wavelength, 590nm to 833nm. The device is extremely compact, can be realized through batch fabrication (mass) and effective for designing on chip plasmonic sensors. The polarization selection improves the signal to noise ratio of the output signal and thus provides more detection sensitivity.**

Keywords— photonic crystal, Integrated plasmonic sensor.

I. INTRODUCTION

Integrated plasmonic sensors are extremely small in size, normally fabricated on planar waveguide structure and provide almost equal sensitivity like the standard Krestchmann type plasmonic sensors, which are large in size and employs bulk optics. Integrated sensors allow sensing in multiple channels simultaneously, requires minimum amount of energy for operation and their integrated design gives structural robustness. The main problem of any plasmonic sensors is that only the transverse magnetic (TM) modes excite surface plasmon. Since the modal cutoff width of the guiding layer is larger for TM mode than transverse electric (TE) mode, so it is not possible in integrated waveguide sensor to eliminate the fundamental TE mode without cutting off the fundamental TM mode. So the input light should be polarized in order to get better signal to noise ratio (SNR). Bulk plasmon sensor employs external polarizer to obtain TM polarized light which is not a good option for designing integrated sensors. Therefore a waveguide (WG) based polarizer is required for integrated sensors. The palsmonic biosensor should be sensitive around refractive index (RI) 1.33 and operable in the wavelength region 600nm to 900nm [1]. So far all reported waveguide based TM polarizers works on a wavelength region close to 1.55 μm, which is far from the requirement. We first report a two dimensional photonic crystal (PC) waveguide which allows only the TM mode in the wavelength range 590nm to 833nm.

The PC is analyzed analytically using the plane wave expansion method (PWM) [2] and wave propagation through integrated sensor structure is done with the help of Finite Difference Time Domain (FDTD) method using Lumerical FDTD software and an estimation of the detection signal is made to predict the performance of the device. We compared the sensitivity of the proposed sensor with other reported experimental integrated sensors employing output power measurement principle.

II. DESIGN OF INTEGRATED SENSOR

A. Design of photonic crystal

Photonic crystal structure is an array of a high dielectric permittivity material on a low permittivity material or vice versa. The structure allows some optical frequency signal to pass through it and some frequencies are forbidden in the structure. The electromagnetic wave equation in a PC can be written as [2]

$$\nabla \times \left[\nabla \times E(x|\omega) \right] = \frac{\omega^2}{c^2} \varepsilon(x_\parallel) E(x|\omega) \tag{1}$$

$$\nabla \times \left[\nabla \times H(x|\omega) \right] = \frac{\omega^2}{c^2} \varepsilon(x_\parallel) H(x|\omega) \tag{2}$$

where $E(x|\omega)$ and $H(x|\omega)$ are the electric and the magnetic field of the photon, ω is the angular frequency, c is the velocity of light and $\varepsilon(x_\parallel)$ is the dielectric function describing the PC. The eigenvalue equation (1) and (2) are solved for ω. Only the real values of ω are the acceptable solution. The electromagnetic (EM) wave having these frequencies can pass through the structure. The complex valued solutions form the photonic band gap (PBG) and are forbidden to pass through the PC. Therefore one can generate a plot between normalized frequency $\omega a/2\pi c$, where a is the lattice constant, and wave-vector k ($2\pi/\lambda$, where λ represents operating wavelength). The

components of k in the plane of the crystal is called in-plane wave vector and the component perpendicular to the plane is called out-of-plane wave-vector. So two sets of PBG can be generated, namely in-plane PBG where normalized frequency is plotted as a function of in-plane k and the other is off-plane where normalized frequency is plotted against the out-of-plane k. When a defect is introduced in the crystal then all EM waves having forbidden frequencies are confined within the defect. It is evident from Equation (1) and (2) that the band structure depends on ε $(x_{\parallel})$ i.e. the permittivity of the materials used, lattice constants (for the proposed structure it is the distance between the centers of the silicon rods) and the dimension of the lattice sites (in the present case rod diameter). The schematic diagram of the PC structure is shown in Fig. 1.
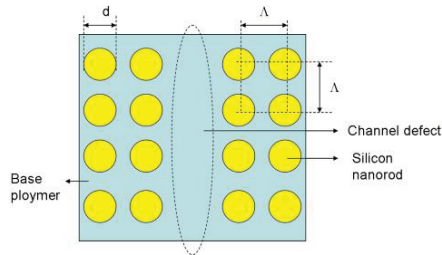
Fig. 1. Schematic diagram of the plan view of the photonic crystal. Light propagates along the direction of the channel.

The proposed structure is a two dimensional square lattice PC designed on a substrate of RI 1.457334. The PC is constructed on a polymer base of RI 1.327 (MY-132-V15K) with nanorods (diameter 80 nm and pitch (a) 200 nm) of SOPRA-polysilicon 2 with 10% silicon. The in-plane PBG of the PC is shown in Fig. 2.
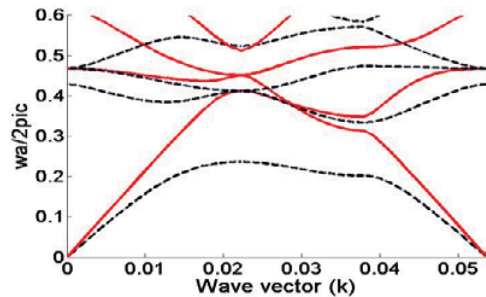
Fig. 2. Bandgap diagram of the PC. Dashed lines are for TM and solid lines are for TE polarization. ω is operating frequency, a is pitch, c is velocity of light in vacuum.

The structure has a TM band gap between 588nm to 833nm, but no TE band gap is present. The in-plane DOS (density of state) plot for the structure is given in Fig. 3. The DOS plot shows the variation of the number of permissible EM modes in the crystal structure with normalized frequency [3].
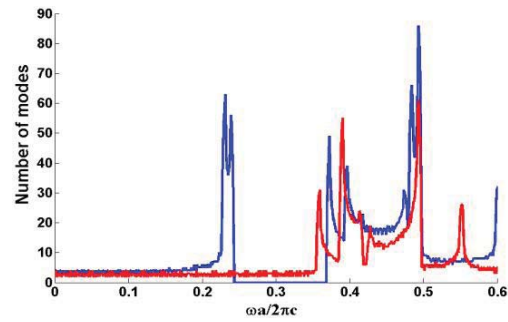
Fig. 3. The DOS plot of the proposed photonic crystal. The red line is for TE modes and blue line for TM modes.

It can be shown from Fig. 3 that there are no TM modes when ωa/2πc varies from 0.24 to 0.34. On the other hand this region has nonzero DOS value for TE modes. This means in the mentioned frequency band only the TM mode will propagate through the defect channel.

B. Design of plasmonic sensor

We are interested to design an integrated sensor. We first took a four layer plasmonic waveguide structure. The schematic diagram of the plasmonic structure is shown in Fig. 4.
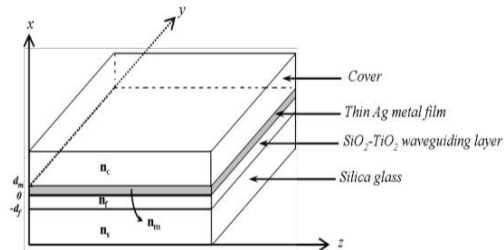
Fig. 4. . Four layer planar waveguide structure with embedded thin metal layer of silver (Ag).

The structure is assumed to be infinite in y direction and the refractive index distribution is given by [4].

$$n(x) = \begin{cases} n_c , x > d_m ,\text{cover} \\ n_m , d_m > x > 0, \text{metal} \\ n_f ,0 > x > -d_f, \text{film} \\ n_s, x < -d ,\text{substrate} \end{cases} \qquad (3)$$

The structure is optimized to support only the fundamental modes in the specified bandgap region. The refractive index of the guiding layer is taken as 1.7264. In order to achieve a better coupling between the plasmonic mode and the guided mode we set the thickness of the metal layer to 40nm.
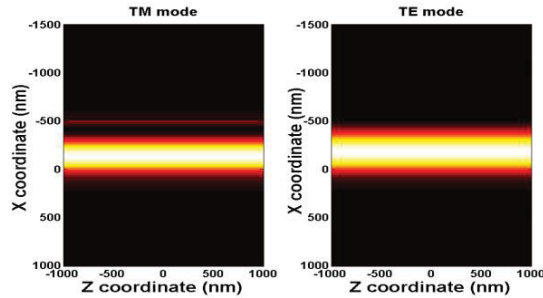
Fig. 5. Fundamental TM and TE mode field distribution for ns=1.457334, nf=1.7264, nc=1.33, df=550nm and dm=40nm. The metal layer is considered as silver layer. RI of Ag is calculated from ref. [5].

Now we varied the thickness of the guiding layer and found out that when df is below 580nm only the fundamental TE and TM modes are supported in the structure. This optimization is carried out by fixing the cover layer index to 1.33 and operating wavelength is taken 632nm. The modal field distribution is shown in Fig.5.

The interaction between the core guided fundamental TM mode and the surface plasmon polariton (SPP) can be enhanced farther by wall perturbation method. If the interface between the metal layer and the adjacent dielectric layer is perturbed in a symmetric fashion then the plasmonic response of the structure increases. The schematic diagram with triangular perturbation is shown in Fig. 6.
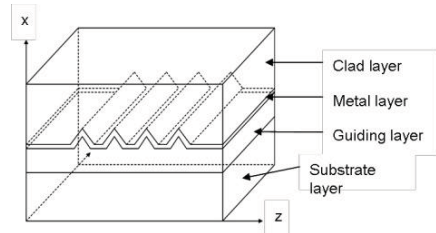
Fig. 6. . Schematic diagram of the waveguide with triangular wall perturbation with surface metal layer.

In an earlier study we showed that the wall perturbation increases the surface plasmon (SP) amplitude [4]. Hence more power will be coupled out from the guided mode. The variation of SP amplitude with different cover index for various perturbations is shown in Fig. 7.
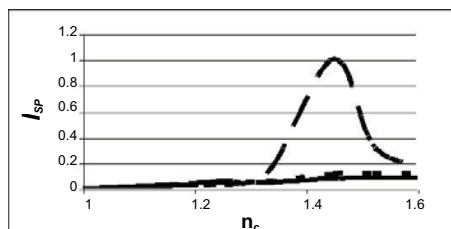
Fig. 7. Variation of normalized SP amplitude (ISP) at metal-clad interface with clad index (nc) for different grating geometry at the interface. Solid line for without perturbation, dashed line for rectangular and broken line for triangular perturbation.

We now integrated the two structures to design a polarization selective plasmonic sensor. The main advantage of this integrated structure is its efficiency. Since the guided mode in the PC is used to excite the plasmonic structure so better light coupling is expected. The schematic diagram of the integrated device is shown in Fig. 8.
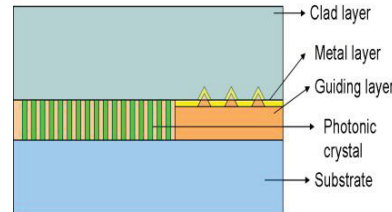
(a)
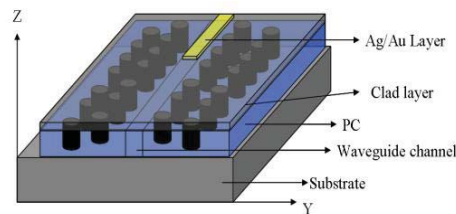
(b)

Fig. 8. (a) Cross-sectional schematic view of the integrated sensor device. (b) 3D schematic view of the sensor structure`

III. SIMULATION AND RESULTS

We analyzed wave propagation through the structure y Lumerical FDTD engine to observe the evolution of the propagated core guided mode. We calculated the change in the guided mode amplitude for different refractive index of the clad layer. We set the wavelength to 632nm as LED sourced at this wavelength is widely available. We set the cover layer index to 1.33 (water) as the intention is to use it as a biosensor. We excite the structure with a plane wave source. The propagation of fundamental TE and TM mode is shown in Fig. 9.

(a)

(b)
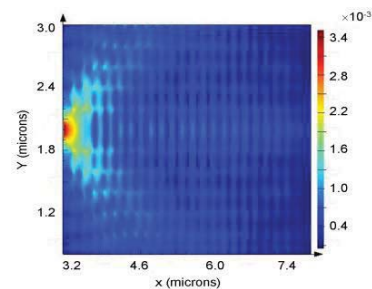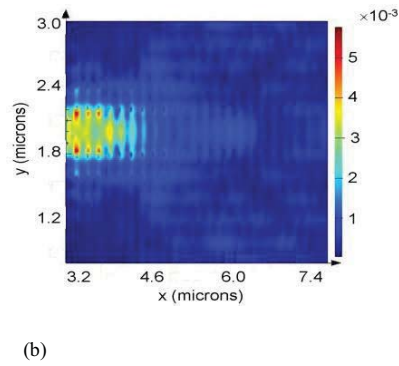
Fig. 9. Propagation of light through the integrated sensor (a) TE polarized (b) TM polarized

From Fig. 9 one can clearly infer that only the TM mode will be coupled to the sensor structure. The TE light readily leaks out through the PC cladding within a propagation distance of 1μm. We took the cavity channel 5μm long and the sensor structure (3μm long) is embedded within it. The normalized TE and TM mode amplitude after a propagation length of 8μm for different cover index is shown in Fig. 10.
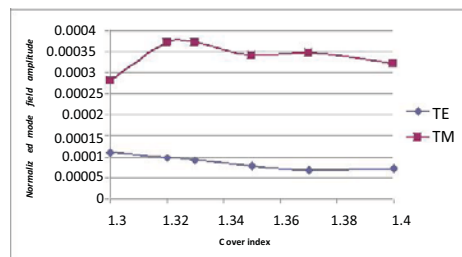
Fig. 10. Variation of normalized TE and TM output amplitude with cover refractive index.

We can conclude from Fig. 10 that TM polarized output dominates in the output signal. We compared the output TM and TE amplitude ratio of the sensor structure embedded in the PC and without PC. The result is shown in Fig. 11.
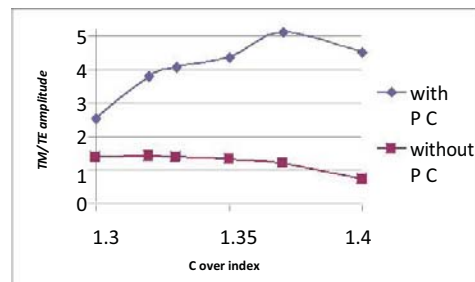
Fig. 11. TM/TE amplitude variation with cover refractive index TM/TE amplitude variation with cover refractive index.

Fig. 11 shows that detection of TM signal is much easier in our proposed structure. So the SNR will increase as the TE output will act as noise. The PC helps to cut down the TE response and thus the structure gives a better signal detection.
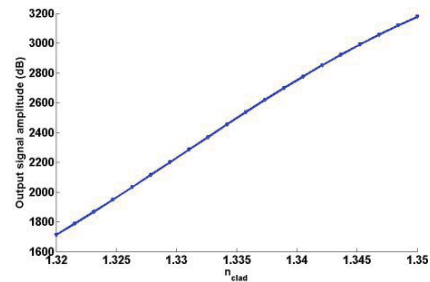
Fig. 12. . Variation of output signal TM amplitude with Cover refractive index.

Since we intend to use amplitude variation measurement technique to detect the sample, which will act as cover layer, it is needed that the output signal should vary linearly in the desired RI region. Fig. 12 shows that the signal varies linearly in the region 1.32 to 1.35, which is the most desired range. The sensitivity is 50238 dB/ RIU.

IV. CONCLUSION

The proposed sensor offers linear and polarization selective operation in the RI region suitable for bio-fluids. The refractive index of the cover medium can be estimated by observing the amplitude of the output signal. The intensity of the output signal changes linearly with cover index. The introduction of PC enhances the SNR ratio and the perturbation increases the sensitivity. The total structure is compact and can be designed on a chip.

References

[1] J. Homola, S. S. Yee and G. Gauglitz, "Surface plasmon resonance sensors: review", Sensors and Actuators B, 54, 3-15 (1999).

[2] A. A. Mradudin and A.R. McGurn, "Out of plane wave propagation of electromagnetic waves in a two dimensional periodic dielectric medium", J. Mod. Opt. 41, No-2, 275-284 (1994).

[3] K. Sakoda, Optical properties of photonic crystal (Springer-Verlag, Berlin Heidelberg, 2005).

[4] R. Chattopadhyay, R. D. Roy and S. K. Bhadra, "Sub-micron plasmonic waveguide for efficient sensing of bio-fluids", PIER Lett. 41, 1-12 (2013).

[5] A. D. Rakic´, A. B. Djurisˇ ic´ , J. M. Elazar, and M. L. Majewski, "Optical properties of metallic films for vertical-cavity optoelectronic devices", App Opt. 37, No. 22, 5271-5283 (1998).

Comparative analysis of Dual Tail Comparator using Clock Gating Technique

Akanksha Singh
Research Scholar
ECE Department
ITM University, Gwalior (MP)
akankshasingh.singh469@gmail.com

Ayushi Marwah
Assistant Professor
Department of Electronics and
Communication, ITM University,
Gwalior (M.P.)
er.ayushi10@gmail.com

Shyam Akashe
Professor
Head of Department
Electronics and Communication
ITM University, Gwalior (M.P.)
shayam.akashe@itmuniversity.ac.in

Abstract: **This paper presents the comparison of dynamic latch comparator with dual tail comparator. Dual input in the circuit is compared and single output respective to the input provided is acquired from the opposite end. Comparator circuit should consume less power and should have a high speed of operation. With the proposed design the amenities of the comparator circuit is obtained. Since scaling of transistor size is taking place, so the circuit is designed in 45nm technology. The supply voltage for the circuit is also very low as compared to other conventional based design. With the proposed design the efficiency of the circuit obtained is higher than the conventional design with reduction in the leakage current and leakage power in the design. The circuit is simulated at 45 nm technology with the supply voltage of 0.7 volts.**

Keywords: **dynamic latch comparator, dual tail comparator, power consumption, speed, efficiency, leakage power**

I. INTRODUCTION

Comparator circuit is the basic building block of both digital and analog circuit. Circuit is used for the comparison of both the voltage and current signal. Basically two or more than two inputs are provided in the comparator circuit and single output is obtained from the other end depending of the input signal provided to it. Various designs where comparator circuit is used are in analog to digital signal, for sampling of the data, for comparison of voltage and current signals etc. Op-amp based design is used earlier for the designing of the

comparator circuit. Differential pair circuit is the basic comparator design. With the advancement in the VLSI technology scaling of the transistor sizing is taking place. So the circuit is designed with cmos transistor, FinFET for the better and effective result of the circuit. Clocked comparator circuit consists of 3 phases: pre-amplification, decision circuit and post-amplification circuit as shown in Fig1.
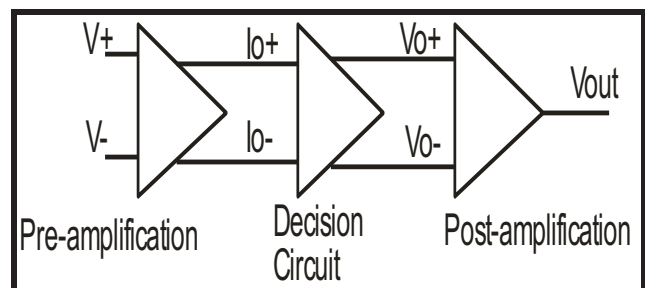
Fig1. Block Diagram of Comparator

Modifications in the circuit are being done for designing a good and effective circuit. Using the truth table of the basic comparator circuit one bit comparator circuit is designed and further eight bit comparator circuit is designed afterwards. It is observed that with the decreased in the current in the circuit power dissipation in the circuit is also decreasing effectively [1]. Variable Switching Voltage (VSV) circuit is implied in the flash ADC circuit for increasing the speed of operation in the design with lowering the peak power consumption in the design. The circuit is simulated in 65nm technology. A higher linearity is obtained using it with faster response time [2]. Comparator circuit is designed using the regenerative

latch and SR latch. With the inclusion of the latch in the circuit the kickback noise in the circuit is reduced. Circuit is operated with low voltage and with higher speed. With the elimination of the kickback noise faster speed in the design is obtained [3]. ADC circuit with preamplifier and regenerative latch provides with faster operation speed and better sensitivity in the design. Input referred offset voltage is also adjusted using the proposed design of the circuit [4]. Circuit is designed using two differential circuits. Differential circuits replacing the normal input leads to faster output response with lower power consumption in the design. A better response in terms of speed and power consumption is obtained using it [5].

Comparator circuit is used for various applications in the design. Comparator circuit is used with back-gate and clock boosting technique. These designs are used in low voltage and wide range operation. It is used in small signal processing and basically in SOC [6]. Differential signal is placed in place of normal input of the comparator circuit. With the proposed design a higher operating speed with lower power consumption in the circuit is obtained [7]. Dual tail circuit came into existence for the higher output response in the circuit. The circuit is designed for operating with higher speed and lower power consumption [8]. Circuit is modified with triple-tail cell. The main advantage of the circuit as compared to other design is the operation of circuit at higher speed. It has better output response as compared to the conventional design [9]. For further reducing the power consumption and leakage power in the design clock gating technique is used. Clock gating technique is applied in the dual tail circuit for the reduction of power consumption in the design along with faster speed of operation [10]-[11]. Dual tail comparator circuit is compared with the conventional comparator design and the output of the circuit is observed and calculated. A better and effective result is acquired using the former design [12]. Clock gating technique is implemented in the dual tail circuit. The modified circuit shows faster operating speed with lower power consumption in the design [13]. Dual tail comparator circuit is simulated in cadence and parameters of the circuit is observed and calculated. Various conventional circuits are simulated along with the proposed design. Comparison of all the circuit is observed and made with the proposed design [14].

II. WORKING OF DYNAMIC LATCH COMPARATOR CIRCUIT

Conventional dynamic latch comparator circuit has high input impedance, rail-to-rail output swing and lower static power consumption. The operation of the circuit works in two phases: Firstly the reset phase. It includes when the

clock "clk" = 0 and Mtail is off. During this phase the transistor M7 and M8 will get reset. Thus it will pull both the output i.e., outp and outn to VDD and thus it then is the starting condition of the circuit or the circuit is in reset phase. The cmos implementation of dynamic latch comparator is shown in Fig2. Second is the comparison phase i.e., when the "clk" = VDD. Transistor M7 and M8 will be off and Mtail will be on. Both the output outp and outn are on VDD. They eventually start to get discharged at different rates. When Vinp>Vinn then outp discharges at a much faster rate than outn, and hence outp discharged by drain current of transistor M2, falls down to VDD before outn which is being discharged by drain current of transistor M1. Thus the PMOS transistor M5 will get turn on leading to latch regenerative speed. This causes back-to-back regenerative feedback path by transistor M3, M5, M4 and M6. Thus outp discharges to ground and outn pulls to VDD. When Vinp<Vinn the reverse process follows.
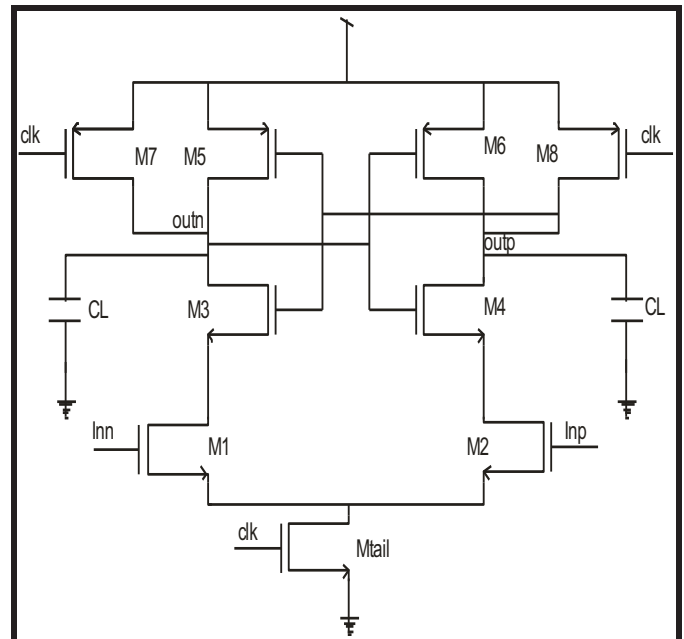
Fig2. Dynamic Latch Comparator

III. WORKING OF DYNAMIC LATCH COMPARATOR USING CLOCK GATING

Clock gating phenomenon is used in the circuit for controlling the clock signal given in the circuit. As we know clock dissipates nearly 70% of power in the circuit, so clock gating in the circuit is done. Clock gating is basically of two types: Local gating and Global gating. In the former one gating signal is provided to separate module in the circuit while in the later one gating is provided to the universal clock pulse which further is distributed to the entire circuit in the design. Clock gating implementation is depicted in Fig3.
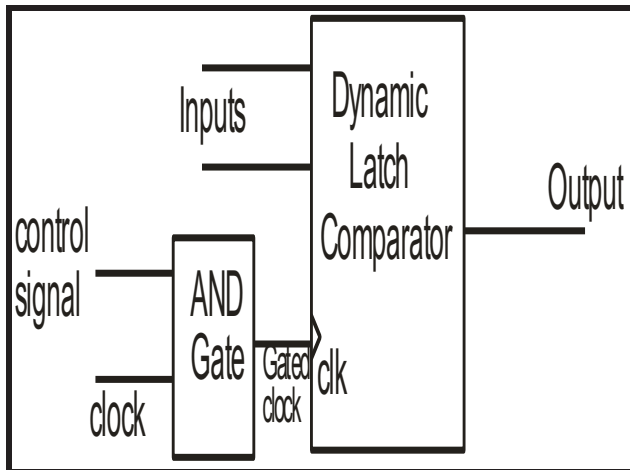
Fig3. Dynamic Latch Comparator using Clock Gating

In the circuit when both the enable signal and clock signal is high then the gated signal will proceed further and the output from the circuit will be obtained.

IV. WORKING OF DUAL TAIL COMPARATOR CIRCUIT

The main advantage of the circuit from the other conventional design is operating at lower supply voltage. Dual tail circuit enables large current in latching stage along with wider Mtail2 in the regenerative latching path. It is independent of input common mode voltage with small current in input stage for low offset. In the reset phase clk = 0, Mtail1 and Mtail2 are off. M3 and M4 transistor are pre-charged, fn and fp nodes to V$_{DD}$ which further causes transistors MR1 and MR2 causing the output nodes to ground signal. During the decision making phase i.e., clk = V$_{DD}$, Mtail1 and Mtail2 is on. This leads to transistors M3 and M4 turning off which further leads to voltage drop from nodes fn and fp. Transistors MR1 and MR2 forms the intermediate stage. Node fn passes from the cross coupled inverter and result in good shielding between the input and output signal leading to reduction of kickback noise. CMOS implementation of dual tail comparator circuit is depicted in Fig4.
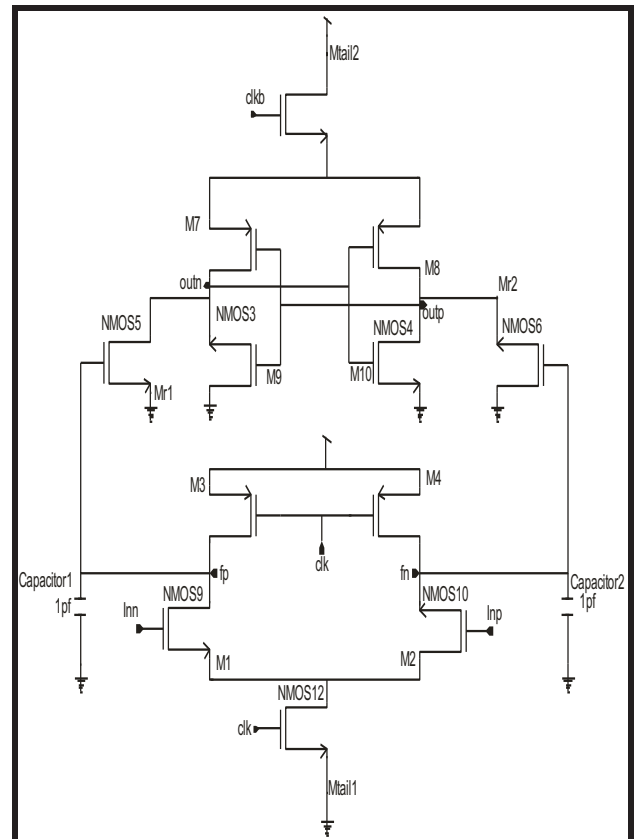
Fig4. Dual Tail Comparator Circuit

The output voltage acquired at the first stage output at time t0 has its effect on the initial differential output voltage with latch delay. Delay of the circuit is reduced by the design. In the intermediate stage, transistor will be in cutoff mode fn and fp nodes are discharged to ground. During the reset phase, the nodes are charged from ground to V$_{DD}$ causing high transient noise in the regeneration time with low kickback noise voltage.

The circuit has higher energy with input referred as offset voltage than conventional dynamic latch comparator. The dual tail circuit consists of two current paths which further increases the performance of the circuit.

V. PARAMETERS CALCULATED

1) Power Consumption
2) Delay
3) Power-delay Product
4) Voltage Gain
5) Efficiency
6) Leakage Power

POWER CONSUMPTION

It is defined as the total power consumed by the circuit. Power consumption in the circuit means how much power

should be provided in order to drive a load and provide us output. Power consumption causes due to two factors: static and dynamic. Static power comes into existence when circuit is in idle mode. It is defined as the product of voltage and current. While dynamic power is defined as the power consumption in the run mode. It is proportional to the switching activity of the clock pulse, capacitance, supply voltage and frequency of the design. More the supply voltage, more the power consumption in the circuit.

Power (Ptotal) = Static power + Dynamic Power   (1)

$$P(t) = (Vdd) * (Idd(t)) \qquad (2)$$
$$P(dynamic) = \alpha C (Vdd)^2 f \qquad (3)$$
$$P(static) = I(static) * Vdd \qquad (4)$$

Energy consumed by the circuit is given by

$$E = \int_0^T (Vdd)(Idd(t))\, dt \qquad (5)$$

$$Pavg = \frac{E}{T} = \left(\frac{1}{T}\right)\int_0^T (Vdd)(Idd(t))\, dt \qquad (6)$$

Table I. Comparison table of Power Consumption

	Dynamic Latch Comparator	Clock Gating in Dynamic Latch Comparator	Dual Tail Comparator Circuit
Watt	13.07n	64.39p	740.0f

DELAY

The most important property of a comparator circuit is the operating speed of the circuit. Delay in circuit is defined as the time taken to provide us with output when input is provided to the circuit. It occurs due to the presence of parasitic capacitance in the design. The charging and discharging of parasitic capacitance causes the occurrence of propagation delay in the circuit. Using the dual tail technique the operating speed of the circuit is higher as compared to the conventional design of comparator.

$$Delay(\tau) = 0.69\, RC \qquad (7)$$
$$Delay(\tau) = \frac{T(rf) + T(fr)}{2} \qquad (8)$$

Where T (rf) = time for rising to falling and T (fr) = time for falling to rising

Table II. Comparison table of Propagation Delay

	Dynamic Latch Comparator	Clock Gating in Dynamic Latch	Dual Tail Comparator Circuit

		Comparator	
nsec	12.609	10.56	9.32

Fig5. represents the comparison chart of delay of the circuits.
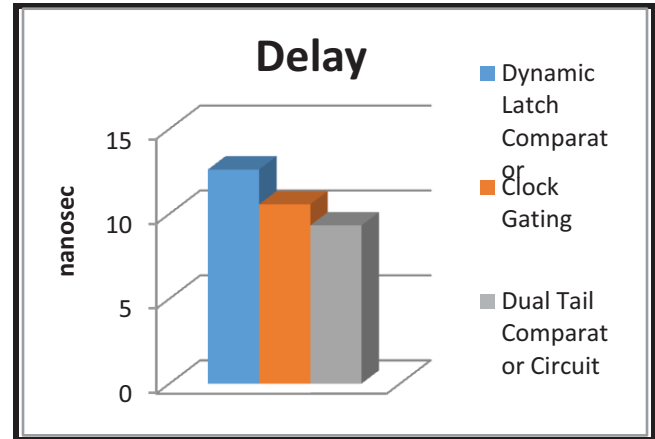
Fig5. Comparison Chart of Delay

POWER-DELAY PRODUCT

It is defined as the product of both the power consumption and propagation delay of the circuit. Lower the power delay product of the circuit, better the circuit is.

$$PDP = Pavg * (\tau) \qquad (9)$$

Table III. Comparison table of Power–Delay Product

	Dynamic Latch Comparator	Clock Gating in Dynamic Latch Comparator	Dual Tail Comparator Circuit
pdp	164.79e-18	6.79e-19	6.89e-21

VOLTAGE GAIN

It is defined as the ratio of output voltage to input voltage. Voltage gain is measured in terms of dB. With the dual tail technique in the circuit, voltage gain in the circuit has increased effectively.

$$Voltage\ Gain = 10 \log\left(\frac{Vout}{Vin}\right) dB \qquad (10)$$

Vout is Output Voltage acquired and *Vin* is Input Voltage supplied

Table IV. Comparison table of Voltage Gain

	Dynamic	Clock	Dual Tail

	Latch Comparator	Gating in Dynamic Latch Comparator	Comparator Circuit
dB	18.09	20.40	21.4

Fig6. represents the comparison chart of voltage gain of the circuits.
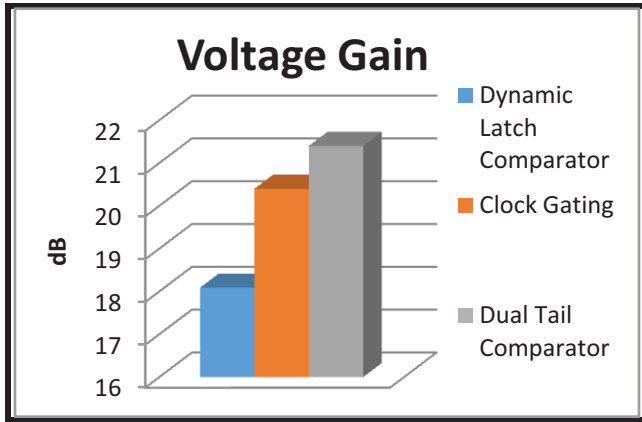
Fig6. Comparison Chart of Voltage Gain

EFFICIENCY

It is calculated as the ratio of both output power to input power. If is defined in terms of percentage. With the dual tail comparator circuit a better and efficient output for the circuit is acquired.

$$\eta = \frac{Pout}{Pin} \qquad (11)$$

Where, *Pout* is the power calculated at the output terminal and *Pin* is Power delivered at the input

Table V. Comparison table of Efficiency

	Dynamic Latch Comparator	Clock Gating in Dynamic Latch Comparator	Dual Tail Comparator Circuit
%	28.9	29.6	46.5

Fig7. represents the comparison chart of efficiency of the circuits.
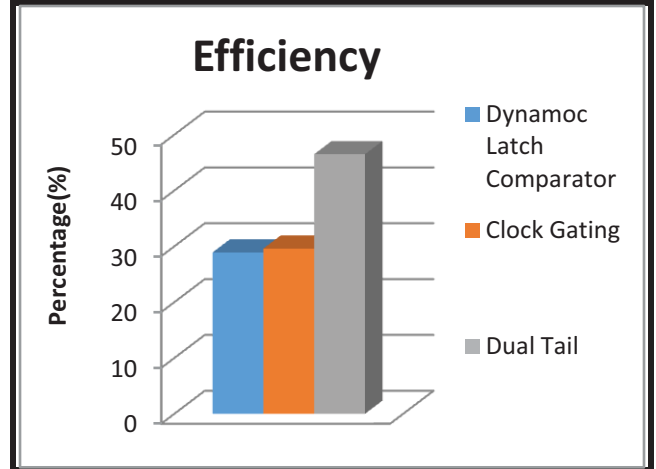
Fig7. Comparison Chart of Efficiency

LEAKAGE POWER

Due to the presence of short channel effects leakage power occurs in the transistor. It occurs basically when the circuit is sin sleep mode. Leakage current can lead to losing of data and thus leakage current along with leakage power should be minimal for the circuit. It is the product of leakage current and leakage power in the circuit.

$$P\ (leak) = \ I\ (leak) * Voltage \qquad (12)$$

Table VI. Comparison table of Leakage Power

	Dynamic Latch Comparator	Clock Gating in Dynamic Latch Comparator	Dual Tail Comparator Circuit
pW	100.6	72.31	26.84

Fig8. represents the comparison chart of efficiency of the circuits.
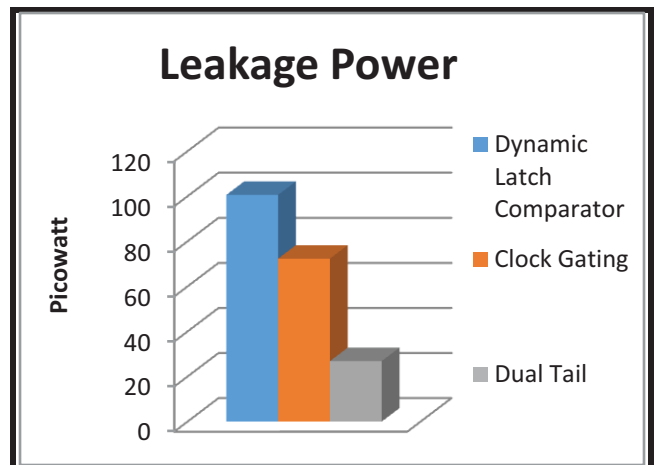
Fig8. Comparison Chart of Leakage Power

VI.   OUTPUT WAVEFORMS OBTAINED

1. The output of the comparator circuit is shown in Fig9. Input and output of the circuit at time interval is shown in the figure.
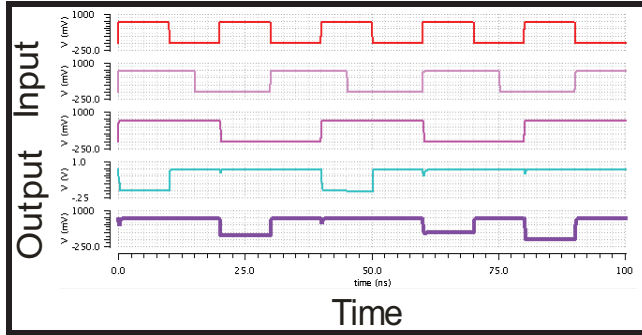
Fig9. Output of Comparator Circuit

2. Power consumption of the conventional comparator circuit is shown in Fig10.
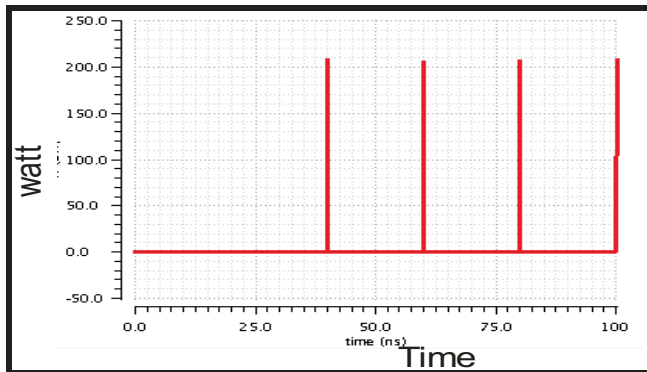
Fig10. Power Consumption Graph

3. Leakage Power of the conventional circuit is shown in Fig11.
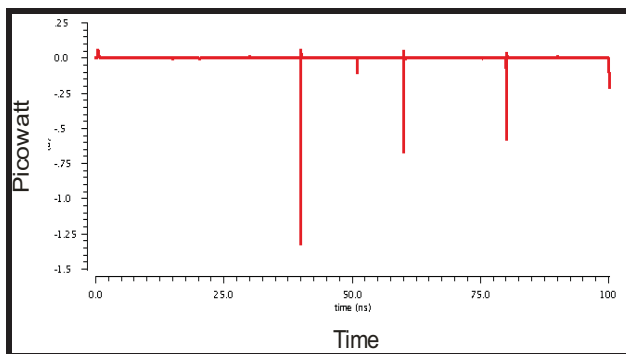
Fig11. Leakage Power Graph

VII. CONCLUSION

The comparison of three circuits is being done. All the circuits are simulated in 45nm technology with the supply voltage of 0.7 volt. Dual tail comparator circuit provides a higher voltage gain, efficiency with reducing the power consumption, propagation delay, leakage power in the design. The dual tail circuit provides with better and efficient output at a faster rate and with low supply voltage. Parameters like power consumption, power-delay product and leakage power is reduced by 98%, 98.9% and 73.32% respectively. While the voltage gain and efficiency in the circuit is raised by 18% and 60% respectively. With the proposed design the delay in the circuit is reduced to 9.32 nsec from 12.609 nsec respectively.

REFERENCES

[1]   S. K. Jaiswal, K. Verma, G. Singh, and N. Pratihar, "Design of CMOS 8-BIT comparator for low power application," *Proc. - 4th Int. Conf. Comput. Intell. Commun. Networks, CICN 2012*, pp. 480–482, 2012.

[2]   G. Ahmed and R.K. Bhagel, "Design Of 6-Bit Flash Analog to Digital Converter Using Variable Switching Voltage Cmos Comparator," VLSICS, vol. 5, no.3, June 2014

[3]   H. J. Achigui, C. Fayomi, D. Massicotte, and M. Boukadoum, "Low-voltage, high-speed CMOS analog latched voltage comparator using the flipped voltage follower as input stage," *Microelectronics J.*, vol. 42, no. 5, pp. 785–789, 2011.

[4]   F. Brianti, A. Manstretta, and G. Torelli, "High-speed autozeroed CMOS comparator for multistep A/D conversion," *Microelectronics J.*, vol. 29, pp. 845–853, 1998.

[5]   M. B. Guermaz, L. Bouzerara, a. Slimane, M. T. Belaroussi, B. Lehouidi, and R. Zirmi, "High Speed Low Power CMOS Comparator for Pipeline ADCs," *2006 25th Int. Conf. Microelectron.*, no. Miel, pp. 14–17, 2006.

[6]   Y. C. Hung and B. Da Liu, "A low-voltage wide-input CMOS comparator for sensor application using back-gate technique," *Biosens. Bioelectron.*, vol. 20, pp. 53–59, 2004.

[7]   S. Shubhanand and a G. Rao, "Design and Simulation of a High Speed CMOS Comparator," vol. 6, no. 1, pp. 75–80, 2013.

[8]   C. A. S. B. E and M. E. V. Design, "Design of a Novel High Speed Double-Tail Comparator," vol. 3, no. 1, pp. 11–14, 2014.

[9]   K. Gupta, N. Pandey, and M. Gupta, "MCML D-Latch Using Triple-Tail Cells : Analysis and Design," vol. 2013, 2013.

[10]   N. Akshaya and A. Sridevi, "Design of Low Power Efficient Double Tail Comparator Using Clock Gating Technique,"IJRDO, vol. 2, no. 4, pp. 2–6, 2015.

[11]   R. Manopriya and M. Karthik, "Design of Low Power and High Speed Double Tail Comparator Using Clock Gating Method," IJERST, vol. 4, no. 1, Feb 2015

[12]   K. Radhika, K. Priyameenakshi, and M. E. College, "Analysis and Optimization of Dual Tail Comparator," vol. 1, no. 9, pp. 251–255, 2014.

[13]   A. Akshaya, B. Sridevi, and C. B. Joy, "Design of Low Power Area Efficient Double Tail Comparator," vol. 2, no. 1, pp. 295–299, 2015.

[14]   S. Ghosh and S. Sharma, "Design of A Novel High Speed Dynamic Comparator with Low Power Dissipation for High Speed ADCs," pp. 411–426, 1956.

Recording of Holographic Solar Concentrator in Ultra Fine Grain Visible Wavelength Sensitive Silver Halide Emulsion

Recording of Visible wavelenght Concentrating Hologram

Vadivelan V

Research Scholar
Research and Development Centre,
Bharathiar University
Coimbatore – 641046,
Tamilnadu, India
vvelan@gmail.com

Chandar Shekar B

Assistant Professor
Nanotechnology lab
Physics Department, KASA
Coimbatore- 641029
Tamilnadu, India

Abstract—**Holography is an optical technique which is involved in the solar applications specifically solar concentration. Visible spectrum of solar light concentration on wavelength depended solar cells is effective way to enhance the diffraction efficiency of the solar cells, this is prime aim of this work. Initial step of successful recording of high diffraction efficiency phase holographic optical element were recorded. For this, we used ultra fine grain visible wavelength spectral sensitive silver halide holographic emulsion from Ultimate holography. The novelty of this work is three different laser sources of 442nm, 532nm and 633nm were used for multiplex holographic transmission lens in a same emulsion and applied for solar concentration. We optimize exposure sensitivity for each laser wavelengths and combined wavelengths in order to obtain the multiple band response of the material. The detail study of holographic optical elements recording is explained.**

Keywords—Holographic Optical elements, Holography, Solar Energy, Holographic Lens, Wavelength Multiplexing, Diffraction Efficiency, Holographic Lens, Solar Cells.

I. INTRODUCTION

Precise knowledge of solar irradiance components at the earth surface is leads to many solar energy applications. India is endowed with rich solar energy resource since it is located in the equatorial sun belt of the earth. The daily average solar energy incident over India varies from 4 to 7 kWh/m^2 with about 2,300–3,200 sunshine hours per year, depending upon location. This is far more than current total energy consumption. The annual global radiation varies from 1600 to 2200 kWh/m^2, which is comparable with radiation received in the tropical and sub-tropical regions. Thus it is clear that solar power projects are commercially viable in most parts of India. Specifically conversion of solar energy into electric energy is highly important to meet at current energy crises, it is one of the most important and promising application of solar energy for the current world. One of an approach to increase the conversion efficiency of the solar cell is concentration of solar light on the solar cells. Many conventional solar concentrators are involved to concentrate the solar light to enhance the conversion efficiency of the solar cells [1]. Current trends demand that the photovoltaic (PV) concentrators must achieve various goals of lowering costs at all levels and/or increasing the energy yield [2]. Conventional concentrators are complicated and some of it needs cooling and tracking system. Alternative technique of holography is an optical method that can provide a variety of improvements to existing solar energy conversion devices and systems. Holographic Optical Elements (HOEs) are very good example of optical concentrators and have been suggested for use as solar concentrators. The diffraction and

the dispersion properties of HOEs are examined for use as solar concentrators for photovoltaic systems [3,4]. Advantage of holographic optical elements are light weight, durable, economical, less expensive, easy reproduction, low cost in terms of mass production and multifunctional, thus holography offers an ideal spectrum splitting for photovoltaic conversion [5]. Holographic Solar Concentrator (HSC) in different holographic emulsion are mentioned here, recently HSC recorded in photopolymer is reported by Sam et al [6] but self life, material availability and stability should be reconsider. HSC in surface relief material has been reported [7]. Stojenoff works related with HSC in Dichromated Gelatin has been reported [8,9]. Almost all the HSC has been recorded by using single wavelength and the holographic emulsion is also sensitive to particular wavelength only. In this work, we used visible color sensitive ultra fine grain holographic emulsion from Ultimate Holography and from our knowledge; this is first time three visible laser sources are used for the fabrication of HSC. We successfully recorded the HSC and its characteristics are discussed in details. HSC capability of concentrating the wanted wavelength of solar spectrum into the desired direction can concentrate light on the wavelengths dependable solar cells and it will help to enhance the system efficiency 30-40%. One of a main advantage of a holographic solar concentrator as compared to a conventional one is seen in the overall reduction of investment cost and in the possibility to generate inexpensive solar electric power [9,10].

II. EXPERIMENTAL ARRANGEMENT

Three laser sources of 442 nm, 532nm and 633nm are used to record the HSC, here we recorded holographic transmission lens as HSC. The detail of the experimental layout is follows. The laser beam is divided into two beams by using variable density beam splitter (BS) and the two divided beams named as reference and object beams. The object beam is redirected from Aluminum front coated mirror (M1) to the recording plate (HP) with the desired angle, in between it was spatially cleaned by spatial filter (SF1) and the distance between HP and SF1 decides the focal length of the Holographic Optical Element. Another beam called reference beam is expanded and specially cleaned by using spatial filter arrangement (SF2) and collimated by lens (L1). The spatially filtered collimated beam and diverging beams are interfered at the ultra fine grain silver halide holographic emulsion at HP. The schematic of the experimental arrangement is shown in figure 1 red wavelength He-Ne laser.
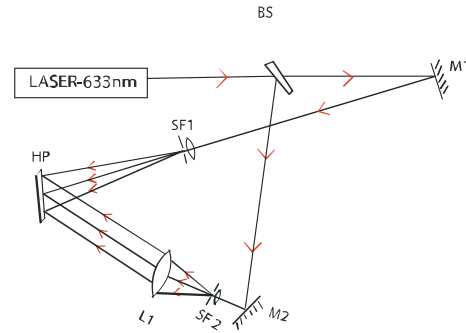
Fig. 1. Schematic of holographic lens recording
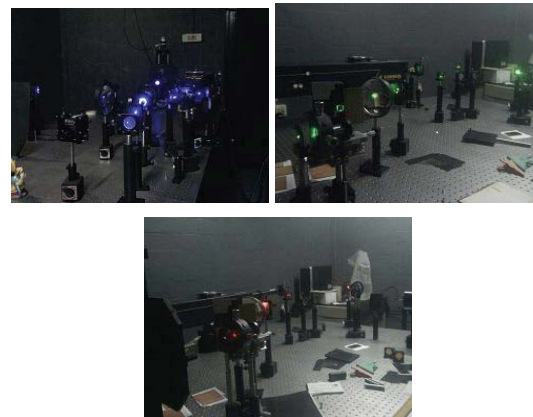
Fig. 2. Experimental Arrangement for Holographic Lens recording in Blue, Green and Red Wavelengths

The Uniblitz electronic shutter allows the interference of the two beams as per their exposure sensitive, it is not shown in the schematic. Again the same procedure followed for other two laser sources of wavelengths 442nm and 532nm by replacing the laser sources without disturbing the optical layout. Initially experiments were carried out to optimize the exposure sensitivity for each laser source by trial and error methods, once it was optimized for all the three wavelengths, then calculated the right exposure sensitivity for all the three wavelengths. The exposure sensitivity is optimized by trial and error method for all the laser sources separately as well as combined. The whole experimental set up is arranged on the top of vibration isolation table and it is shown in figure 2. The recorded wavelength dual – beam multiplex transmission holographic lens is processed by developer - bleach combination as phase hologram. The obtained results are discussed in result and discussion section. The same experiment is followed for other two lasers too and the beams are interfered at the same area of the plate. The recorded interference patterns under the safe light condition with optimized laser exposures is processed by developer - bleach combination.

III. RESULT AND DISCUSSION

High diffraction efficiency of over 50% was recorded and also high visible transmission was achieved by using Ultimate developer and modified rehalogenating bleach combination. High diffraction efficiency of hologram is achieved by using Silver Halide as a phase modulation material that is bleached holograms. We modification R10 bleach from the standard bleach by only chemical concentration, we used Pottasium Dichromate (1g), Pottasium Bromide (35g) and Sulphuric Acid (1ml). The recording of holographic solar concentrator in three laser wavelengths multiplexed on a single element is first time reported as per our knowledge. The advantage of holographic solar concentrator is spectrum splitting and concentration but here we have split the spectrum and paid attention for concentration of specific wavelengths on visible
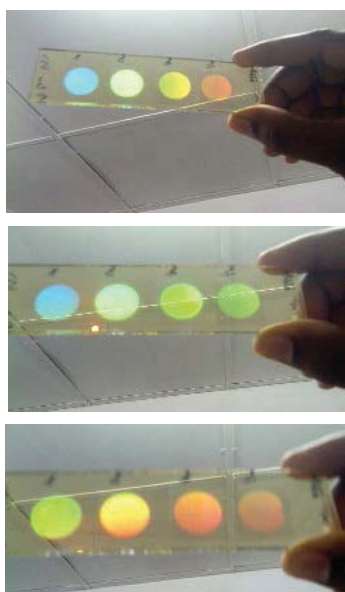
Fig. 3. Transmission Holographic Lens Recorded by Three Visible Laser Wavelengths.

wavelength dependable solar cells. Exposure sensitivity of the plate for all three wavelengths was inspected by exposed the plate separately ranging from $100\mu J/Cm^2$ to $2000\mu J/Cm^2$. Also exposure of the HSC was performed sequentially, starting with the blue wavelength of 442nm, followed by the green wavelength of 532nm and ending with the red wavelength of 633nm. A set of HSC with different exposure energy combinations for each wavelength was obtained, ranging from 120 through $225\mu J/Cm^2$ for the He-Cd laser, 150 through $225\mu J/Cm^2$ for green wavelength DPSS laser and 500 through $1000\mu J/Cm^2$ for the He-Ne laser. The recorded HSC is shown in figure 3. These HSC is applied to concentrate the specific wavelength on the wavelength dependable solar cells is continuous in further development of this. This will without doubt enhance the conversion system efficiency to 30-40%.

We proposed this wavelength multiplexed holographic optical element with high efficiency as well as its spectrum splitting and focusing property can be applied for HSC. Spectrum splitting of HSC is shown in Fig. 4.
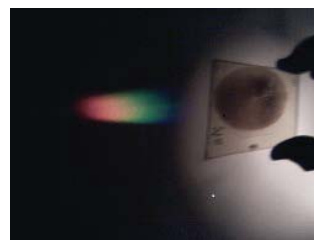
Fig. 4. Spectrum splitting of Holographic Solar Concentrator

IV. CONCLUSION

A Panchromatic silver halide holographic emulsion used for the fabrication of wavelength multiplexed holographic solar concentrator. We optimized the exposure sensitivity of the material separately for blue, green as well as red and also for combined wavelengths. Here we proposed the multiplexed element applied for concentrating the solar radiation to enhance the conversion efficiency of the cascade wavelength dependable solar cells. Also this material can be used to manufacture cost effective holographic beam combiner as well as color display holograms and photonic crystals. Further progressing research is going on for the device engineering.

Acknowledgment

References

[1] Marina Buljan, "Recent trends in concentrated photovoltaics concentrators' Architecture" J. Photon Eenrgy, 4(1), 040995 (2014).
[2] Nishikawa W., Horne S., Melia J., "LCOE for concentrating photovoltaics (CPV)," in Int. Conf. on Solar Concentrators for the Generation of Electricity (ISCS-5) , (Institute of Electrical and Electronics Engineers, New York, 1900), in Palm Desert, California (2008).
[3] Hull, J.L., Lauer J.P., Broadband, D.C, "Holographic solar concentrators", Proc. SPIE, 1987, 692, pp 68.
[4] Asghar Khan, N.R.Chakraborty and H.L.Yadav, "Compound Holographic Optical Element System for Splitting and Concentrating Solar Spectrum on Laterally- Arranged Multiple Band Gap Solar Cells" International Journal of Physics and Applications, 2013, Vol. 5, No. 3, pp 115-120
[5] D.V. Pulfrey, "Photovoltaic Power Generation" (Van Nostrand Reinhold Comp. New York, 1978).
[6] Sam et al., "Design and optimization of photopolymer based holographic solar concentrators" Amer. Inst. Of Phy conf optics: phenomena, materials, devices, and Characterization, conf. Proc. 2011, 1391, pp - 248-250.
[7] Ties M. de Jong,Dick K. G. de Boer,and Cees W. M. Bastiaansen," Surface-relief and polarization gratings for solar concentrators" OPTICS EXPRESS, 2011, Vol. 19, No. 16, pp -15127 – 15142.

[8] Stojanoff C.G. "A review of selected technological applications of DCG holograms" In: Proceedings of SPIE 7957; 2011.

[9] Stojanoff C.G. "The effects of the film manufacturing techniques, of the exposure procedures and of the development and post-treatment thermochemical processes on the holographic properties of HOEs in DCG" In: Proc SPIE 6252; 2006.

[10] J. E. Ludman," Holographic Solar Concentrator" Applied Optics, 21(17),

[11]Jose M. Castro, Deming Zhang, Brian Myer, and Raymond K. Kostuk,"Energy collection efficiency of holographic planar solar concentrator" Applied Optics, Vol.49, Issue5, pp. 858-870 (2010).

Applications of Planar Transmission Lines

Parnika Gupta, Khushi Arora, Shefali Chopra
Department of Electronics and Communication Engineering
Manav Rachna University

Abstract—The transmission lines are basically used in two ways either as a medium for signal transmission or as a circuit component. They can also be designed as impedance matching sources for antennas or stubs filters. The ease of fabrication of devices that use transmission lines for interconnection among the other sub-components of the circuit gives it an edge over the other tedious wiring methods. Planar transmission lines specifically stand out in this regard with respect to the latest fabrication technology being used for the nanoscale development of integrated circuits and at the same time playing a major role in radio frequency communication systems.

Index Terms-Antenna arrays, Band pass filter, Coupler, Power splitter, Resonators.

I. INTRODUCTION

The planar transmission lines and especially the microstrip lines has been a major field of study over the recent years. It has also attracted a lot of attention to its advantage of being modified to a patch antenna. The development of planar transmission lines for broadband communication suitability as well as for the manufacturing of monolithic microwave integrated circuits gives us a clear picture of the range of its applications and benefits.

II. APPLICATIONS OF MICROSTRIP LINES

A microstrip line is referred to as the quasi-TEM transmission line in which the microstrip is embedded on the surface of an insulating dielectric substrate with a ground plane on its parallel side as shown in Fig.1. These microstrip lines have an easily accessible top surface so that further fabrication of devices is highly convenient. But the losses due to the radiations and electromagnetic interference as well as the dimensions of the field external to the dielectric material makes it a source of technology to be used within constrained design. The dielectric material being used comprises of GaAs, Silicon etc. and it displays a Q-factor of 250 when the radiations are low and the Q-factor lies in the range of 100 to 150 for high radiations. Being small sized and easily integrable, these lines are used for a wide range of microwave circuit designs (MICs) like printed circuit lines for miniaturized microwave front end applications on the receiver side which includes devices such as mixers .These mixers are composed of microwave ring circuits containing balanced microstrip lines. In millimeter wave applications low power stages of integrated transmitter system [1] as well

as enhancement gain effects of power amplifiers adhering to CMOS transceivers for use in wireless communication [2] are also acknowledged to microstrip line applications in microwave circuits .The Wideband L-Band Suboptimum Class-E power amplifiers for RF and satellite communication are also structured with microstrip lines[3] .The microstrip technology is also tapped for Low pass L-Band microwave
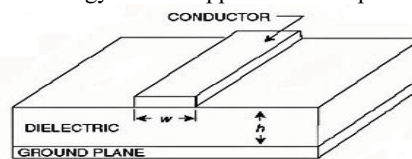
Figure 1: Microstrip Line

filters (stepped impedance microstrip lines)and modifying the characteristic impedance , conductor shape and dielectric material to improve circuit performance in communication systems[4].The microstrip band pass filter is employed in S-band of radio frequency for WiMAX (Worldwide Interoperability for Microwave Access) Application [5] .The shielded microstrip lines are the microstrip lines that are shielded by a metallic enclosure so that the electromagnetic interference losses are reduced and these are then casted for designing of microwave filters .These lines are also applied as couplers or adaptors for measurement of impedance or VSWR of electromagnetic devices[6].

III. APPLICATIONS OF STRIPLINES

Stripline (or suspended stripline) is a transmission line in which the conducting portion is immersed in a dielectric material with the metallic ground planes on either side of the dielectric which are mostly shorted to avoid the fields from escaping the dielectric substrate which emits radiation on a low scale, boasts on supporting a Q factor of about 500 and its load impedance may vary from 40 to 150 ohms.Fig.2 shows the above mentioned details of the stripline. The stripline accommodates the need for providing isolation among the various circuit sub-parts in a multi-layered circuit board though chip mounting is relatively difficult. The added advantage to a stripline is that its impedance can be varied to a larger extent as compared to that of microstrip lines because they allow more flexibility in the matter of positioning the conductor within the dielectric substrate. For the image decoding applications in the human head, where data obtained from transceiver array loops was juxtaposed with the data obtained from stripline transmission line array for 7 Tesla Parallel Imaging striplines were used [7].The Band pass filters are designed by utilizing the parallel coupled stripline stepped impedance resonator which controls the responses

and losses encountered by the resonators [8] since it can be used over a broad frequency range. Double conductor stripline and shielded stripline is also developed for use in the less tapered configurations while manufacturing of integrated circuits and where the circuit is susceptible to noise or signal distortion. Earlier, the striplines were considered a subpart of the microstrip line but over the years it has succeeded in carving out its own place in fabrication technology due to the presence of the conductor trace inside the substrate.
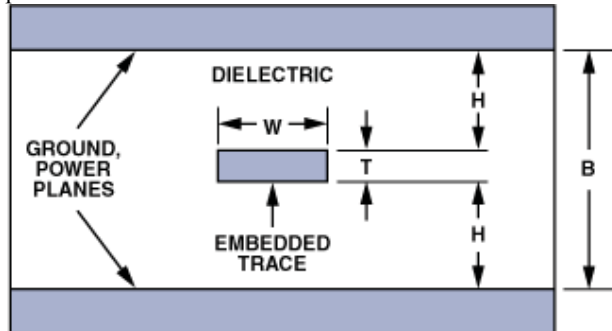
Figure 2: Stripline

IV. APPLICATIONS OF SLOTLINES

The slotline has a substrate whose one side remains as it is and the other side has a ground plane on which a narrow slot is
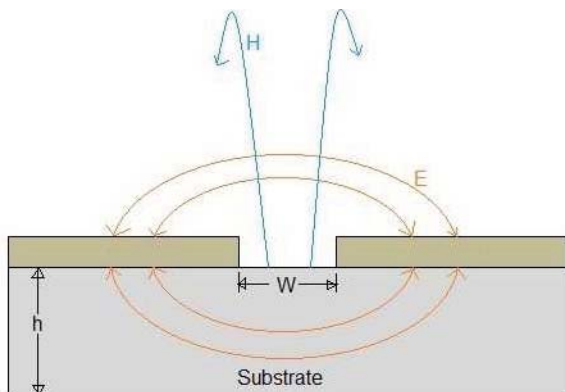
Figure 3: Field Configuration in a slotline

etched. It doesn't support TEM mode and is used in conjunction with microstrip line for designing circuits and it radiates moderately, has a high dispersion rate, supports a Q factor of about 100 which is less than that of the stripline and its impedance varies over a range of 60 to 200 ohms. The field density is limited within the substrate so, the higher order modes are suppressed as shown in Fig.3 and it supports the TE mode which is known for its diffusive nature so it is mostly not recommended for broadband applications except for Bilateral slotline or double slotline in which twin slot lines are etched on both sides of the substrate as it proffers less impedance and matching with stripline. When one end of the slotline is shorted its characteristics are similar to that of a half-wave resonator and by introducing a MEMS switch at the other end of the slot line transmission line, it can control the load of the slotline and thus microelectromechanical switches are used for application in the tunable resonator(digital frequency tuning).Annular rings generated from slotlines such as slot line ring resonators, slotline dual-mode Band Pass

filters are taken as a part of the circuitry in resonator filter and coupler applications which is significantly useful for MICS and MMICS[9].The millimeter wave technology which is apt for Wireless Communication Networks uses integrated NRD(Non-Radiative Dielectric) Guide and slotline for transmission of frequencies in the millimeter wave frequency region[10]. Certain changes are also being made to the traditional TSA(Tapered Slot Antennas) which is a kind of printed antenna for gain enhancement to be used at different frequencies for outer space communication as well as domestic communication purposes[11].The hybrid T-Junctions are also devised through the transition of Microstrip lines to slotlines which are further extracted for other circuit components such as power dividers, mixers and modulators such as ASK modulator, phase detector(since there is minimum amount of signal loss in the case of isolated coupled slotline). Due to an acceptable level of non-interference between balanced and unbalanced slotlines it also finds uses in feeding applications in rat-race hybrid junction, pulse inverters, couplers etc. with broader bandwidth graphs.

V. APPLICATIONS OF FINLINES
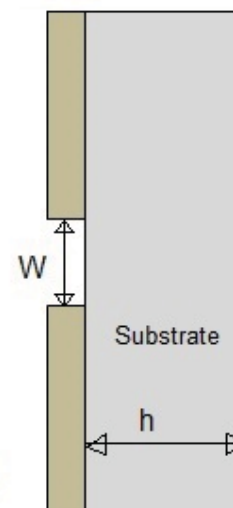
Figure 4: Finline

Finlines are basically the slotlines that are placed in the interior E-plane section of a rectangular waveguide which is evident from Fig 4. The substrate has low dielectric constant and it sustains a combination of TE and TM modes thus leading to low dispersion. It also yields circularly polarized fields that assist the working of non-reciprocal devices such as isolators and circulators. They emit the least amount of radiation or in some ideal cases –no radiations and their Q-factor is 500. The characteristic impedance is between 20 ohms and 400 ohms. Integrated finlines are mostly operated in the frequency range of 30 to 100 Gigahertz because at high frequencies there are lesser number of design constraints and these structures are used for low and medium power applications. The finline PIN diode switches as well as finline PIN diode attenuators in millimeter wave technology like Ultra Broadband PIN diode switches, PIN diode attenuators working in Ka-Band, Q-Band and W-Band. BPSK and QPSK modulators are also constructed from finline PIN diode phase

shifter and finline coupler and this technology further finds applications in communication systems in addition to balanced mixers using waveguide to Microstrip transition [12].

VI. APPLICATIONS OS COPLANAR WAVEGUIDES

In coplanar waveguides (CPW), a conductor strip and two ground planes are placed on the same plane above the substrate as proposed by Wen. The design of a coplanar waveguide is shown in Fig.5. The grounded coplanar waveguide (GCPW) has a ground plane below the substrate. The field is mostly confined within the thick substrate leading
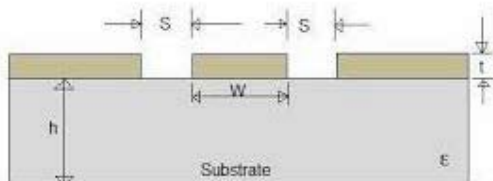
Figure 5: Coplanar Waveguide

to less dispersion and making CPWs the preferred choice for MMIC fabrication using GaN technology(Gallium Nitride based devices). CPW supports quasi TEM mode at low frequencies and TE mode at high frequencies leading to their application in microwave Integrated circuits (MICs). The impedance values range from 20 ohms to 250 ohms and the conductor strip can easily be tapered to a pin for facilitating attachable circuits in broadband communication. GCPWs are also applied in isolated RF switches, power splitters, filters and directional couplers due to the high degree of isolation between circuit components. Coplanar waveguide resonators are developed using temperature variations in superconducting material for detector applications [13]. MEMS switches (Microelectromechanical switches) applied in capacitive metal membrane shunt configuration and CPW resonator for X Band pass filters prefer CPW because of the presence of both the ground as well as conductor on the same plane [14-16].Waveguide to coplanar transitions are employed for communication in millimeter and centimeter frequency range [15]. Grounded CPW (GCPW) lines are used as pickup structures in Energy Beam Position Monitors operated within particle accelerators used Grounded CPW (GCPW) for the ease of transition to coaxial connectors later in the operation [17].

VII. CONCLUSION

Further advancements are being made by scientists and engineers all over the globe to improve the quality of transmission lines by variation in its characteristic properties. Already we are using optical fiber transmission for high-speed communication and this transmission speed is being improved for wireless communication using planar transmission lines.

REFERENCES

[1]   Prof. Usha Yadav**, "Simulation and Design Analysis of Integrated Transmitter System for Millimeter Wave Applications," International Journal of Advanced Research in Computer Science and Software Engineering, Volume 5, Issue 3, March 2015.

[2]   Sandeep, Neeraj, Mohit Sharma , "Enhancement Gain of CMOS PA using Microstrip line for Millimeter wave applications," INTERNATIONAL JOURNAL FOR RESEARCH IN APPLIED SCIENCE AND ENGINEERING TECHNOLO GY (I JRAS ET), *Vol. 2 Issue VI, June 2014,ISSN: 2321-9653.*

[3]   Francisco Javier Ortega-Gonzalez, David Tena-Ramos, Moises Patiño-Gomez,   Jose   Manuel   Pardo-Martin,   and   Diego Madueño-Pulido, "High-Power Wideband -Band Suboptimum Class-E   Power Amplifier," IEEE Trans. on Microwave Theory and Techniques, VOL. 61, NO. 10, OCTOBER 2013.

[4]   Omid Borazjani and Arman Rezaee, "Design, Simulation and Construction of a Low Pass Microwave Filters on the Micro Strip Transmission Line," *International Journal of Computer Theory and Engineering, Vol. 4, No. 5, October 2012.*

[5]   Avishek Das, Avisankar Roy, Kushal Roy, Amit Bhattacharyya, Dibyendu Chowdhury, "Design and Analysis of Microwave Planar Band Pass Filter for WiMAX Application," International Journal of Emerging Trends & Technology in Computer Science (IJETTCS), Volume 3, Issue 6, November-December 2014, ISSN 2278-6856.

[6]   Roddy,   Frank M. ; Sandia Corporation Albuquerque, New Mexico; Hewitt, Jack G, ".Use of Microstrip Transmission Line to Improve Broadband Electromagnetic Measurements," Electromagnetic Compatibility Symposium Record, 1969 IEEE, 17-19 June 1969.

[7]   Adriany G, Van de Moortele PF, Wiesinger F, Moeller S, Strupp JP, Andersen   P, Snyder   C, Zhang   X, Chen   W, Pruessmann KP, Boesiger P, Vaughan T, Uğurbil K, "Transmit and Receive Transmission Line Arrays for 7 Tesla Parallel Imaging," Magnetic Resonance in Medicine 53:434–445 (2005).

[8]   Makimoto, Mitsuo ; Sadahiko Yamashita, "Bandpass Filters Using Parallel Coupled Stripline Stepped Impedance Resonators," Microwave   Theory   and   Techniques,   IEEE   Transactions on (Volume: 28, Issue: 12).

[9]   Chien-Hsun Ho, Lu Fan, Kai Chang, "Slotline Annular Ring Elements and Their Applications to Resonator, Filter and Coupler Designs," IEEE Trans. On Microwave Theory and Techniques, VOL. 41, NO. 9, SEPTEMBER 1993.

[10]   Nagendra P. Pathak, "Integration of NRD Guide and Slot Line for Millimeter Wave Indoor Wireless Applications," Proceedings of WFMN07, Chemnitz, Germany.

[11]   Wen-Xun Zhang, "Modified Tapered Slot-line Antennas for Special   Applications,"   REV   Journal   on   Electronics   and Communications, Vol. 2, No. 3–4, July – December, 2012.

[12]   He Liquan, Wu Xidong, Zhu Xiaowei, "Fin-line Pin diode BPSK and QPSK modulators," Waves, February 1993, Volume 14, Issue 2, pp 355-361.

[13]   G Hammer, S Wuensch, M Roesch, K Ilin, E Crocoll and M Siegel, "Superconducting coplanar waveguide resonators for detector   applications,"   Superconductor   Science   and Technology Volume   20 Number   11**,**G   Hammer *et al* 2007 *Supercond.Sci.Technol.* **20** S408 doi:10.1088/0953-2048/2 0/11/S21.

[14]   Rainee N. Simons, NASA Glenn Research Center, Cleveland, Ohio, "Coplanar Waveguide Circuits, Components and Systems".

[15]   G.C. Dalman , "New waveguide-to-coplanar waveguide transition for centimeter and millimeter wave applications," Electronics Letters, Volume 26, Issue 13, 21 June 1990, p. 830 – 831,DOI: 10.1049/el:19900544 , Print   ISSN 0013-5194, Online ISSN 1350-911X.

[16] Mihai ŞOVA, Ion BOGDAN, "Coplanar Waveguide Resonator Design for Array Antenna Applications," Mikrotalasna revija, December 2003.

[17]   A. Penirschke†, A. Angelovski, R. Jakoby,Institut f ¨ur Mikrowellentechnik und Photonik, TU Darmstadt, Germany, Sydlo, U. Mavric, C. Gerth, S. Vilcins-Czvitkovits, D. Noelle DESY, Hamburg, Germany, "GROUNDED COPLANARWAVEGUIDE TRANSMISSION LINES ASPICKUPS FOR BEAM POSITION MONITORING IN PARTICLE ACCELERATORS,"TUPC29, Proceedings of IBIC2013, Oxford, UK.

[18] Image citations: www.embedded.com, www. analog.com, www. RF Wireless World.com.

Power amplification characteristics of ultrafast pulses after the NPR port of Yb-doped fiber laser in all normal dispersion configuration

Pradeep K. Gupta, C. P. Singh, A. J. Singh, S. K. Sharma, P. K. Mukhopadhyay, K. S. Bindra and S. M. Oak

Solid State Laser Division

Raja Ramanna Centre for Advanced
Technology Indore, India-452013
pkm@rrcat.gov.in

Abstract—The power amplification characteristics of all-fiber Yb-doped double clad fiber amplifier seeded by the pulses extracted after the nonlinear polarization rejection (NPR) port of all-normal dispersion (ANDi) mode-locked Yb-doped fiber oscillator is reported. 21.8 W of amplified average power at 37 MHz repetition rate was obtained at pump power of 35 W corresponding to ~62% pump to signal power conversion efficiency. The single pulse energy of the amplified mode locked pulses was ~590 nJ. The effect of pre-amplifier signal strength on temporal and spectral profiles of amplified pulses were investigated experimentally. It was found that though stronger signal strength at the input of the power amplifier is useful to increase the threshold for onset of amplified spontaneous emission (ASE), however, it may lead to severe distortion in temporal profile after compression due to enhanced nonlinearity. We conclude that there is an optimum signal strength for generation of clean and smooth ultrashort pulses with low ASE contribution with in the operating range of the power amplifier. The compressed pulse duration of the amplified pulses was measured to be 280 fs.

Keywords—All normal dispersion, mode locked, fiber amplifier, Yb-doped fiber laser.

I. Introduction

Ytterbium (Yb) doped mode-locked fiber laser in all normal dispersion (ANDi) configuration has attracted a great deal of current interest due to its simplicity in construction and configurability with all-fiber integration. Further, the shape of the mode-locked pulses from the ANDi laser is dissipative soliton type which can tolerate a large variation of gain and loss and hence highly suitable for energy scaling in external amplifier. Since its first demonstration in 2006 [1], considerable progress has been made during the recent past to understand the pulse shaping dynamics in ANDi laser as well as to improve its performance [2-4]. However, the pulses from most of these systems exhibit large amount of side-lobes when they are compressed to femtosecond duration and the pulse quality degrades further on amplification [5]. One of the reasons for poor pulse quality from the ANDi laser is that in most of the systems the output is taken either before or at the nonlinear polarization rejection (NPR) port in order to extract maximum pulse energy, though, the influence of nonlinearity

like self phase modulation (SPM) on the spectra of the pulses is very strong at those locations. Recently, we have shown that by extracting the pulses after the nonlinear polarization rejection port in ANDi Yb-doped fiber laser can provide a clean seed source which is considerably resistant to distortion on amplification as compared to that from the NPR-port and can be compressed into femtosecond regime without any significant side-lobes in the pulse profile [6]. It would be interesting to study the high power amplification characteristics of such mode locked pulses.
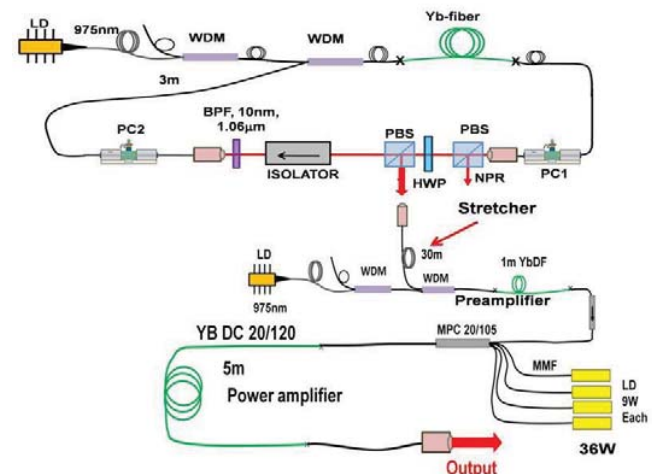
Figure 1: All-normal dispersion Yb-doped mode locked fiber oscillator-amplifier set-up.

In this paper, we report power amplification of pulses extracted after the NPR port of the mode locked Yb-doped ANDi laser. Mode locked pulses were amplified into Yb-doped double clad fiber (Yb DCF) amplifier. Around 21.8 W average amplified signal power with 35 W coupled pump power was obtained at fundamental repetition rate of 37 MHz. Spectral and temporal characterization of the power amplifier output was carried out for different input signal strength. In general, larger signal strength is desirable for power amplification to keep the ASE contribution low. However, strong signal strength leads to severely distorted pulse profile

due to increased nonlinearity. We found an optimum signal strength for clean and smooth compressed pulses while keeping low ASE contribution.

II. ALL NORMAL DISPERSION YTTERBIUM DOPED FIBER OSCILLATOR: GENERATION OF CLEAN PULSES

The construction of the ANDi Yb-doped fiber laser is shown schematically in Fig.1. The oscillator is comprised of a 70 cm long single clad single mode Yb-doped fiber (YbDF) with mode field diameter of 6.0 μm. It was pumped in-core by a single mode fiber (SMF) coupled laser diode (LD) at 976 nm with the help of a 980/1060 WDM combiner.
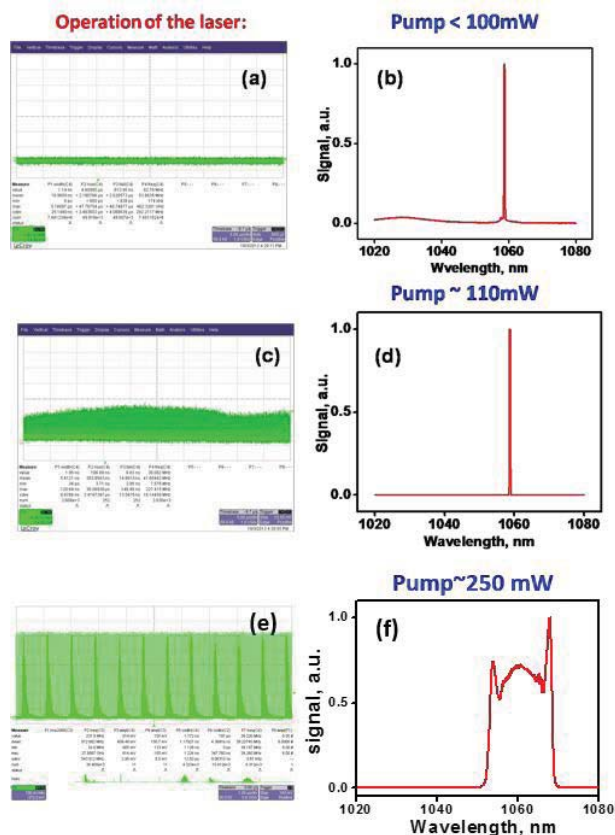
Figure2. Oscilloscope traces (a, c & e) and laser spectrum (b, d & f) in CW, QML & cwML regime respectively.

The maximum pump power delivered in the core of the YbDF was ~330 mW. One end of the YbDF was spliced to the output port of the WDM and at the other end; a standard SMF (HI1060, 105 cm long) was connected. At the signal port of the WDM a 300cm long SMF was spliced. The free ends of the two SMFs are connected to in-fiber collimators (COL1 and COL2). The total cavity length including the free space between the collimators was ~570 cm. A polarizing beam splitter (PBS1) is placed near COL1. The PBS1 in combination with the two in-fiber polarization controllers (PC1 and PC2) attached to the SMFs acts as the fast saturable absorber based on nonlinear polarization rotation. A fraction of the circulating power is coupled out from the cavity at PBS1 as the nonlinear

polarization rejection. An output (OP) coupler is implemented after the PBS1 with the help of a half wave plate (HWP) and a polarizing beam splitter (PBS2). The polarization transmission axes of PBS1 and PBS2 are kept parallel to each other and by adjusting the orientation of the c-axis of the HWP with respect to the PBSs the output coupling ratio from the OP port can be varied for a wide range. For example when the c-axis of HWP is kept parallel to the polarization transmission direction of the beam splitters no output occurs through the OP port and the NPR port acts as the only output port for the laser, while orienting it at some other angle output also occurs through the OP port. In our experiment the c-axis of the HWP was oriented to ~15^0 with respect to the polarization transmission direction of the beam splitter which was found optimum for extracting the maximum pulse energy through the OP port. A bulk optical isolator (ISO) was placed in the free space for unidirectional ring cavity operation and a narrow band interference filter (BPF) with 10 nm bandwidth and peak transmission at 1060 nm is placed after the isolator for self starting and stable mode-locking operation with a central wavelength around 1060 nm. The net dispersion in the oscillator was estimated to be ~0.12 ps^2. The laser can be easily mode-locked by adjusting the PC1 and PC2 and output can be taken either through the NPR port or OP port by orienting the c-axis of the HWP parallel or at 15^0 to the

polarization transmission direction of the PBSs. We denote **these two configurations of the laser as the 'NPR port setup' and 'OP port setup' respectively.** In the OP port setup when HWP is oriented at 15^0 to maximize the output from this port leakage signal from NPR port is also measured for comparison.

The evolution of mode locking in the oscillator segment is shown in Fig.2. The laser had a threshold ~70mW and operates in continuous wave (CW) mode upto ~100mW pump power. Fig. 2a and 2b show the oscilloscope trace for CW operation and the corresponding lasing spectrum respectively. On increasing the pump power, the laser operates in Q-switched mode-locking (QML) regime. Fig. 2c and 2d show typical oscilloscope trace and spectrum of the QML lasing regime. However, when the pump power is increased beyond 240 mW stable self-starting continuous wave mode locking (cwML) is achieved and a stable train of mode-locked pulses with a repetition rate of 37 MHz is observed as shown in Fig. 2(e). As a signature of ultrashort pulses, the spectrum of the cwML pulses becomes broad as depicted in Fig. 2(f). The operational characteristics of the

ANDi oscillator is described in Fig. 3. Fig. 3(a) shows the variation of the output p**ower from the 'NPR port setup'** and the corresponding mode-locking regimes as a function of the pump power. Since CW operation is observed over a very short pump power above threshold, it is not mentioned in Fig.3a. It can be seen from Fig.3 (a) that the laser operates in the QML regime until the pump power is below 240mW. However, when the pump power is increased beyond 240 mW stable self-starting continuous wave mode locking (cwML) is achieved and a stable train of mode-locked pulses with a repetition rate of 37 MHz is observed. A maximum average power of 90 mW was obtained at pump power of 300 mW corresponding to pulse energy of ~2.4nJ. The corresponding spectral profile of the mode-locked

pulses was recorded with the help of an optical spectrum analyzer (Agilent 86142B) and is shown in Fig. 3(b). It can be seen that the spectra is the usual hare-head shaped [3] with large peaks at the edges. The root mean square (rms) spectral width ($\Delta\lambda_{rms}$) was measured to be ~5.54 nm. It is to be noted from
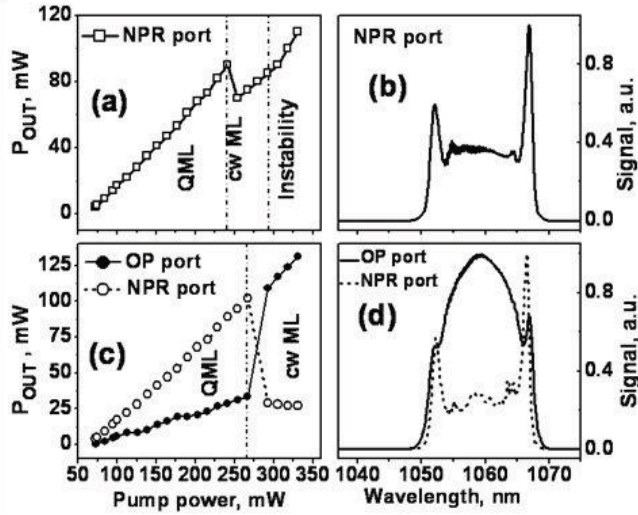
Figure.3.(a) and (b): operational and spectral characteristics of **the oscillator in 'NPR port setup'**,(c) and (d): **operational and spectral characteristics of the oscillator in 'OP port setup'.**

Fig.3(a) that as the pump power is increased beyond 300 mW, instability in the mode-locked pulses takes place and stable cw mode locking could not be obtained. The performance of the **laser in 'OP port setup' is shown in Fig.**3(c) and (d). The solid circles in Fig.3(c) shows the variation of the output power from the OP port as a function of the pump power. The power leaking-out through the NPR port in this setup is also shown in the same figure (open circles). It can be seen from Fig. 3(c) that the threshold for cw mode-locking is increased slightly (~270mW) due to the coupling loss of the OP port and most of the output occurs through the NPR port in the QML regime. However in cwML regime there is a sudden increase in the power through the OP port and the output power through the NPR port is reduced drastically. The laser was in stable cwML regime even at the maximum operating pump power of 330 mW delivering ~130 mW of average power. This corresponds to 3.5 nJ of pulse energy which is around 45% higher than that **obtained from the 'NPR port setup'.** The solid line in Fig. 3(d) shows the spectral profile of the mode locked pulses through the OP port. It can be seen that the spectra is smooth and dome shaped with considerably diminished peaks at the edges. The rms spectral width was measured to be ~ 4.8 nm. The dashed line in the figure shows the spectra of the pulses leaking through the NPR port which is qualitatively similar in shape to Fig. 3(b) with a nearly same spectral width ($\Delta\lambda_{rms}$ ~5.55 nm).

Pulses from the oscillator are highly chirped with a measured duration of 5 ps. Around 10 mW of signal from the OP port was coupled to the stretcher fiber. The stretcher is made of 30 m long SMF which increases the pulses duration to around 30 ps. The pre-amplifier setup consists of a 1 m long

Yb doped SMF pumped in-core (400mW, 976nm) by a fiber coupled LD. A small scale amplification characteristics of the mode locked pulses obtained from the OP- and NPR-port have been studied into single clad single mode YbDF amplifier [6]. It was found that in contrast to NPR-port, the spectra of the pulses from the OP port is considerably resistant to distortions on amplification and can be compressed in the femtosecond regime (156 fs) without any significant side-lobes and hence can serve as an excellent seed source for further power amplification. Therefore, we have used seed signal only from OP-port for power amplification.

III. POWER AMPLIFICATION OF ULTRASHORT LASER PULSES

Power amplifier segment is designed based on prior simulations incorporating the interplay of seed signal strength, pump power, amplifier fiber length and the peak ASE power in ultrafast Yb DCF amplifier using a commercial simulation software [9]. An optimum choice of parameters for negligible ASE contribution is obtained. We have considered the amplification of signal power at 1060 nm co-propagating with the pump wavelength at 975 nm in the Yb-doped fiber. The growth of ASE, for each direction of propagation and their back-action on the local excited-state population due to wavelength-selective amplification and reabsorption can be modeled by the following rate equations involving the population inversion density N_2 (z), the pump field $P(z)$, the signal field $P_s(z)$ and the ASE P_f (z) at a given longitudinal position z along the fiber under the assumption of purely homogeneous broadening as [7]:

$$\frac{dP(z)}{dz} = -\eta_p \sigma_{ap} P(z)\left[N_{tot} - (1+\delta)N_2(z)\right] \quad (1)$$

$$\frac{dP_s(z,\nu_s)}{dz} = \eta_s \sigma_{es}(\nu_s) P_s(z,\nu_s)\left[(1+\alpha(\nu_s))N_2(z) - \alpha(\nu_s)N_{tot}\right] \quad (2)$$

$$\frac{dP_f^\pm(z,\nu)}{dz} = \pm\eta_s \sigma_e(\nu)\left[P_f^\pm(z,\nu)[(1+\alpha(\nu))N_2(z) - \alpha(\nu)N_{tot}] + h\nu\delta\nu N_2(z)\right] \quad (3)$$

Here, η_p and η_s are the overlapping factors of the pump and signal respectively within the fiber core, $P(z)$ is the power of the pump, P_s *(z, ν)* is the power spectral density of the injected co-propagating signal and $P_f^\pm$ *(z, ν)* is that for the co-propagating and counter-propagating ASE. N_{tot} is the dopant concentration, $N_2(z)$ is the metastable level density population. σ_{ap} and $\sigma_{ep}(\nu_p)$ are the pump absorption and stimulated emission cross section. $\delta = \sigma_{ep}(\nu_p)/\sigma_{ap}$ is the ratio between the stimulated emission and absorption cross section at the pump wavelength, and $\alpha(\nu_s) = \sigma_{as}(\nu_s)/\sigma_{es}(\nu_s)$ is the ratio between the cross section of the signal absorption and stimulated emission. $\alpha(\nu_s) = 1$ for an ideal three-level system, and 0 for a pure four-level scheme. α (ν) and σ_e (ν) are the same for the ASE wavelength. In the ASE power expression, the factor $h\nu\delta\nu$ is the noise power corresponding to one photon per mode in

bandwidth δv; if the two polarizations can can be propagated in the fiber, the noise power becomes $2hv\delta v$.

Eqs (1)-(3) are solved numerically using a commercial simulation software [8] for following parameters: core diameter = 20 μm, inner cladding diameter =125μm, N_{tot} = 8.5 10 m , $_{ap}$ = 25 10 μm , $_{ep}$ = 21.7 10 μm , $_{as}$ = 0.448 10 μm , $_{es}$ = 2.62 10 μm and = 0.8 ms. The simulation results are summarized in Fig.4. Fig. 4(a) shows the computed interdependence of signal strength, output power and pump power for a fixed gain fiber length whereas Fig. 4(b) shows the interdependence of signal strength, output power and length of gain fiber for a fixed pump power. Thus Fig.4 provides a guide line for selecting optimum length of the gain fiber depending on the available pump power and signal strength to obtain maximum amplified power with low ASE contribution. Figure 4 shows the simulation results for a wide range of input signal strengths for less than 1% ASE contribution. It can be seen from Fig. 4(a) that the signal strength should be increased proportionally with the pump power in order to obtain maximum output power with minimum ASE signal for a fixed fiber length of 2 m. Optimum length of the gain fiber required for a given signal strength at a fixed pump power of 40W is shown in Fig. 4 (b). It can be seen that lower signal strength requires longer gain fiber to obtain the maximum output power with low ASE content.
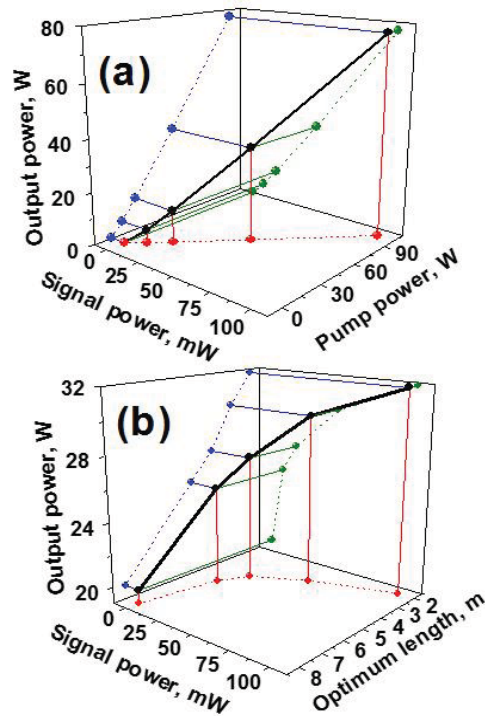
Figure 4: (a) Interdependence of the signal, pump and output power for low (<1%) ASE contribution for a fixed fiber length of 2m (b) Interdependence of optimum fiber length, signal strength and amplified power with less than 1% ASE at a fixed pump power of 40W.

Power amplifier is designed in the lab based on the simulation results. The power amplifier segment is shown in Fig. (1). It is comprised of a (6+1) x1 multiple pump combiner (MPC) with signal feed through, a Yb-doped doubled clad fiber with 20 μm core diameter and 125 μ m inner clad diameter (YDF-20/130-VIII, Nufern) and 4-nos of high power multimode fiber (core diameter 105μm, N.A. 0.15) coupled laser diodes at 976nm with 9W of output power each. The MPC combines the pump beam from the high power laser diodes for cladding pumping of YbDCF and the signal from the preamplifier (via an isolator) to the core of the YbDCF for power amplification. Considering the insertion losses from isolator and MPC the signal strength coupled to the power amplifier can be varied in the range of 5 mW – 60 mW by varying the preamplifier gain. The length of the YbDCF is kept fixed ~5 m for complete absorption of the pump beam and the signal strength is adjusted to obtain low ASE contribution and clean temporal profile of the amplified pulses.
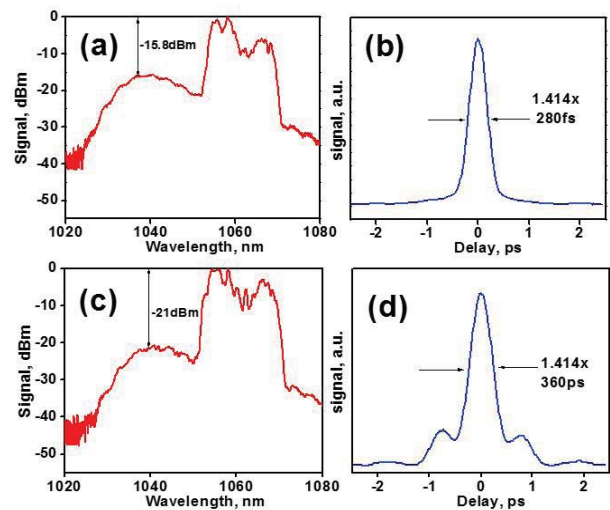
Figure 5: Optical spectrum and autocorrelation traces of power amplifier at (a) 7 mW and (b) 30 mW input signal strength.

Total 35 W of pump power is coupled to the inner clad of Yb DCF. The other end of Yb DCF was spliced with a high power fiber pigtailed collimator. The amplified signal was sent to the grating compressor. The compressor consists of a pair of gratings (groove density: 600 lines/mm) and a broad band retroreflector arranged in near littrow configuration. The overall compression efficiency of the grating pair was found to be ~55%. A part of the amplifier output was used to monitor the spectrum of the mode locked pulses.

In order to find the optimum signal strength, we first recorded the characteristics of the amplified pulses at a fixed pump power of ~15W with varying signal strength. It is observed that with increase in the input signal strength ASE contribution reduces whereas, in the time domain from the autocorrelation (AC) measurements it was found that the pulse gets distorted. Optical spectrum and AC traces of amplified

pulses after the compression at two representative input signal strengths are shown in Fig 5. At low input signal strength (~7 mW), the ASE peak is ~16 dBm below the signal peak as shown in Fig. 5(a). In the linear scale ASE to signal peak is ~3 %. The AC shows smooth and clean profile with FWHM ~396 fs which corresponds to ~280 fs pulse duration assuming a Gaussian pulse profile as shown in Fig. 5 (b). With increase in the input signal strength to ~ 30 mW, the ASE peak is ~21 dBm below the signal peak. In the linear scale ASE to signal peak is below 1%. In the temporal domain, the pulse no longer remains clean and smooth as evident from the AC trace shown in Fig. 5(d) with an estimated pulse duration of 360fs.

Although, increasing the input signal strength to the power amplifier reduces the contribution from ASE, the signal enhancement in the pre-amplifier becomes practically disadvantageous due to strong SPM induced nonlinearity. Since grating pair compensates only the linear chirp, the residual nonlinear chirp distorts the pulse profile and results in enhanced pulse duration as well. Nonlinearity in the preamplifier is more significant as it consists of SMF (core diameter is small ~6 μm). Thus, the signal strength in the preamplifier should be managed in such a way that it feeds the power amplifier sufficiently to keep ASE below 1% of the amplified signal and simultaneously maintaining small SPM induced nonlinearity. Based on our measurement we found that an optimum input signal strength of 10 mW to get clean and smooth pulses from the power amplifier and at the same time keeping the ASE contribution low.
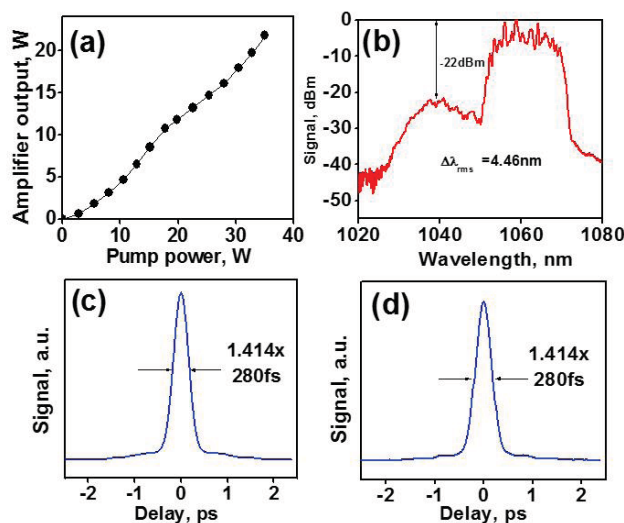
Figure 6: (a) Variation of amplifier output power with pump power coupled in Yb DCF. (b) Spectral profile of mode locked pulse after power amplification, (c) and (d) AC trace of the compressed amplified pulses at 1 W and 30 W pump power respectively.

Figure 6 shows the power amplification characteristics in Yb DCF amplifier with the optimum input signal strength. The amplified average power scales up almost linearly with the pump power. The variation of amplified

power with the pump power is shown in Fig. 6(a). At the maximum coupled pump power of 35 W, amplified signal power was measured to be 21.8 W corresponding to single pulse energy of ~590 nJ. The pump to signal power conversion efficiency was found to be ~62%. The recorded spectral profile of the mode locked pulses after power amplification is shown in Fig. 6(b). It can be seen that there is no significant contribution from amplified spontaneous emission and the rms spectral width was calculated to be 4.46 nm. Figure 6(c) and 6(d) show the AC traces of the amplified pulses after compression into grating pair at low and high pump powers. It can be seen that there is no appreciable change in the pulse shape and duration with increase in the pump power. The temporal profile is significantly smooth and free from any side lobes with a measured pulse duration of 280 fs (assuming a Gaussian pulse shape). It is interesting to note that with optimum input signal strength the spectral and temporal profile of the pulses remain unaffected by the power amplification process within the operating range of the pump power.

IV. CONCLUSION

In conclusion, we have studied the power amplification characteristics of all-fiber Yb-doped double clad fiber amplifier seeded by the pulses extracted after the NPR port of ANDi mode-locked Yb-doped fiber oscillator. 21.8 W of amplified average power at 37 MHz repetition rate was obtained at pump power of 35 W corresponding to ~62% pump to signal power conversion efficiency. The single pulse energy of the amplified mode locked pulses was ~590 nJ. The effect of pre-amplifier signal strength on temporal and spectral profiles of amplified pulses were investigated experimentally. It was found that though stronger signal strength at the input of the power amplifier is useful to increase the threshold for onset of amplified spontaneous emission (ASE), however, it may lead to severe distortion in temporal profile after compression due to enhanced nonlinearity. We conclude that there is an optimum signal strength for generation of clean and smooth ultrashort pulses with low ASE contribution with in the operating range of the power amplifier. The compressed pulse duration of the amplified pulses was measured to be 280 fs.

References

[1]. A. Chong, J. Buckley, **W. Renninger and F. Wise, "All-**normal-**dispersion femtosecond fiber laser," Opt. Exp., 14(21),** 10095-10100, 2006.
[2]. A. Chong, W. Renninger and F. Wise, "All normal dispersion femtosecond fiber laser with pulse energy above **20nJ," Opt. Lett. 32(16), 24**08-10, 2007.
[3]. A. Chong, W. Renninger and F. Wise, J. Opt. Soc. Am. B. 25, 140 (2008).
[4]**. K. Kiew, W. Renninger, A. Chong and F. Wise, "Sub** 100fs pulses at Watt level powers from a dissipative soliton **fiber laser," Opt. Lett. 34(5), 593**-95, 2009.

[5]. **P. K. Mukhopadhyay, K. Özgören, İ. L. Budunoğlu, F. Ö. İlday, "All**-fiber low-noise high-power femtosecond Yb-fiber amplifier system seeded by an all-normal dispersion fiber **oscillator," IEEE J. Sel. Top. Quant. 15(1), 145**-152, 2009.

[6]. P. K. Mukhopadhyay, P. K. Gupta, K. S. Bindra, and S. **M. Oak, "Note: Amplification characteristics of all**-normal-dispersion mode-locked Yb -doped fiber laser: Influence of **input pulse shape," Rev. Sci. Instrum. 84, 076107, 2013.**

[7]. H. CoIc, **"**Analytic modelling of high-gain ytterbium-doped fibre amplifiers**,"** J. Opt.A 4(2), 120-129, 2002.

[8]. Trial version of the simulation software is available at www.liekki.com

Reconfigurable Surface Design for Electromagnetic Wave Control

Fereshteh. Samadi, and Abdelrazik. Sebak

Electrical and Computer Department, Concordia University, Montreal, Quebec H3G 1M8, Canada

F_samadi@encs.concordia.ca, abdo@ece.concorida.ca

Abstract— **A reconfigurable surface, for electromagnetic (EM) wave manipulation, utilizing frequency selective unit-cells integrated with PIN diodes are introduced. By digitally controlling the reconfigurable surface, several functionalities such as focusing, linear polarization conversion and scattering are obtained on the same surface. For the scattering purposes, three arrangement methods of alternative periodic columns, chessboard-like structure and coding surface optimized by GSO algorithm are analyzed. For the coded surface, 10-dB RCS reduction from 15.5 GHz to 22.5 GHz is obtained with a bandwidth of 37%. All the results show that the introduced reconfigurable surface has more potential for future applications.**

Keywords—Active frequency selective surface (FSS), reconfigurable surface, scattering, polarization conversion, security building, focusing.

I. INTRODUCTION

Frequency selective surfaces (FSSs), normally consist of artificially periodic or quasi-periodic structures, which provide several design strategies for various functionalities. They have been applied in several applications such as reducing interference [1], minimizing radar cross section (RCS) [2] and shielding [3] to name a few. Most of the conventional designs were focused on a certain function where the EM wave manipulation was fixed for the designed prototype. Therefore, conventional FSSs showed a limitation when employed to modern multifunctional and complex systems. To address this problem, a large amount of studies has been devoted to developing tunable FSS whose operation status can be controlled and subsequently, flexible functionalities can be achieved. The ability to electrically tune or alter the functionality of a surface has been realized through loading with active semiconductor devices, such as varactors and PIN diodes. They have been employed in several practical applications like reconfigurable antennas [4], designing intelligent walls [5]- [9] and radomes [10], [11]. Nowadays, one of the appealing applications of reconfigurable surfaces is a programmable wireless environment [12]. In this application, electromagnetic (EM) waves can be effectively engineered for several purposes including steering toward any desired direction, scattering, polarization manipulation and more.

In this paper, we present a tunable surface for multi-functional applications such as programmable wireless environment, see Fig. 1. The proposed surface is constructed

of active unit-cells loaded by PIN diodes. Since each unit-cell can be controlled independently, the surface has ability to digitally control EM waves for versatile functions such as scattering, focusing, steering and polarization conversion. For the scattering purposes, $180° \pm 37°$ [13] reflection phase difference between ON and OFF states of the unit-cells in a frequency range of 16.25 GHz to 22.75 GHz is realized. To find the optimal ON and OFF states of the unit-cells, optimization algorithm of group search optimization (GSO) is applied, where very low RCS with a bandwidth of 37% (frequency range between 15.5 GHz to 22.5 GHz) is achieved. Other functionalities are also proved through simulations which clearly shows the applicability of the proposed work for multi-functional systems such as the aforementioned programmable wireless environment.
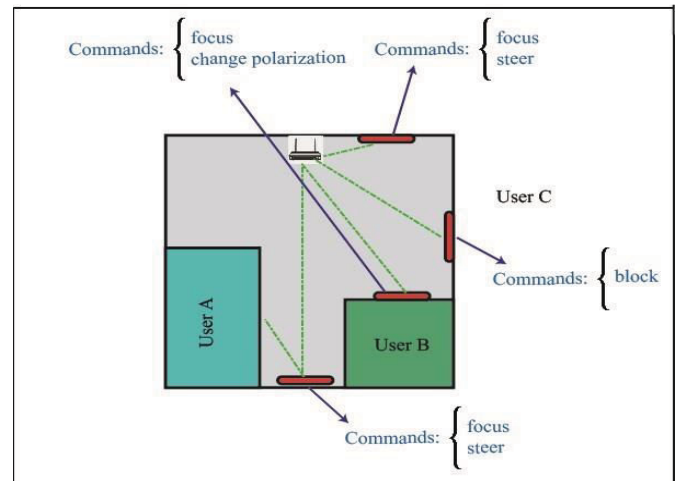
Fig. 1. Programmable wireless environment with an example of commands to manipulate EM waves to match the requirements of users.

II. ACTIVE FSS DESIGN

The geometrical configuration of the proposed multi-functional FSS unit-cell is depicted in Fig. 2 (a,b). The patch is mounted on Arlon diclad 880, with permittivity of 2.2 and thickness of 1.542 mm. To have reflection type unit-cell, a uniform ground plane is selected. In addition MACOM MADP-000907–14020 PIN diode is loaded on the

top to connect the patch to the ground plane through a metal via. The PIN diode is modeled as equivalent series resistance and inductance of 7.8 Ω and 30 pH, when the diode is ON, and series capacitance and inductance 7.8 Ω and 28 pF, when it is OFF, see Fig. 2, (c). The reflection phases for both ON and OFF conditions are investigated through HFSS software and shown in Fig. 3. The reflection phase difference between ON and OFF conditions is also shown in Fig. 3. Considering Fig. 3, the $180° \pm 37°$ [13] reflection phase difference is ranging from 16.25 GHz to 22.75 GHz, with a 33% frequency bandwidth, which is quite wide for active FSS unit-cell.
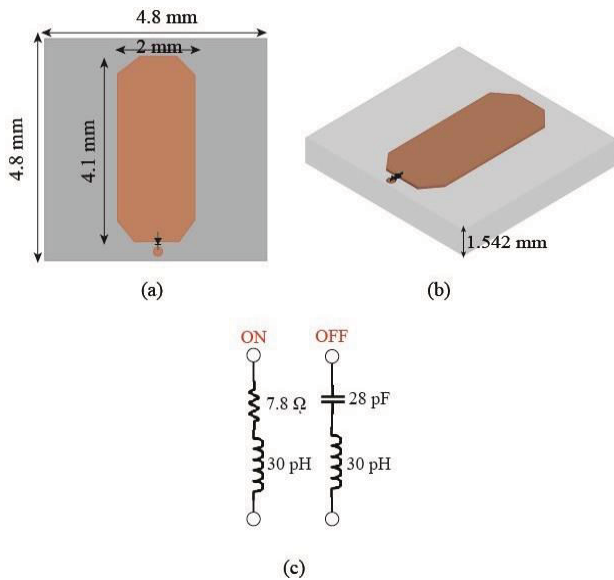
Fig. 2. Geometrical configuration of proposed active FSS unit-cell loaded by PIN diode. (a) Front view, (b) Side view, (c) The equivalent circuit of PIN diode.
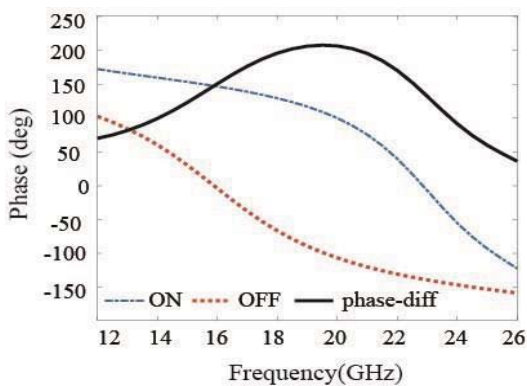
Fig. 3. Reflection phase coefficient, ON state, OFF state and the phase difference between two states.

III. RESULTS FOR MULTIPLE FUNCTIONALTIES

After designing the unit-cell, in order to satisfy periodicity 4 × 4 unit-cells are considered as a tile. The ON and OFF states are mimicked as 1 and 0 digits. The overall dimension of 192 mm × 192 mm consisting of 10 × 10 tiles are used. The multi-functionality is achieved by simply varying 0 and 1, i.e.,

changing ON and OFF states of the tiles. We will investigate every functionalitiy in the following section.

A. Linear Polarization Conversion

Linear polarization conversion can be attained when all the unit-cells in the surface work at ON or OFF states simultaneously, which means all '1' or '0' coding matrices. In order to analyze the polarization conversion efficiency, the surface is illuminated by a diagonal plane wave, as it is shown in Fig. 4(a). The cross-and co-reflection amplitudes are simulated using HFSS software. As it can be seen from Fig. 4 (b), in the frequency range of 12 GHz to 21 GHz, the cross-reflected amplitude is around 0 dB, however; the co-one is very low around -10 dB with a peak of -35 dB. This shows the ability of the structure to rotate the polarization.
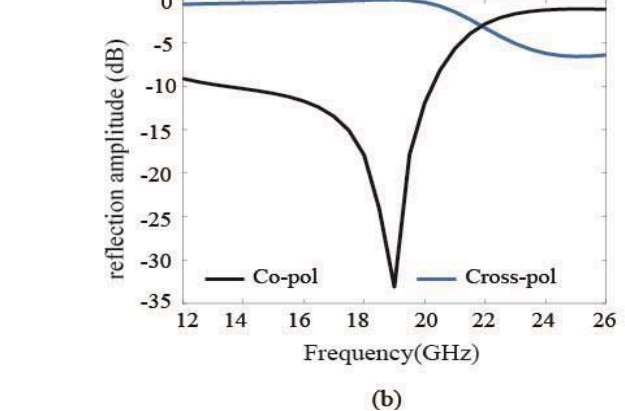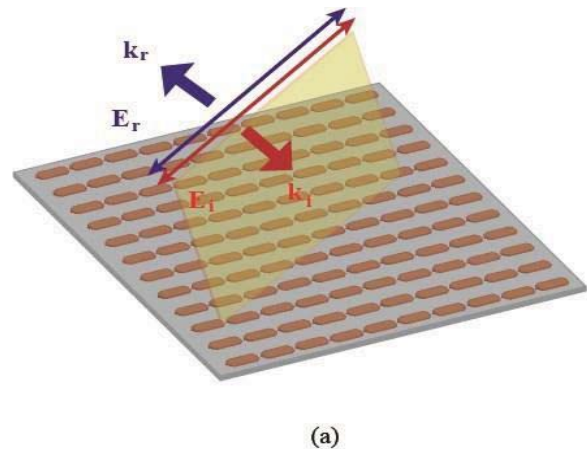
Fig. 4. Linear polarization conversion. (a) Schematic view of surface illuminated by diagonal plane wave, (b) Simulated co-and cross reflection amplitudes.

B. Focusing

When all unit-cells are OFF or ON, focusing properties can be achieved. Fig. 5 shows the reflected focused pattern from the surface when all diodes are ON. In this paper, the corresponding focused beam pointed at 0°, however; the pattern

can be steered in other directions as well, by adjusting phase wave-front.

(a)   (b)
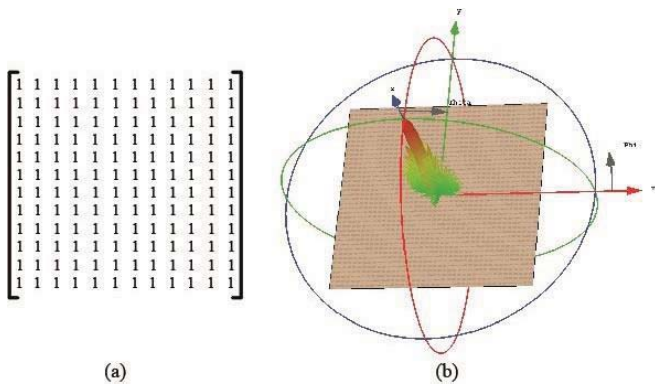
Fig. 5. Focusing properties for the case that all unit-cells are ON.

C. Scattering properties

Various scattering pattern can also be achieved when the surface is illuminated by a plane wave. To do so, several coding matrices are analyzed. Firstly, '1' and '0' tiles are arranged alternatively. This arrangement results in two main beams, see Fig. 6 (a,b). Afterward, a chess-board binary coding configuration shown in Fig. 6(c) is applied, and as it is expected four main lobes are achieved when illuminated by an incident plane wave. Finally, to attain a very uniform scattered pattern, the coding matrix is obtained applying GSO [14] optimization algorithm. Fig. 6 (e,f) depicts the optimal coding matrix and the scattered pattern from the optimal surface. As can be seen from the scattered pattern, very uniform pattern with the lowest maximum RCS is achieved for the coded surface. To further investigate the RCS reduction properties for the three designs, the monostatic normalized RCS is simulated and shown in Fig. 7. It worth mentioning that, the surfaces are normalized by the same size PEC plane. Comparing the RCS reduction curves in Fig. 7, it can be realized that the optimal surface contributes to the widest bandwidth and the lowest RCS reduction. The bandwidth for the coded surface is about 37%, ranging from 15.5 GHz to 22.5 GHz. This value is in agreement with the bandwidth of the reflection phase difference in Fig. 3, as it is expected.

IV. CONCLUSION

We presented a multifunctional reconfigurable structure with the bandwidth of 37% ranging from 15.5 GHz to 22.5 GHz. The proposed design switches between polarization convertor, scattering and focusing surface. The proposed FSS structure consists of 10 by 10 tiles, where by deliberately switching every tile the desired functionality is achieved. The powerful manipulating ability of the EM wave indicates that the proposed FSS structure has great promise for programmable wireless environments and intelligent walls.

(a)   (b)

(c)   (d)

(e)   (f)
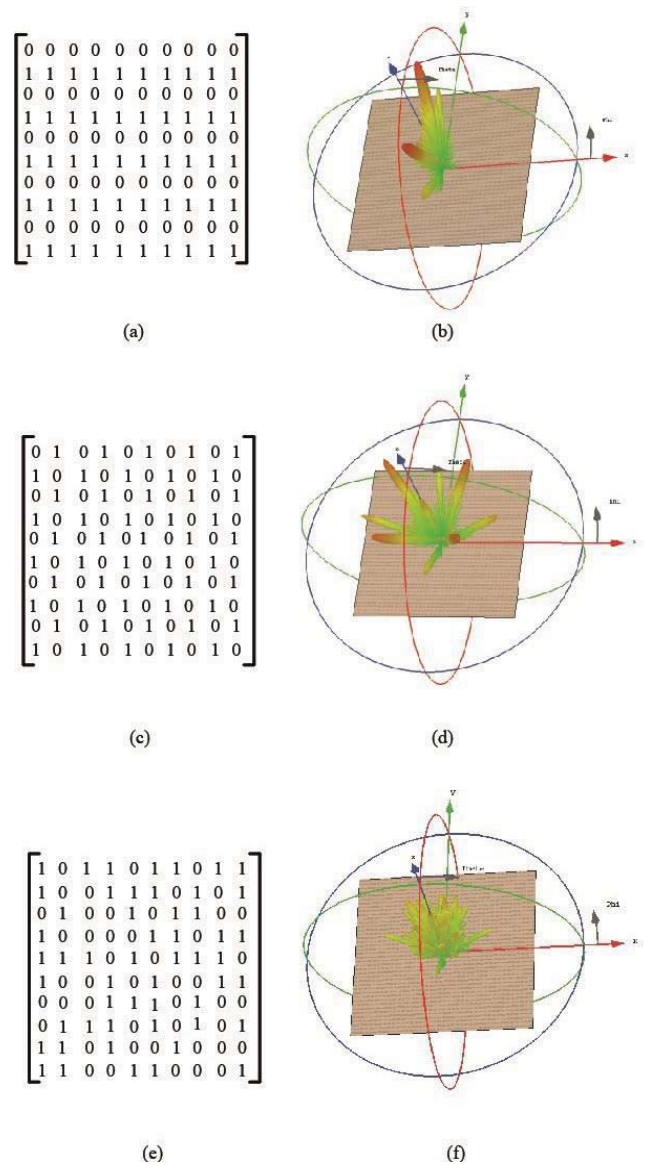
Fig. 6. Various scattering properties under normal incidence wave. (a,b) Alternative structure matrix and associated scattered pattern, (c,d) Chessboard-like structure matrix and associated scattered pattern, (e,f) coded structure matrix and associated scattered pattern.
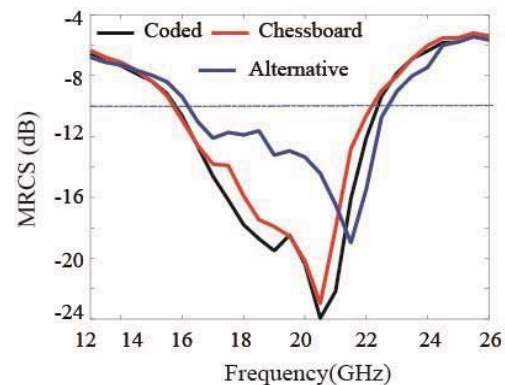
Fig. 7. Monostatic normalized RCS reduction.

REFERENCES

[1] M. Yan, S. Qu, J. Wang et al., "A miniaturized dual-band FSS with stable resonance frequencies of 2.4GHz/5GHz for WLAN applications," IEEE Antennas and Wireless Propagation Letters, vol. 13, pp. 895–898, 2014.

[2] C. Sudhendra, A. R. Madhu, A. C. R. Pillai, R. Kark, and T. S. Rukmini, "A novel ultra wide band radar absorber based on hexagonal resistive patch FSS," in *Proceedings of the 4th IEEE Applied Electromagnetics Conference, AEMC 2013*, pp. 1-2, December 2013.

[3] R. Sivasamy, M. Lingeshwaran, K. Malathi, S. Esther Florence, and A. M. Gulam Nabi, "A low-profile paper substrate-based dual-band FSS for GSM shielding," *IEEE T ELECTROMAGN C,* vol. 58, no. 2, 2016, pp. 611-614.

[4] Sanz-Izquierdo, B., Liang, B., Parker, E.A., et al., "An application of active frequency selective surface to reconfigurable antenna technology," Proc. Active and Passive RF Devices Seminar, London, UK, February 2016, pp. 1– 5.

[5] Subrt, L., Pechac, P.: "Intelligent walls as autonomous parts of smart indoor environments," IET Commun., 2012, 6, (8), pp. 1004–1010.

[6] Gustafsson, M., Karlsson, A., Pontes Rebelo, A.P., et al.: "Design of frequency selective windows for improved indoor outdoor communication," IEEE Trans. Antennas Propag., 2006, 54, (6), pp. 1897–1900.

[7] Ch. Liaskos, Sh. Nie, A. Tsioliaridou, A. Pitsillides, S. Ioannidis, and I. Akyildiz. "A new wireless communication paradigm through software-controlled metasurfaces." *IEEE Commun. Soc, vol.* 56, no. 9, pp. 162-169, 2018

[8] G. I.Kiani, K. L. Ford, L. G. Olsson, K. P. Esselle, and Ch. J. Panagamuwa. "Switchable frequency selective surface for reconfigurable electromagnetic architecture of buildings. " IEEE Trans. Antennas Propagat., vol.58, no. 2, pp. 581-584, 2009

[9] J. Roberts, J. M. Rigelsford, and K. L. Ford. "Diffraction from Frequency Selective Surfaces for secure building applications." In *2012 6th European Conference on Antennas and Propagation (EUCAP)*, pp. 2388-2391. IEEE, 2012.

[10] Weiwei, W., Xi, C., Qi, F., et al.: "A measured FSS radome with two absorptive bands separated by one passband," Proc. 11th European Conf. Antennas Propagation (EUCAP), Paris, France, 2017, pp. 1118–1121

[11] Sangeetha, B., Gulati, G., Nair, R.U., et al. "Design of airborne radome using Swastika-shaped metamaterial-element based FSS," Proc. IEEE Annual India Conf. (INDICON), Bangalore, India, December 2016, pp. 1–4.

[12] Ch. Liaskos, N. Shuai, T. Ageliki, P. Andreas Sotiris Ioannidis, and A. Ian "A new wireless communication paradigm through software-controlled metasurfaces," *IEEE Communications Magazine,* vol. 56, no. 9, 2018, pp.162-169.

[13] W. Chen, C. A. Balanis and C. R. Birtcher., "Checkerboard EBG Surfaces for Wideband Radar Cross Section Reduction, " IEEE Trans. Antennas Propagat., vol. 63, no. 6, pp. 2636-2645, 2015.

[14] F. Samadi, M. Akbari, M.R. Chaharmir, and A. Sebak., "Scatterer Surface Design for Wave Scattering Application," IEEE Trans. Antennas Propagat., vol. *67*, no. 2, pp.1202-1211, 2019.

On-Body Circular Patch Antenna for Breast Cancer Detection

Dhrubo Ahmad
Department of EEE
American International University-Bangladesh (AIUB)
Dhaka, Bangladesh
azizrifat2000@gmail.com

Abdul Aziz
Department of EEE
American International University-Bangladesh (AIUB)
Dhaka, Bangladesh
dhrubo23ahmad@gmail.com

Taslima Akter Shila
Department of EEE
American International University-Bangladesh (AIUB)
Dhaka, Bangladesh
taslima.shilaa@gmail.com

Sohel Rana
Department of EEE
American International University-Bangladesh (AIUB)
Dhaka, Bangladesh
sohelahmed.eee@gmail.com

Raja Rashidul Hasan
Department of EEE
American International University-Bangladesh (AIUB)
Dhaka, Bangladesh
hemalaiubeee@gmail.com

Md. Abdur Rahman
Department of EEE
American International University-Bangladesh (AIUB)
Dhaka, Bangladesh
arahman@aiub.edu

Abstract—**Breast Cancer is one of the deadliest forms of cancer faced by women every year. Despite having medical methods like Mammography, MRI and ultrasound available, they have various limitations due to poor tissue contrast. This results in misdiagnosis of breast cancer patients all over the world. The purpose of this paper is to detect the presence of breast cancer tumors in women by the variation of S_{11} parameter of a microstrip patch antenna. To reach the desired goal, a circular microstrip patch antenna has been designed in ISM band along with two types of breast phantoms in order to detect the presence of cancerous tumors. The antenna along with the breast phantoms have been created using CST design environment and its various parameters i.e. reflection coefficient, efficiency, SAR have been evaluated to reach the goal set by this paper.**

Keywords—*ISM band, Microstrip patch, Reflection coefficient, S_{11}, Frequency, Breast tissue, Breast phantom, Farfield, Efficiency, SAR*

I. INTRODUCTION

Breast cancer is one of the leading causes of death in women. It is one of the most widespread disease for women around the world. Now a days, a staggering number of women are being affected every year by breast cancer. Breast cancer can also lead to others serious complications in brain, lungs, liver or bones [1]. And so, to ensure critical, proper and effective treatment, early detection of tumors that leads to breast cancer is of utmost importance. To achieve this, locating the exact position and size of the tumor is necessary. Since in the early stage of breast cancer, the tumor remains very small, it is possible for microwave imaging to locate it

promptly and precisely.

At present, mammography is the go to method for detecting breast cancer in women. To detect the presence of breast cancer in women who have no apparent symptoms, screening mammograms are routinely administered. The size of the tumor ultimately decides the ability of a mammogram to detect breast cancer. The ability may depend on the breast tissue density, and the skill of the radiologist for reading, administering and performing the mammogram. If the patient is younger than 50 years, it is less likely that Mammography will reveal the presence of breast tumors. The reveal is more likely to happen in older women. This is due to the fact that younger women have denser breast tissue. Due to this, they might appear white in the diagnostic of a mammogram. As a tumor also appear white on a mammogram, this makes the tumor harder to detect in a mammogram [2].

Another method of diagnosing breast cancer is by biopsy [3]. Although biopsy is a really good method of screening breast cancer, there are still some viable issues. The amount of tissue extracted from a needle biopsy may not be sufficient and the biopsy may have to be repeated. Even after samples are extracted from the precise area, there is a possibility of false negative results occurring if the pathologist misdiagnoses the tissue as benign when in reality, cancer is indeed present. Although with surgical biopsy, this is less likely to happen. But even then a misdiagnosis can happen if the tissue of a wrong area is removed [4].

For this reason, recently, research has been going on regarding different types of antenna that uses microwave imaging technique to figure out the presence of a tumor. A patch antenna or microstrip patch antenna is a wide-beam, narrowband antenna. It is also known as printed antenna. Its physical geometry revolves around two dimensions. For fabrication of a patch antenna, on an insulating dielectric substrate like a PCB or printed circuit board, a shaped metal sheet is mounted. At the opposite side of the substrate, a continuous metal layer bonded which forms a ground plane [5]. These types of antenna can either be implantable or on-body. This antenna radiates a microwave signal to the breast and those signals detect the cancerous cells from breast.

In this paper, the proposed antenna was designed in CST Studio Suite (CST) and two types of breast phantom was created in order to simulate the results. From the results, it is seen that the presence of tumors at both of the breast phantoms were detectable.

This paper is presented as, in section II is the modelling of the antenna. In section III, design of the breast phantoms are included. Section IV consists of the simulated results. Lastly, the overall paper has been discussed in section V.

II. MODELLING OF THE ANTENNA

A microstrip patch antenna was designed which operates at ISM Band in order to detect the presence of cancerous tumors. ISM band works at the range of (2.4-2.48 GHz) [6]. The antenna is working at a resonant frequency of 2.885 GHz for Breast Phantom 1 and 2.3557 GHz for Breast Phantom 2. Copper has been used to create both the ground plane and the patch. To create the substrate, flexible material FR-4 has been used. CST Studio Suite has been used to design the antenna and human body phantom model.

The reason that copper was chosen was due to the fact that copper is an amazing conductive material and it is very efficient in terms of distributing electrical energy. Also, due to the fact that copper is relatively cheap [7]. FR-4 was chosen primarily because of its availability, high dielectric strength, resistance to moisture, cheap cost and its capability of delivering proper result in higher frequency [8].

TABLE I.   DETAILS OF COPPER MATERIAL

No	Copper Material	
	Characteristics	Value
01	Type	Lossy Metal
02	Mu	1
03	Electric Conductivity	5.96e+007 [S/M]
04	Rho	8930 [Kg/M^3]
05	Thermal Conductivity	401 [W/K/M]
06	Heat Capacity	0.39 [Kj/K/Kg]

No	Copper Material	
	Characteristics	Value
07	Diffusivity	0.000115141 [M^2/S]
08	Young's Modulus	120 [Kn/Mm^2]
09	Poisson's Ratio	0.33
10	Thermal Expansion	17 [1e-6/K]

TABLE II.   DETAILS OF FR-4 MATERIAL

No	FR-4 Material	
	Characteristics	Value
01	Type	Normal
02	Mu	1
03	Epsilon	4.3
04	Electric Tan.	0.025 (Const. Fit)
05	Thermal Conductivity	0.3 [W/K/M]

Using all the electrical parameters stated above, the final antenna design was created. The dimension of the antenna was measured to be $48.46 \times 42.46 \times 1.6$ mm^3.
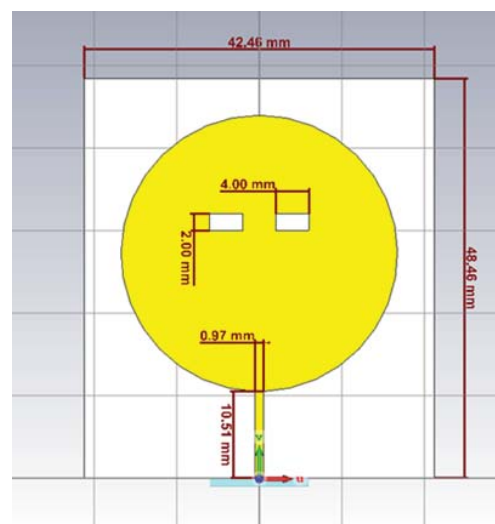
Fig. 1. Dimension of the Created Antenna

TABLE III.   DIMENSION OF THE CREATED ANTENNA

No	Dimension	
	Name of the Parameter	Size (mm)
01	Total Length	48.46
02	Total Width	42.46
03	Radius of Patch(a)	16.73
04	Thickness of Patch (yp)	0.035
05	Line Width (ls)	0.97
06	Line Length (ps)	10.5
07	Patch Distance (wg)	4.5
08	Substrate Height (ts)	1.6

After simulating the antenna in free space, 2.465 GHz was found to be the operating frequency with a reflection co-efficient of -31.923577 dB as seen from figure 2.
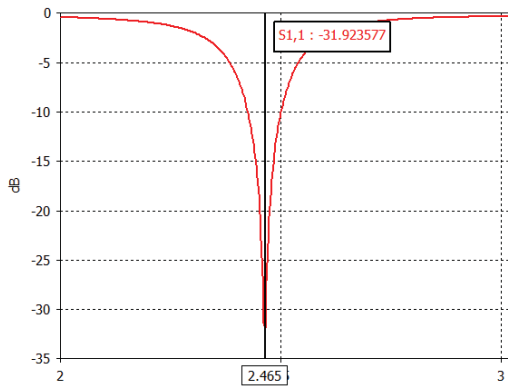
Fig. 2. S_{11} of the Antenna in Free Space

III. DESIGN OF THE BREAST PHANTOMS

In order to simulate our antenna, at first a breast phantom had to be made with the necessary parameter values. For this, skin and breast tissue were used.

The parameter used to create the skin of the breast phantom was as below:

Disp. Eps. = Nth order model (fit): N=3
Mue = 1
Rho = 1100 [kg/m^3]
Thermal Conductivity = 0.293 [W/K/m]
Heat cap. = 3.5 [kJ/K/kg]
Diffusivity = 7.61039e-008 [m^2/s]
Blood Flow = 9100 [W/K/m^3]
Metab. Rate = 1620 [W/m^3]

The properties used to create the breast glandular tissue of the breast phantom was as below:

Disp. eps. = Nth order model (fit): N=3
Mue = 1
Rho = 1020 [kg/m^3]
Therm. Cond. = 0.624 [W/K/m]
Heat cap. = 3.6 [kJ/K/kg]
Diffusivity = 1.69935e-007 [m^2/s]
Blood Flow = 360000 [W/K/m^3]
Metab. Rate = 64000 [W/m^3]

The properties used to create the breast cancer tumor was as below: [9]

Electric Conductivity = 4 [S/m]
Dielectric Permittivity = 39

The radius of the tumor used in the design was 6 mm. The first type of model incorporated the whole antenna shown in figure 3 and 4 below. Matching with its dimension. It

consisted of 1 mm of skin and 29 mm of breast glandular tissue.
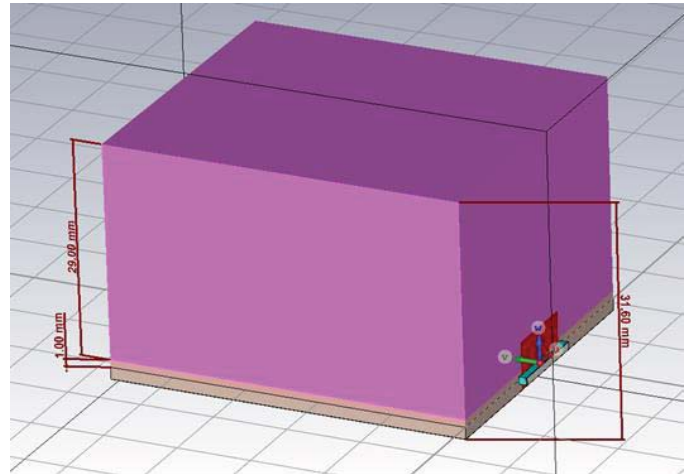
Fig. 3. Breast Tissue model with Skin and Breast Tissue
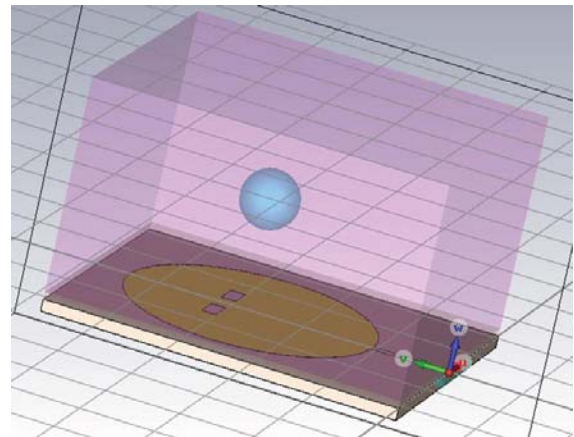
Fig. 4. Breast Tissue model with Skin, Breast Tissue & Tumor

The second model was created to be similar to a real biological model as shown in figure 5 and figure 6. The skin that was created here enveloped the breast tissue. The radius of the skin was 55mm and the radius of the breast tissue was 54mm.
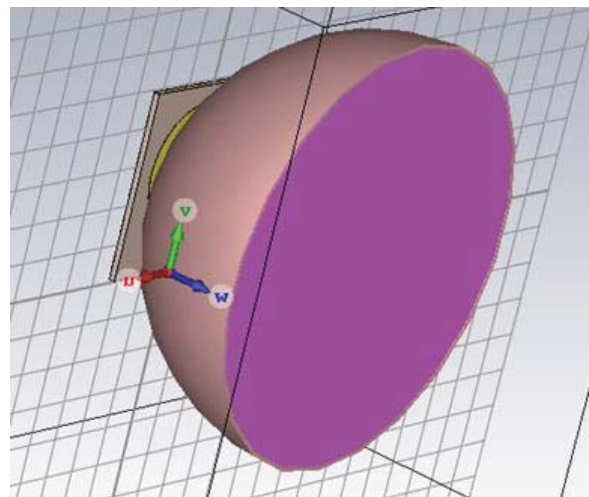
Fig. 5. Breast Phantom model with Skin and Breast Tissue
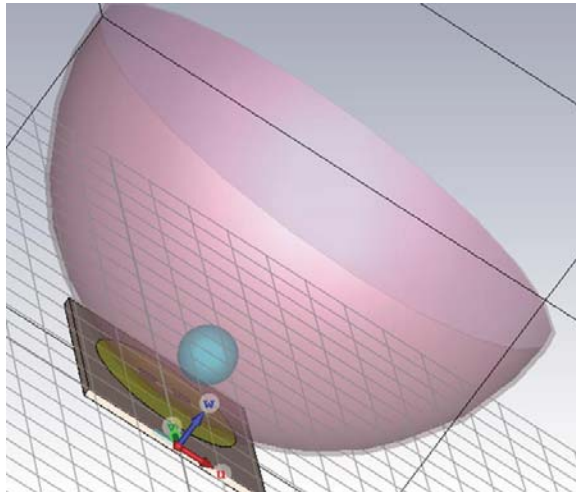
Fig. 6. Breast Phantom model with Skin, Breast Tissue & Tumor

IV. SIMULATION AND RESULTS

S-parameters or reflection coefficients describe the input and output relationship between antenna ports. S_{11} implies the reflected power that the device is trying to deliver to the antenna [10]. After simulating the antenna in free space, resonant frequency was found to be 2.465 GHz with a reflection coefficient value of -31.92 and a VSWR value of 1.052 as seen from figure 7 and 8 below.
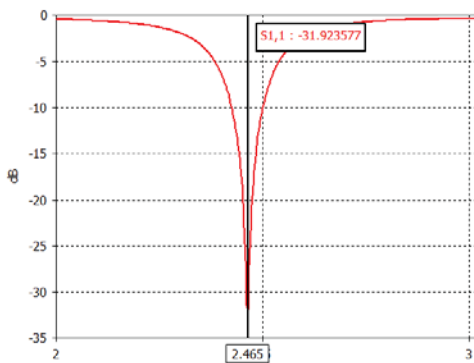
Fig. 7. S_{11} in Free Space
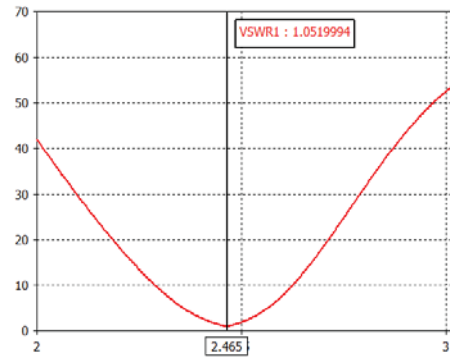
Fig. 8. VSWR in Free Space

A breast tissue region was created and the antenna was simulated by keeping the antenna on top of the skin of the breast. The reflection coefficient had been reduced to -12.470129 while the resonant frequency was found at to 2.885 GHz as shown in figure 9.
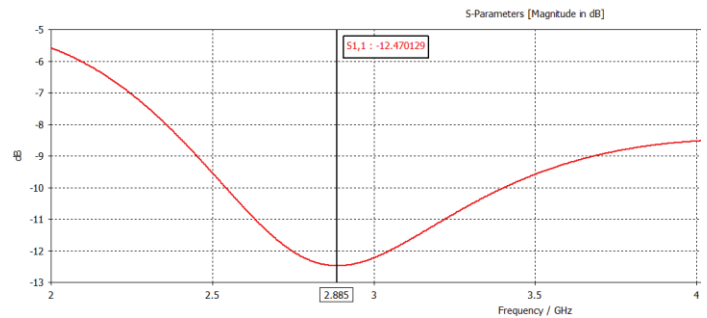
Fig. 9. S_{11} in Breast Tissue model without Tumor
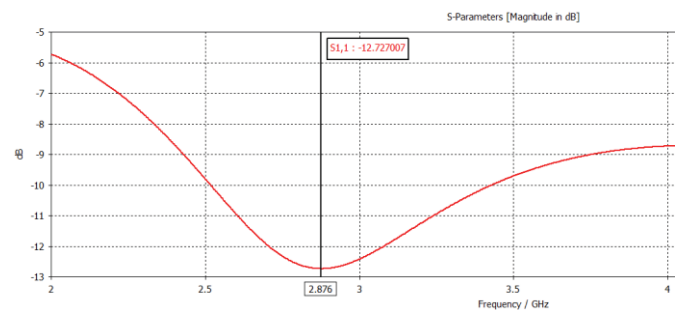
Fig. 10. S_{11} in Breast Tissue model with Tumor

For the analysis of our breast tissue model with tumor from figure 10, we can see that the reflection coefficient drops a bit with the presence of an antenna.

A close look at the curves shown in figure 9 and figure 10 above suggests that the curve goes a little downwards in comparison to the one having no tumor. The new value of reflection coefficient is -12.727007 dB.

Afterwards, the simulation was done for different positions and size of the tumor. At first placing the tumor in the upper

part of the antenna provided the same exact operating frequency. But the noticeable change was in the reflection coefficient value.
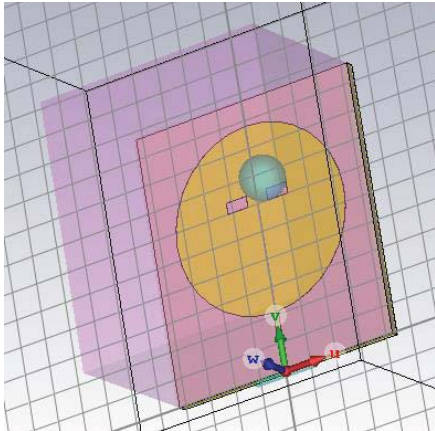
Fig. 11. Breast Tissue model with Tumor Position Right
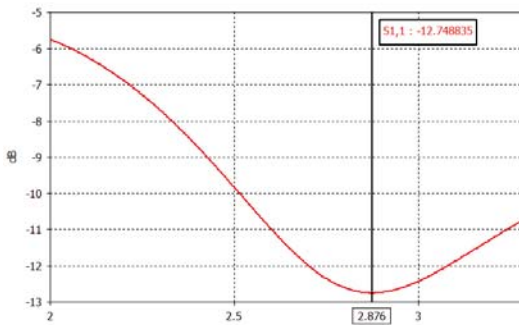
Fig. 12. S_{11} in Breast Tissue model with Tumor Position Right

As seen from figure 11 and figure 12, putting the tumor to the right from the center provided us with a reflection coefficient value of -12.748835 dB. While putting the tumor to the left provided us with a reflection coefficient value of -12.73303 dB as shown in figure 13 and 14 below. So it was understood that a decrease in the coefficient value had indicated that the position of the tumor had moved from the center of the antenna.
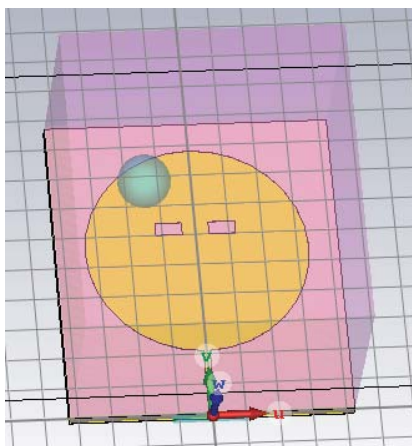
Fig. 13. Breast Tissue model with Tumor Position Left
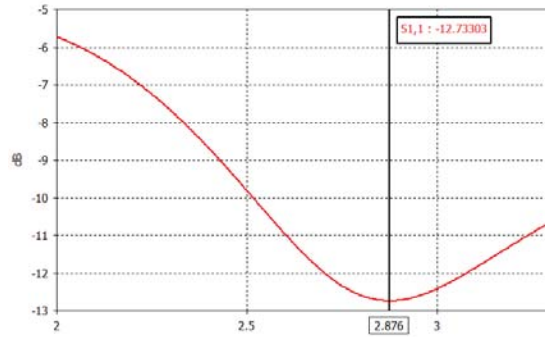
Fig. 14. S_{11} in Breast Tissue model with Tumor Position Left

This time, the simulation was done for different size of the tumor. Increasing the tumor radius to 8 mm, the simulation was done again as seen from figure 15.
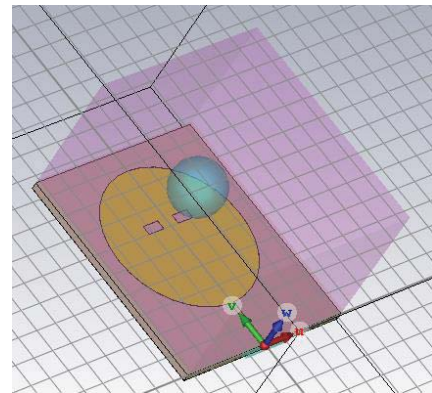
Fig. 15. Breast Tissue model with Bigger Tumor (8mm)
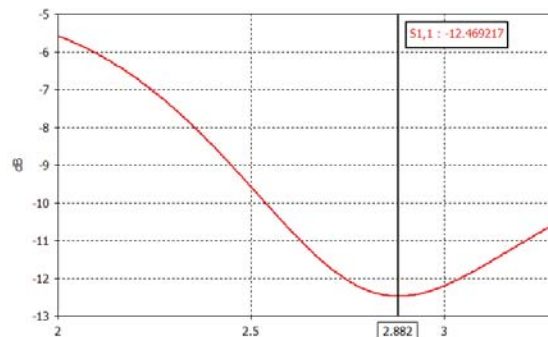
Fig. 16. S_{11} in Breast Tissue model with Bigger Tumor (8mm)

Changing the tumor size provided an increase in the operating frequency which was 2.882 GHz. There was also noticeable change was in the reflection coefficient value. The value of the reflection coefficient was -12.469217 dB as seen in figure 16.
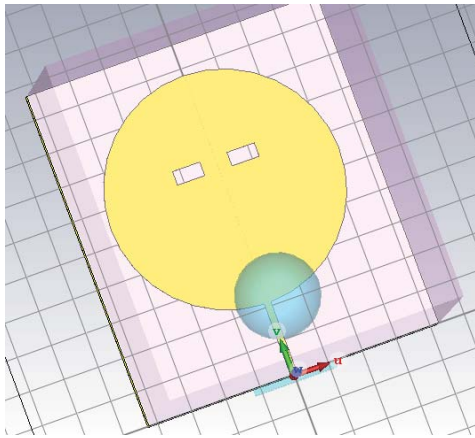
Fig. 17. Breast Tissue model with Bigger Tumor (8mm) – Different Position
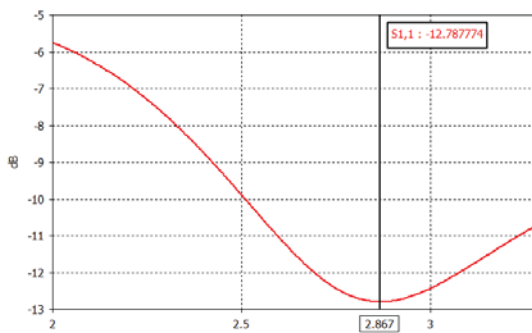
Fig. 19. S₁₁ in Breast Phantom model – Without Tumor

Fig. 18. S_{11} in Breast Tissue model with Bigger Tumor (8mm) – Different Position
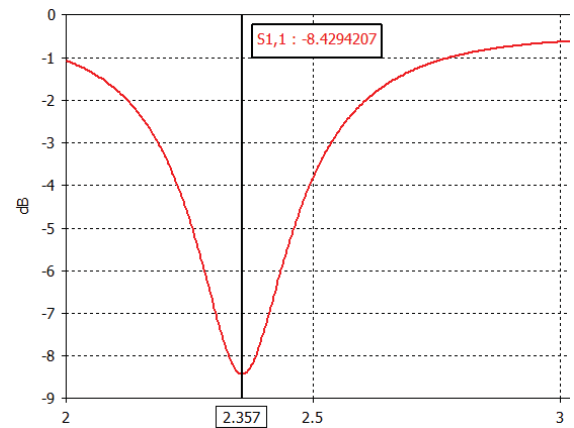
Fig. 20. S_{11} in Breast Phantom model – With Tumor

Putting the tumor to the bottom side provided us with a frequency 2.867 GHz and a reflection coefficient value of -12.787774 dB as observed from figure 17 and figure 18. So we can say that an increase in the size of the tumor decreases the value of reflection and further nether region placement of the tumor decreases it a lot more as observed from figure 16 and figure 18.

This time, the simulation was done for the design of the breast phantom. This provided an updated value of operating frequency at 2.357 GHz. This also provided us with a reflection coefficient value of -8.4932765 dB as seen from figure 19.

In the presence of a tumor provided us with a reflection coefficient value of -8.4294207 dB as per figure 20 above. So, we can say that an increase in the reflection coefficient value indicates that there is an inconsistency present in the breast phantom from figure 8 and figure 9. S_{11} below -10 dB would mean that reflected power is less than 10% and at the very least, 90% input power is delivered to the antenna. So this means that the values that we had gotten were fairly reasonable.

Maximum voltage ratio denoted to the standing wave as minimum is called VSWR or Voltage standing wave ratio. It is also called SWR. Power will not be released proficiently if the antenna impedance and its transmission line do not match each other. In other way some of the power returned back. VSWR is the term of the indication of impedance mismatch. The higher value of the VSWR means the higher value of impedance mismatch.

Simulating the antenna with breast phantom gives a VSWR value of 1.6245145 shown in figure 21.
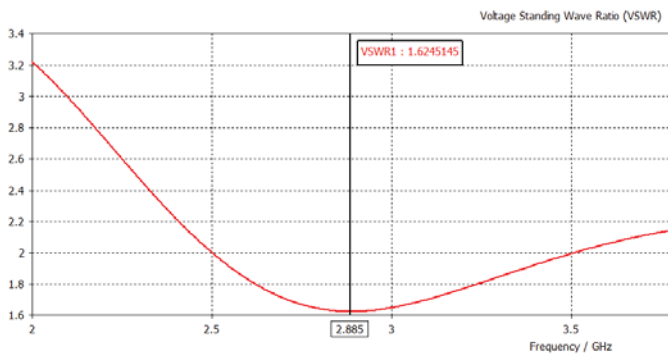
Fig. 21. VSWR in Breast Phantom model

TABLE IV.   COMPARISON CHART

State	Comparison Chart		
	Characteristics	*Breast Phantom 1*	*Breast Phantom 2*
Without Tumor	Resonant Frequency	2.885 GHz	2.357 GHz
	Reflection Coefficient (dB)	-12.470129	-8.4932765
With Tumor	Resonant Frequency	2.876 GHz	2.357 GHz
	Reflection Coefficient (dB)	-12.727007	-8.4294207

The efficiency of an antenna is known as the ratio of the power that is delivered to the power which is radiated from the antenna [11]. From figure 22 below, it can be observed that the directivity of the antenna was found to be 6.776 dBi.

Also, for this antenna, radiation efficiency was measured to be -8.009 dB and the total efficiency was found to be -8.496 dB. The gain of the antenna was found to be 2.453 dB.
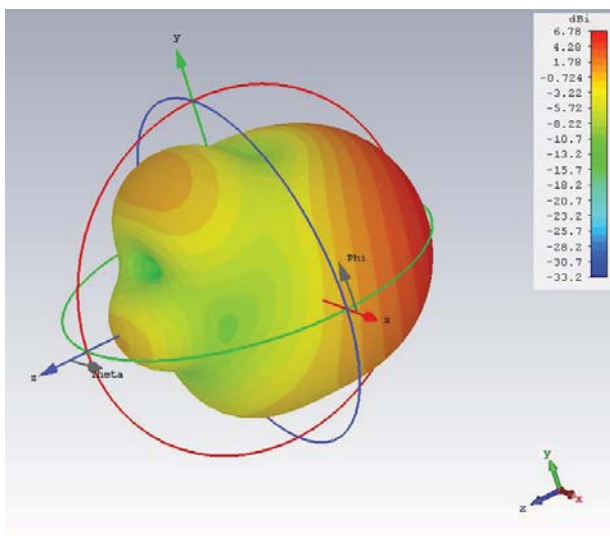
Fig. 22. Farfield Analysis (3D)

From the farfield firectivity (Phi=90) view of the antenna, the magnitude of the main lobe was found to be -28.4 dBi and the magnitude level of the side lobe was observed to be -3.5 dB.

The main lobe direction was at 167.0 deg and angular width (3 dB) was at 83.3 deg as seen from figure 23.
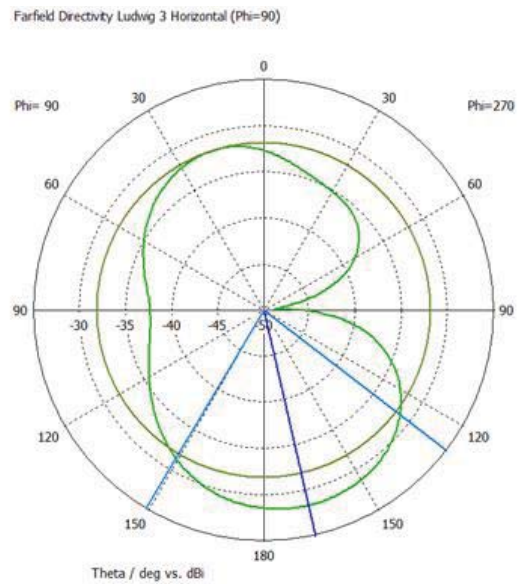
Fig. 23. Farfield Directivity Ludwig 3 Horizontal Analysis (Phi=90)

The maximum SAR for 1g of tissue was calculated. The W/kg bar at the figure below shows the level of intensity for SAR. The maximum SAR value was found to be 0.0603 W/kg for 1g of tissue as seen in figure 24 below.

According to Federal Communications Commission (FCC) which refers patient's safety, the value of SAR should be under 1.6 W/kg for 1g of tissue as per American Standard [12].
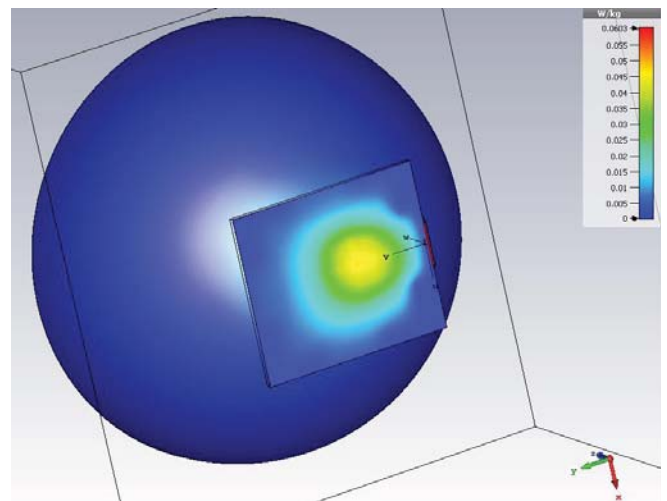
Fig. 24. SAR Distribution (1g Tissue)

V.   CONCLUSION

In this paper, a circular microstrip patch antenna was designed in the ISM band and simulated. The compact size